Changlin Zheng

Investigation of Magnetic Materials and Semiconductor Nanostructures by Electron Holography

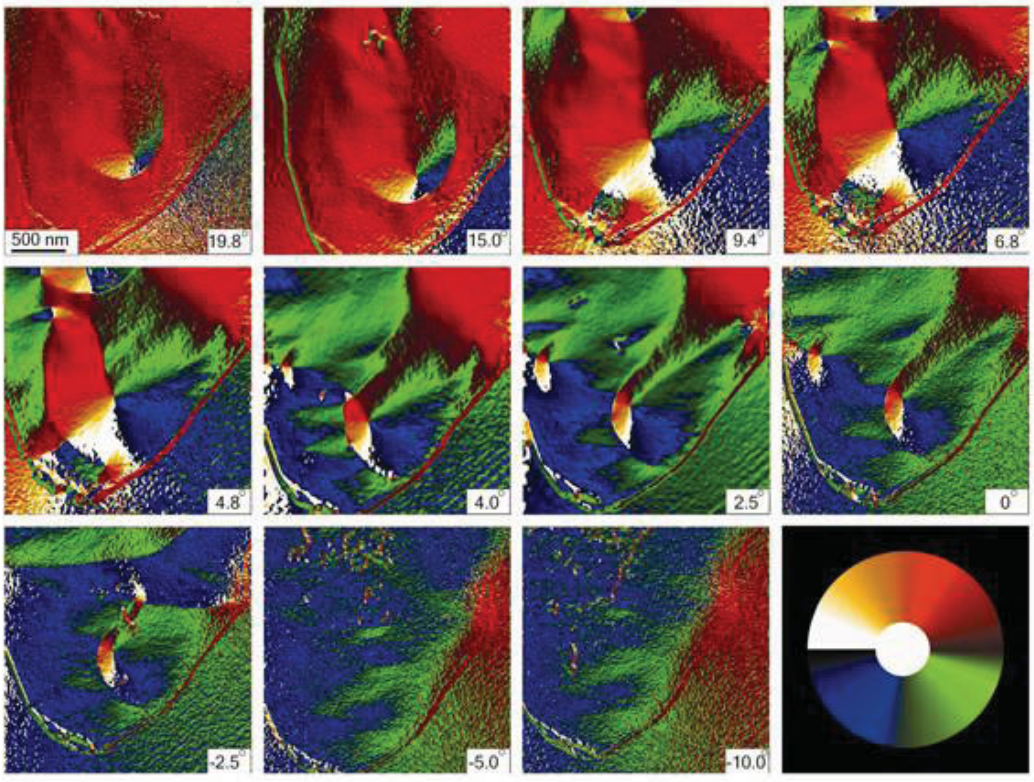

Cuvillier Verlag Göttingen
Internationaler wissenschaftlicher Fachverlag

Investigation of Magnetic Materials and Semiconductor Nanostructures by Electron Holography

DISSERTATION

zur Erlangung des akademischen Grades
doctor rerum naturalium
(Dr. rer. nat.)
im Fach Physik

eingereicht an der
Mathematisch-Naturwissenschaftlichen
Fakultät I
Humboldt-Universität zu Berlin

von
M.Sc. Changlin Zheng
geboren am 14.09.1977 in Jiangsu, China

Präsident der Humboldt-Universität zu Berlin:
Prof. Dr. Dr. h.c. Christoph Markschies

Dekan der Mathematisch-Naturwissenschaftlichen
Fakultät I:
Prof. Dr. Lutz-Helmut Schön

Gutachter:

1. Prof. Dr. Ulrich Gösele
2. Prof. Dr. Wolfgang Neumann
3. Prof. Dr. Michael Lehmann

eingereicht am: 28.05.2009
Tag der mündlichen Prüfung: 15.10.2009

Bibliografische Information der Deutschen Nationalbibliothek
Die Deutsche Nationalbibliothek verzeichnet diese Publikation in der Deutschen Nationalbibliografie; detaillierte bibliografische Daten sind im Internet über http://dnb.ddb.de abrufbar.
1. Aufl. - Göttingen: Cuvillier, 2009
Zugl.: Berlin (Univ.), Diss., 2009

978-3-86955-149-4

Nonnenstieg 8, 37075 Göttingen
Telefon: 0551-54724-0
Telefax: 0551-54724-21
www.cuvillier.de

1. Auflage, 2009
Gedruckt auf säurefreiem Papier

978-3-86955-149-4

Zusammenfassung

Schwerpunkt dieser Arbeit waren Untersuchungen von magnetischen Materialien und von Halbleiter-Nanostrukturen mittels "off-axis" Elektronenholographie. Das Grundprinzip dieser Methode beruht auf dem experimentellen Nachweis und der Analyse der Phasenverschiebung der gestreuten Elektronenwelle verursacht durch die Verteilung des elektrischen und magnetischen Feldes im dreidimensionalen Raum. Die Untersuchungen verfolgten zwei unterschiedliche Themen: die Korrelation von Struktur-Eigenschaftsbeziehungen in FeCo-basierten und Fe-basierten nanokristallinen softmagnetischen Legierungen und die dreidimensionale Abbildung von auf (001) Si-Substraten gewachsenen (Si,Ge)-Inseln.

1. Nanokristalline softmagnetische Legierungen

Die FeCo-basierten und Fe-basierten nanokristallinen softmagnetischen Legierungen wurden mit Hilfe des Schmelzspinnverfahrens hergestellt. Die amorphen Bänder wurden anschließend bei unterschiedlichen Temperaturen wärmebehandelt.

Die Aufklärung der Struktur und chemischen Zusammensetzung der FeCo-basierten nanokristallinen Legierungen erfolgte mittels konventioneller Transmissionselektronenmikroskopie (CTEM) in Hell- und Dunkelfeldabbildung, Elektronenbeugung, hochauflösender TEM (HRTEM), der Z-Kontrasttechnik im Rasterdurchstrahlungsmodus und der energiedispersiven Röntgenspektroskopie.

Die TEM-Untersuchungen zeigten, dass die Legierungen aus einer amorphen Matrix bestehen, in welche nanoskalige FeCo-Kristalle in regelloser Orientierung eingelagert sind. Bei den FeCo-Teilchen handelt es sich durchgängig um die kubisch-innenzentrierte Phase mit einem Gitterparameter von 2.0 Å. Die Größe der Kristallite hängt sehr stark von der Temperatur der Wärmebehandlung während der Kristallisationsphase ab.

Bei der Temperung bei 500°C und 550°C (Temperdauer 1h) beträgt die durchschnittliche Korngröße der Kristallite ca. 12 nm bzw. 18 nm. Bei Temperung bei 610°C (gleiche Temperdauer) ist die amorphe Phase nahezu vollständig kristallisiert worden. Dies führte zu einem drastischen Anstieg der Korngröße auf ca. 90 nm. Ferner konnte nachgewiesen werden, dass einige Kristallite der $Fe_{23}B_6$ Phase entstanden sind.

Die Anordnung der magnetischen Domänen der FeCo-basierten nanokristallinen Legierungen wurde mit Hilfe der Elektronenholographie und der Lorentzmikroskopie untersucht. Die Ergebnisse verdeutlichen, dass eine starke

Korrelation zwischen der Mikrostruktur der Legierungen und der Struktur der magnetischen Domänen besteht. Die bei 500°C getemperten Legierungen bestehen aus magnetischen Domänen deren Größe einen Bereich von einigen Hundert Nanometern bis zu einigen Mikrometern umfasst. Nur wenige Verankerungspunkte (pinning sites) wurden gebildet. Die Anordnung der magnetischen Domänen weist auf gute softmagnetische Eigenschaften hin. Aus dem Linienprofil der Phasenschiebung der Elektronenwelle senkrecht zur Domänenwand wurde eine Wandstärke von ca. 30 nm bestimmt, die erheblich größer ist als die durchschnittliche Nanokristallitgröße von ungefähr 12 nm. Die gemessene Wandstärke stimmt gut mit den numerischen Simulationen überein.

Eine vergleichbare Domänenkonfiguration bezüglich Größe und Verankerungspunkte weisen die bei 550°C getemperten Proben auf. Die Stärke der Domänenwände, bestimmt aus einer Defokusserie von Lorentzmikroskopieaufnahmen, beträgt 40 nm. Auch für diese Wärmebehandlungstemperatur wurde bestätigt, dass die Domänenwände sehr viel dicker als die durchschnittliche Korngröße von 18 nm sind. Aus dem Gradienten der Elektronenphase in Abhängigkeit von der aus EELS-Messungen bestimmten Kristalldicke wurde die magnetische Flussdichte zu 1.0 T bestimmt.

Bei einer Tempertemperatur von 610°C ist die Größe der magnetischen Domänen signifikant reduziert verglichen mit der durchschnittlichen Korngröße von $\sim$ 90 nm. Jede der magnetischen Domänen besteht nur aus zwei bis drei Kristalliten, wobei die magnetischen Domänenwände an den Korngrenzen zwischen den Kristalliten verankert sind. Der magnetische Fluss in dieser Legierung ist sehr komplex und fehlgeordnet, was auf schwache softmagnetische Eigenschaften hinweist.

Das dynamische Magnetisierungsverhalten der Legierungen wurde sowohl mit Hilfe der Lorentzmikroskopie als auch mittels Elektronenholographie untersucht, indem die Probe in einem schwach angeregten Feld der Objektivlinse gekippt wurde. Es konnte so gezeigt werden, dass die bei 550°C getemperten Proben auf diese Weise einfach magnetisiert und demagnetisiert werden können. Während der dynamischen Magnetisierung tritt der Barkhausen Effekt auf. Bei den Legierungen, die bei 610°C getempert wurden, sind die magnetischen Domänenwände an den Korngrenzen verankert. Durch diese unmittelbare Korrelation sind die softmagnetischen Eigenschaften stark unterdrückt.

Die beobachtete Korrelation von Struktur und magnetischen Eigenschaften der Legierungen kann mittels des statistischen Anisotropiemodells von Hertzer interpretiert werden. Die Ergebnisse zeigen, dass Legierungen mit kleineren FeCo-Körnern bessere softmagnetische Eigenschaften aufweisen.

2. Halbleiter-Nanostrukturen

Im zweiten Schwerpunkt der Arbeit wird dargelegt, auf welche Weise die dreidimensionale Rekonstruktion der Gestalt von nanoskaligen (Si,Ge)-Inseln aus der zweidimensionalen Phasenabbildung von Elektronenhologrammen möglich ist. Die (Si,Ge)-Inseln wurden mittels Flüssigphasenepitaxie auf (001)-orientierten Si-Substraten abgeschieden. Für die TEM-Untersuchungen wurden "plan-view"-Proben hergestellt, wobei 2 Proben mit stark unterschiedlichen Inselgrößen untersucht wurden.

Für beide Proben zeigt die Projektion der Inseln in den TEM-Aufnahmen eine quadratische Grundfläche. Eine Inselbreite von 130 nm bzw. 350 nm wurde bestimmt. Aus den Elektronenbeugungsexperimenten geht klar hervor, dass die Inseln eine Parallelorientierung zum Substrat aufweisen. Zum anderen zeigen die Inseln eine hohe laterale Ordnung, was eine Bestätigung für den Stranski-Krastanov-Wachstumsmechanismus ist. Die Zusammensetzung der Inseln wurde unter Zuhilfenahme der gemessenen Inselbreite zu x = 0.38 (Inselbreite $\omega = 130$ nm) und x = 0.23 ($\omega = 350$ nm) bestimmt.

Die Holographieexperimente wurden im Lorentzmodus mit einem großen Gesichtsfeld durchgeführt. Nach der Rekonstruktion der Phasenbilder aus den Elektronenhologrammen wurde der Einfluss des Si-Substrates auf die Phasenschiebung der Elektronenwelle mittels einer Polynomanpassung eliminiert.

Das mittlere innere Potential für $Si_{1-x}Ge_x$-Legierungen wurde mit zwei verschiedenen Methoden berechnet. Für das so genannte "isolierte Atommodell" ergaben sich folgende Werte: 14.69 V ($Si_{0.68}Ge_{0.32}$) und 14.41 V ($Si_{0.77}Ge_{0.23}$) Im Gegensatz dazu lieferte das Modell, in welchem der Einfluss der Atombindungen untereinander berücksichtigt wurde, folgende Werte: 13.37 V ($Si_{0.68}Ge_{0.32}$) und 13.05 V ($Si_{0.77}Ge_{0.23}$). Unter Verwendung der berechneten Werte des mittleren inneren Potentials konnten aus der Phasenschiebung die Inselhöhe ermittelt und so die dreidimensionale Gestalt der (Si,Ge)-Inseln rekonstruiert werden.

Contents

Abbreviations

2D	-	Two-Dimensional
3D	-	Three-Dimensional
BF	-	Bright Field
CBED	-	Convergent Beam Electron Diffraction
CCD	-	Charge Coupled Device
DF	-	Dark Field
DFT	-	Density Function Theory
EDXS	-	Energy Dispersive X-Ray Spectroscopy
EELS	-	Electron Energy Loss Spectroscopy
ENTA	-	Entrance Aperture
HAADF	-	High Angle Annular Dark Field
HCA	-	High Contrast Aperture
HRTEM	-	High Resolution Transmission Electron Microscopy
MBE	-	Molecular-Beam Epitaxy
MFP	-	Mean Free Path Length
MIP	-	Mean Inner Potential
MOKE	-	Magneto-Optical Kerr Effect
NBD	-	Nano Beam Diffraction
SAED	-	Selected Area Electron Diffraction
STEM	-	Scanning Transmission Electron Microscopy
TEM	-	Transmission Electron Microscopy
SAA	-	Selected Area Aperture
SP-STM	-	Spin-Polarized Scanning Tunneling Microscopy
SEMPA	-	Scanning Electron Microscopy with Polarization Analysis
XRD	-	X-ray Diffraction

Chapter 1

Introduction

One of the main tasks of modern materials science is the tailoring of new materials with the properties desired. This tailoring is strongly connected with the characterization of structure, composition, morphology and the structure-property relationships at nanoscale. An important aspect of structure characterization is the direct imaging of materials. Electron microscopy is a powerful method for imaging, diffraction and spectroscopy among the various analytical techniques using different wavelengths and instruments.

Since the first transmission electron microscope (TEM) was built by Max Knoll and Ernst Ruska in 1932, TEM has been proved as one of the most important microscopy tools for the investigation of the structure and composition of materials down to the atomic scale. Compared with other microanalysis methods such as scanning probe microscopy (SPM) or X-ray diffraction, TEM has several significant advantages. First, the high energy electrons accelerated in a TEM (80-1000 keV) have an extreme short wavelength and push the diffraction limitation down to picometer scale. Then more fine spatial structures can be resolved by TEM. In the state of the art instruments, sub-angstrom resolution has been achieved by installing spherical aberration (Cs) correctors for the objective lens and the electron probe. Second, the high energy electrons transmit through the whole thin specimen and carry the bulk information, while conventional SPM is only sensitive to the surface structure. Third, compared with X-rays, electrons can be focused much

easier, thus scattered electron waves can be detected in both the reciprocal space (diffraction mode) and the real space (imaging mode). Additionally, the focused electrons can be used to probe the local structure and composition down to atomic scale, while the signal in the X-ray diffraction is normally coming from a larger area at micrometer scale. Finally, based on the different interactions between the incident electrons and the thin specimen (elastic and inelastic, or coherent and incoherent scattering), various TEM imaging and spectroscopy techniques such as energy dispersive X-ray spectroscopy (EDXS), electron energy loss spectroscopy (EELS) and scanning transmission electron microscopy (STEM) have been developed for the characterization of structure and composition.

The interaction between the incident electrons and the specimen is an electron scattering process by the object potential, including the electrostatic potential and the magnetic vector potential. The electrostatic potential is generated by the positive charges of the nucleus and the negative electron charges in the material and connected with the charge density distribution via Poison equation. It is well known that the charge density distribution including the atom positions, the electronic structure and the interatomic bonding dominates the fundamental properties of the materials. Similarly, the distribution of magnetic vector potential depends on the specimen magnetization and is related to the magnetic properties of the material. Thus, from a general point of view, one of the main tasks of TEM is detecting the scattered electron waves to reconstruct the scattering potential, and further to achieve the information about the related structure, morphology, composition and particular properties.

However there is a well known problem in conventional TEM, that only the amplitude (intensity) of the scattered electron wave, but not the phase can be recorded. The missing phase information limits the further applications of TEM, particularly for the so-called phase objects. Those objects only cause a slight or even no change of scattered electron amplitudes, but a more significant change of the electron phases. Thus, important information is lost with the phase.

In 1948, Dennis Gabor firstly proposed the holography method for solving

the phase problem. As he suggested, by using a known reference wave to superimpose with the scattered electron wave, the full amplitude and phase information will be recorded in the interference fringe image, called electron hologram. After the reconstruction, the amplitude and phase information can be successfully separated.

Today electron holography has been widely used in both high resolution and medium resolution TEM applications. In high resolution electron holography, electron phase shifts are imaged at atomic scales and reflect the rapid varied atomic potential information. Thus, high resolution electron holography can help to get a thorough understanding of the atomic structure of the materials to be investigated.

Furthermore, there is a great interest in medium resolution electron holography. At medium resolution, the electron phase shift induced by a more slowly varying electrostatic and magnetic potential will be imaged and reflect the distributions of the electromagnetic field at nanoscale. These slowly varied potentials include the electrostatic potential generated by the inner field of p-n junctions, ferroelectric domains or the mean inner potential of conventional materials, and the magnetic vector potential of magnetic materials. Applying high energy electrons, these slowly varied scattering potentials (compared with atomic scale) act more like a weak or pure phase object. Then they are difficult to be imaged in a conventional amplitude (intensity) image but show more significant contrast in the phase image. Then quantitative information of the electromagnetic field distributions at nanoscale can be further induced from the phase image. This is particular interesting for magnetic, semiconducting and ferroelectric materials research, since the phase imaging method extends the applications of commonly used TEM from the characterization of structure and composition to the analysis of structure-property relationships.

This work mostly focuses on the applications of electron holography at medium resolution. In the first topic of this thesis, we will describe electron holography and Lorentz microscopy for the observation of the magnetic domain structure and the correlations between microstructure and magnetic domain structures in FeCo-based and Fe-based nanocrystalline soft mag-

netic alloys. In the second topic, we will deal with 3D-(Si,Ge) semiconductor nanostructures investigated by a 2D-phase mapping. The content of the thesis is divided into the following parts:

Following this introduction (chapter 1), an introduction to the theoretical and practical methods of electron holography, including the hologram formation, recording and phase reconstruction is given in chapter 2. The main parameters and the influence of the instrument performance on the phase image will also be discussed.

In chapter 3, the investigation of the microstructure of FeCo-based nanocrystalline alloys by advanced TEM techniques is discussed carefully, including diffraction contrast imaging, electron diffraction, HRTEM, STEM-HAADF as well as EDXS.

The study of magnetic domain structure and the correlations between microstructure and magnetic domain structure in FeCo-based and Fe-based nanocrystalline alloys will be treated in chapter 4. First the magnetic contrast formation in electron holography will be discussed in detail. Then, the observation of magnetic domain structures by means of Lorentz microscopy and electron holography will be illustrated. The domain wall width was measured and compared with a numerical simulation. The quantitative magnetic flux density was measured by a special procedure, where EELS measurements for the determination of thickness were utilized. Furthermore, the dynamical magnetization was observed in both the Lorentz microscopy and electron holography. The correlations between the microstructure and the magnetic domain structure will be discussed. The properties of the magnetic domain structure of a new type of B free Fe-based nanocrystalline alloys will also be presented.

Chapter 5 deals with the 3D-imaging of (Si,Ge) islands from a 2D-phase mapping. First, the basic principle is described for 3D-reconstruction of the nanostructure from 2D-phase mapping. The relationship between specimen thickness and electron phase shift due to the mean inner potential will be discussed. Then the experimental phase mapping and digital phase processing are presented. Following two different models, viz., the isolated atom model and the “bonded atom” model, the mean inner potential of (Si,Ge) alloys is calculated and applied for the 3D reconstruction.

Finally in chapter 6, a summary of the whole work and an outlook are given.

Chapter 2

Theory and experimental techniques

This chapter presents the theoretical fundamentals and the experimental techniques of off-axis electron holography. In addition, the magnetic contrast formation in Lorentz microscopy is explained.

2.1 Introduction to holography

2.1.1 Brief history of holography

The word "holography" is coming from the Greek word "holos", which means "whole" or "complete". This word precisely describes the unique characteristics of the holography, that not only the amplitude, but also the phase of the wave will be recorded and can be interpreted. The theory of holography was firstly developed by the British/Hungarian scientist Dennis Gabor in 1947. At that time he was working in improving the resolution of transmission electron microscopes. He realized that by using a reference wave, the phase of electron wave could be recorded in an interference image and then be used for the correction of the spherical aberration (Cs) of the lens [1]. Today this phase recording method is widely extended to various kinds of applications, varying from data storage to 3D visualization as well as advanced materials research. In 1971, Gabor won the Nobel price in physics for his fundamental contributions to holography.

Following Gabor's original idea, the first electron holography experiment was performed by M.E. Haine and T. Mulvey in 1952 [2]. However in subsequent decades, the further developments in both of electron holography and optical holography were stymied due to the lack of high coherent sources. This situation had not been changed until the invention of laser in 1960. Then the optical holography entered a high speed development time. One of the significant advancements at that time was the invention of off-axis holography by Leith and Upatnieks in 1962 , which can successfully solve the twin-image problem in in-line holography [3]. The same concept was also developed in electron holography by Möllenstedt and Wahl. They firstly designed and built an electrostatic type of biprism which can efficiently work as a beam splitter for off-axis electron holography [4, 5]. Another important factor for the implementation of electron holography is coupled with the development of high brightness and high coherence field emission electron sources. Today, electron holography has become an important branch in the field of transmission electron microscopy.

Since the phase shift of electrons is directly connected with the electrostatic potential and the magnetic vector potential of the materials, this phase imaging technique has opened a new approach for materials science research at nano- and atomic scale. For example, by imaging the electrostatic potential distribution, electron holography can be used to study the polarization in ferroelectric materials [6] and dopant distribution in semiconductor materials [7–10]. Furthermore, by probing the magnetic vector potential distribution, magnetic structures such as magnetic domain configurations and magnetic flux distributions in magnetic materials can be imaged and quantitatively analyzed [11, 12].

2.1.2 Phase shift and interference fringes

The principle of holography can be explained by a simple wave interference model, as shown in Fig. 2.1. A and B are two ideal point sources which emit the coherent waves Ψ_A and Ψ_B, respectively. Both waves Ψ_A and Ψ_B

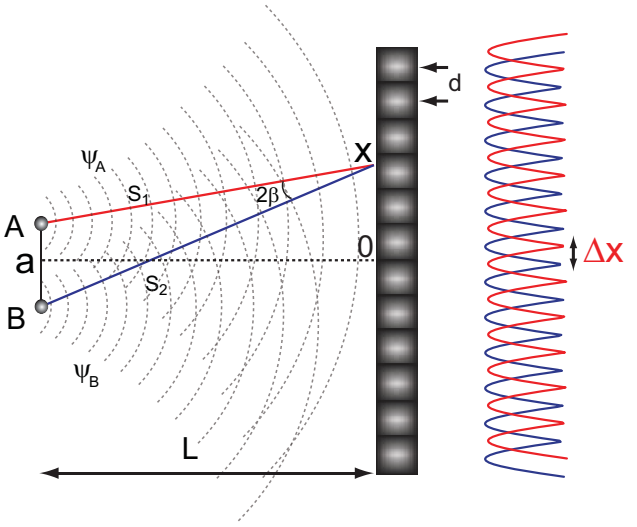

Figure 2.1. The formation of interference fringes by two coherent beams.

have the same wavelength λ and there is no initial phase shift between them. Due to the wave interference, bright and dark fringes will be formed on the screen.

It is well known that the intensity at a specific point x on the screen depends on the phase difference $\Delta\phi$ between wave Ψ_A and wave Ψ_B at that point. $\Delta\phi$ is determined by the optical path length (OPL) difference $S = S_2 - S_1$ with

$$\Delta\phi = 2\pi\frac{S}{\lambda} \tag{2.1}$$

From the geometrical relationship (Fig. 2.1), when $x \ll L$ and $a \ll L$ [13],

$$S = \sqrt{L^2 + (x + \frac{a}{2})^2} - \sqrt{L^2 + (x - \frac{a}{2})^2} \simeq \frac{ax}{L} \tag{2.2}$$

Then the phase difference between Ψ_A and Ψ_B at point x is given by

$$\Delta\phi = 2\pi\frac{ax}{L\lambda} \tag{2.3}$$

When $\Delta\phi = 2\pi n$ ($n = 0, \pm1, \pm2, ...$), the intensity reaches the maximum. The positions of the intensity peaks x_{max} are given by

$$x_{max} = n\frac{L\lambda}{a} \tag{2.4}$$

However, if there is an initial phase shift ϕ_{int} between Ψ_A and Ψ_B, compared with Eq. 2.1, the ultimate phase difference $\Delta\phi$ will become

$$\Delta\phi = 2\pi\frac{S}{\lambda} + \phi_{int} \tag{2.5}$$

Then the whole fringes will be shifted along x with distance

$$\Delta x = \phi_{int}\frac{L\lambda}{2\pi a}, \tag{2.6}$$

and the fringe spacings will not be changed. On the other hand, the initial phase shift ϕ_{int} can be determined from the shift of the fringes Δx, according to Eq. 2.6,

$$\phi_{int} = \Delta x\frac{2\pi a}{L\lambda} \tag{2.7}$$

Then, we will get the basic principle of holography that the phase of an unknown wave can be recorded and reconstructed in an interference image when using a known reference wave. The shift of the fringes directly reflects the initial phase shift of the two waves.

2.1.3 General representation

Instead of analyzing the shift of the fringes in the example shown in Fig. 2.1, here we will give a more general representation of the formation and reconstruction of a hologram. The total wave on the screen due to the superposition of Ψ_A and Ψ_B can be written as

$$\Psi = \Psi_A + \Psi_B \tag{2.8}$$

Thus the intensity I on the screen is given by:

$$I = |\Psi_A + \Psi_B|^2 = |\Psi_A|^2 + |\Psi_B|^2 + \Psi_A\Psi_B^* + \Psi_A^*\Psi_B \tag{2.9}$$

From Eq. 2.9 we can see that the complete wave Ψ_A (amplitude and phase) is recorded in the third and the forth terms. In principle, Ψ_A can be reconstructed from the interference image I. The simplest way is to use the known wave (reference wave) Ψ_B to illuminate the interference image [14]. As a result we will get

$$I \cdot \Psi_B = |\Psi_A|^2\Psi_B + |\Psi_B|^2\Psi_B + \Psi_A + \Psi_A^*\Psi_B^2 \tag{2.10}$$

From Eq. 2.10 it is obviously that the complete wave Ψ_A is reconstructed.

2.1.4 In-line holography

There are various forms of holography, and the original one proposed by Gabor is the so-called in-line holography. In this form, the object is illuminated either by a convergent beam focused on the object or by a plane wave. Then the unscattered transmitted wave is also used as a reference wave to form the hologram with the scattered wave. Figure 2.2 shows such an example with plane wave illumination. The total wave is,

$$\Psi_{tot} = e^{ikz} + \Psi_{obj} \tag{2.11}$$

The intensity of the hologram is given by

$$I = \left|e^{ikz} + \Psi_{obj}\right|^2 = 1 + |\Psi_{obj}|^2 + e^{-ikz}\Psi_{obj} + e^{ikz}\Psi_{obj}^* \tag{2.12}$$

For the reconstruction procedure, we use again a plane wave e^{ikz} to illuminate the hologram. This step can be described as

$$I \cdot e^{ikz} = e^{ikz}(1 + |\Psi_{obj}|^2) + \Psi_{obj} + e^{-2ikz}\Psi_{obj}^* \tag{2.13}$$

From here we can see that the object wave Ψ_{obj} which corresponds to the

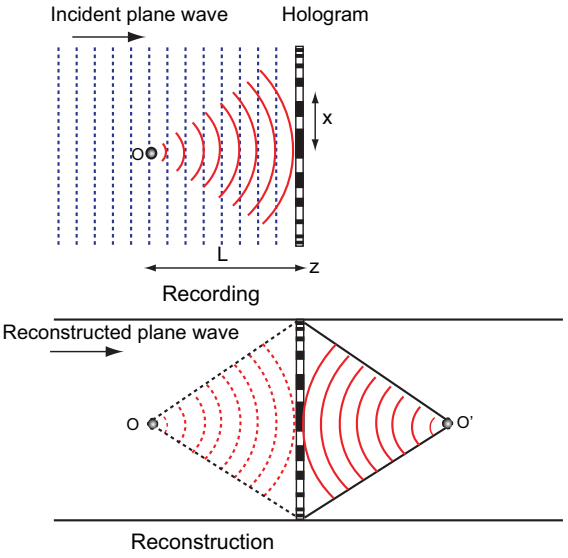

Figure 2.2. Schematic representation of the formation and reconstruction of in-line holography. Adapted from ref. [13].

third term in Eq. 2.13 has been successfully reconstructed. Unfortunately, a complex conjugate object wave Ψ^*_{obj} in the fourth term is also reconstructed. Since the phase factor e^{-2ikz} is along the z-axis and it does not take an effect, the object wave and the complex conjugate wave is symmetrically located between the two sides of the hologram plane (xy plane) as shown in the lower part of Fig. 2.2. Then, an observer from the right side can not distinguish these two image waves. This is the so-called "twin-image problem" of the in-line holography. One solution for this problem is using off-axis electron holography, which was firstly proposed by Leith and Upatnieks in 1962 [3].

2.1.5 Off-axis holography

Leith and Upatnieks firstly realized that it is not necessary to use the transmitted wave, but instead of this one can use a by-passing tilted wave as reference wave. Figure 2.3a illustrates such an example. A tilted plane wave $\Psi_{ref} = e^{i(kz-qx)}$ is superimposed with the objective wave and will form a holo-

gram on the screen. The intensity of the hologram on the screen is written as

$$I = \left|e^{i(kz-qx)} + \Psi_{obj}\right|^2 = 1 + |\Psi_{obj}|^2 + e^{-i(kz-qx)}\Psi_{obj} + e^{i(kz-qx)}\Psi^*_{obj} \quad (2.14)$$

After the reconstruction by means of illuminating the hologram with the plane wave Ψ_{ref}, we will get

$$I \cdot e^{i(kz-qx)} = e^{i(kz-qx)}(1 + |\Psi_{obj}|^2) + \Psi_{obj} + e^{-2i(kz-qx)}\Psi^*_{obj} \quad (2.15)$$

Comparing Eq. 2.15 with Eq. 2.13, we will find that the complex conjugate wave Ψ^*_{obj} is tilted in the x-y plane. As a result the reconstructed object wave and the complex conjugate wave are successfully separated.

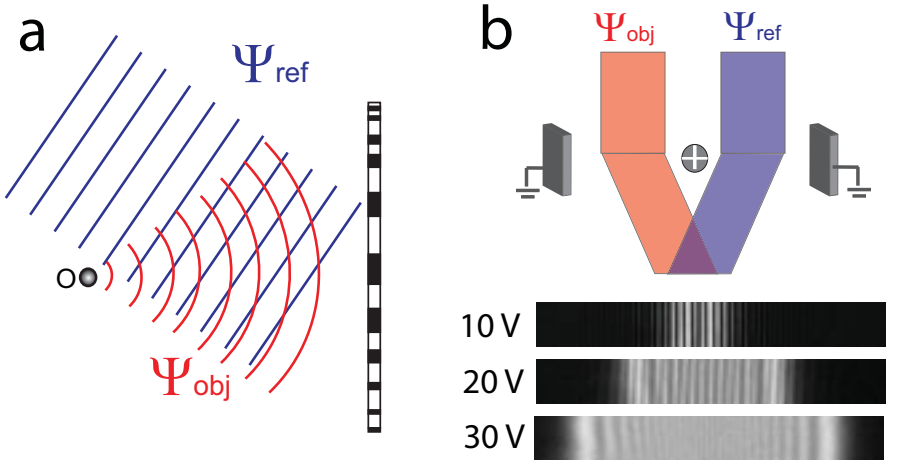

Figure 2.3. (a) Schematic illustration of the principle of "off-axis holography"; (b) formation of off-axis electron hologram by using an electron biprism. The series of interference images at bottom was recorded with different biprism voltages.

From here one can see there are two essential conditions for off-axis holography. First, the source should be highly coherent to ensure the object wave and the reference wave will still keep enough coherence when they travel along different paths. Second, an efficient beam splitter should be used [15].

Both conditions can be easily satisfied in optical holography when using a laser as highly coherent optical source and when using a glass prism or half-silvered mirror as beam splitter. However, for electron holography, only a field emission gun (FEG) can satisfy the requirements for a highly spatial coherence. Furthermore, to construct an efficient beam splitter for electrons is not an easy task.

The earliest attempts for splitting and deflecting electron beams are carried out by single crystal electron diffraction [16]. However, it is not applicable for off-axis electron holography. A breakthrough for off-axis electron holography was the invention of the electrostatic biprism for electrons by Möllenstedt and Düker in 1956 [4]. Figure 2.3b schematically illustrates the basic principle of an electron biprism.

The electron biprism consists of a thin metal wire or a quartz wire which is coated with a gold layer. The diameter of the wire is normally only several hundreds nanometers. The wire is placed between the grounded electrodes. When a positive voltage U_a is applied on it, an electrostatic field will be created around the wire. The distribution of the electrostatic potential V(r) is approximately given by

$$V(r) = U_a \frac{\log(r/r_1)}{\log(r_1/r_2)}, \tag{2.16}$$

where r_1 is the diameter of the wire and r_2 is the distance between the wire and the grounded electrode [17, 18]. The incident parallel beam will be deflected with an angle

$$\alpha = \frac{\pi U_a}{2E \log(r_1/r_2)}, \tag{2.17}$$

where E is the kinetic energy of electrons. From a similar geometrical relationship as shown in Fig. 2.1, we can quantitatively calculate the fringe spacings and the whole width of the fringes from the applied biprism voltage. A more detailed description is given in ref. [18]. In general, the spacing of the fringes is decreased with increasing voltage of the biprism while the total width of the fringes is increased with the biprism voltage. A series of electron holograms recorded with different biprism voltages is shown in Fig. 2.3.

2.2 Principle of off-axis electron holography

2.2.1 Formation of the electron hologram

A ray-diagram of off-axis electron holography in TEM is illustrated in Fig. 2.4. An electron biprism is located close to the first image plane. The high energy coherent electrons are emitted from the field emission gun (FEG) and will be collimated to illuminate the sample through the condenser lens system. The incident wave could be regarded as plane wave with uniform amplitude and the wave vector is parallel to the optical axis. The sample is located in such a way that only half (or less) part of the beam transmits through it while the other part of the beam transmits through the vacuum as a reference wave Ψ_{ref}. The wave transmitted through the sample is modulated by the object potential and can be written as:

$$\Psi_{obj} = A(\vec{r})e^{i\phi(\vec{r})}, \tag{2.18}$$

where $A(\vec{r})$ and $\phi(\vec{r})$ represent the modulated amplitude and phase, respect., and $\vec{r}$ is a two dimensional vector in the sample plane. The wave vector along the optical axis is omitted.

After passing through the objective lens, the amplitude and the phase of the object wave will be slightly modified by the lens due to the lens aberrations. Since in this work we mainly treat the medium resolution electron holography, the lens aberration effect can be neglected.

Close to the first image plane, the reference wave and the object wave will be deflected toward each other by the biprism and form interference fringes. These interference fringes are further magnified by the successive lens system and recorded by a CCD camera as electron hologram. The total interference wave is given by:

$$\Psi_{tot}(\vec{r}) = \Psi_{ref}(\vec{r}) + \Psi_{obj}(\vec{r}) = e^{i\vec{q_c}\cdot\vec{r}} + A(\vec{r})e^{-i(\vec{q_c}\cdot\vec{r}+\phi(\vec{r}))}, \tag{2.19}$$

where $\vec{q_c}$ describes the spatial frequency of the deflected beam (carrier frequency) and depends on the deflected angle. Then, the intensity of the hologram can be written as:

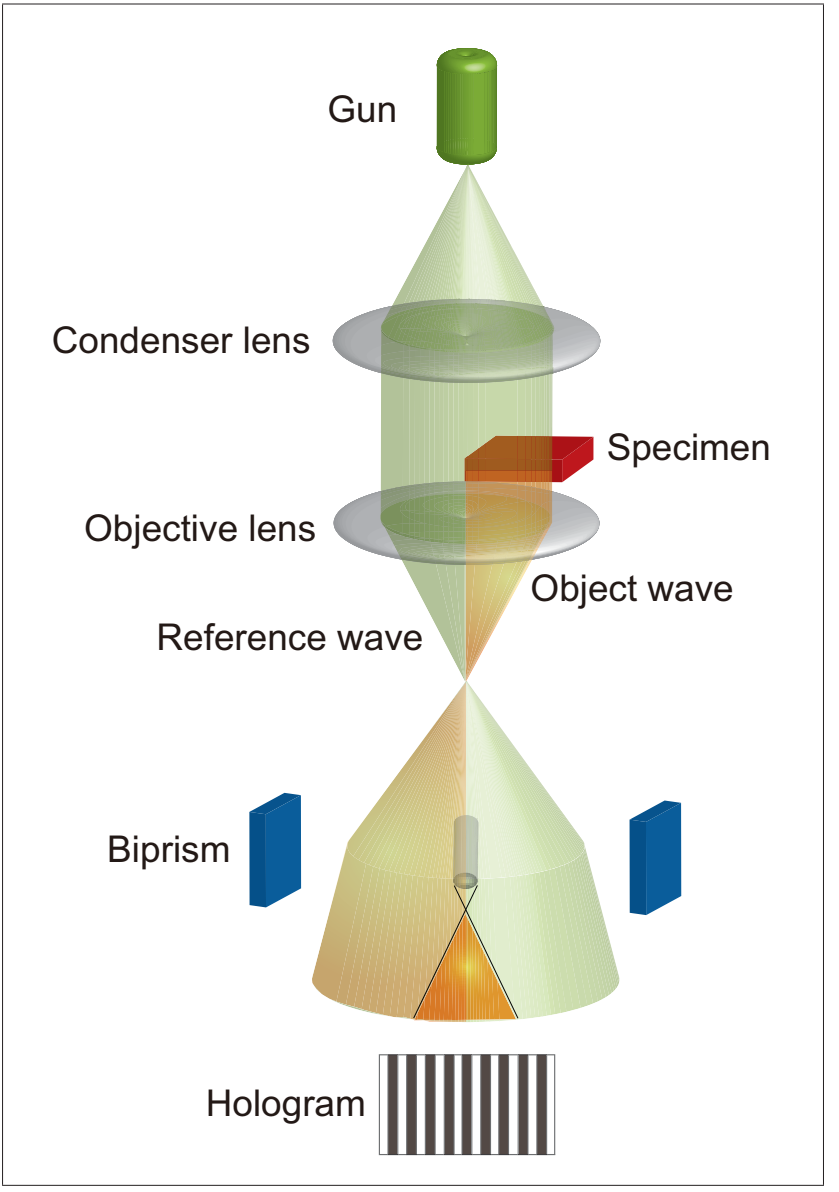

Figure 2.4. Ray diagram of off-axis electron holography in TEM.

$$I_{holo}(\vec{r}) = |\Psi_{holo}(\vec{r})|^2 = 1 + A(\vec{r})^2 + 2A(\vec{r}) \cdot cos(2\pi \vec{q_c} \cdot \vec{r} + \phi(\vec{r})) \qquad (2.20)$$

Both the amplitude $A(\vec{r})$ and phase $\phi(\vec{r})$ of the object wave are recorded in the hologram.

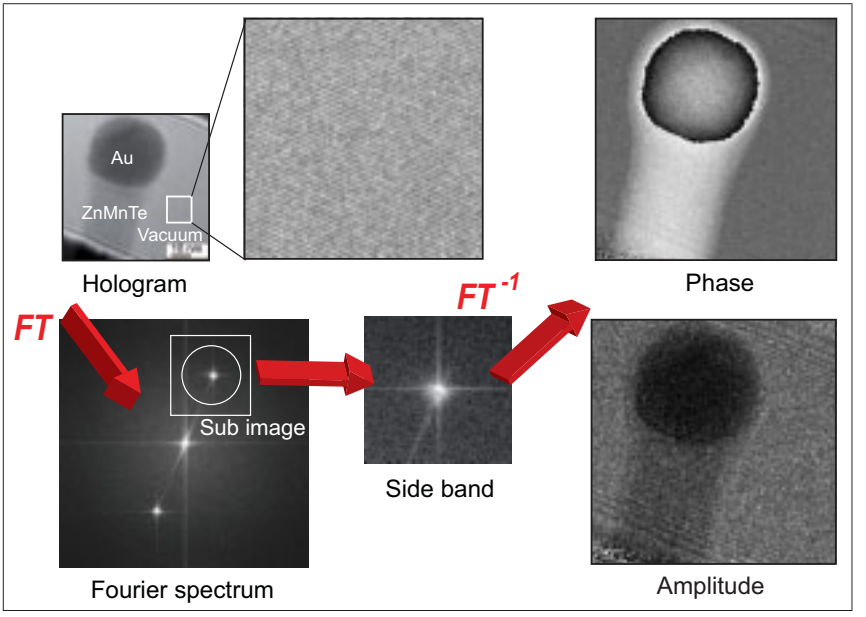

Figure 2.5. Reconstruction of the object exit wave from the electron hologram. Sample: Au/ZnMnTe nanowire grown by MBE.

2.2.2 Reconstruction of phase and amplitude images

In order to extract the phase information from the hologram, it is necessary to carry out a post reconstruction process. Since the phase information is encoded in the relative shift of the interference fringes, there are two different routes for the reconstruction procedure: performing the reconstruction in real space or in Fourier space (frequency space). During the first procedure, the modulated phase of the object wave will be directly measured and calculated from the relative positions of the interference fringes in the hologram [19, 20].

Compared to that, a more convenient way is to transfer the shift of the interference fringes in real space to the frequency change in Fourier space [15, 21].

A typical example of the reconstruction in Fourier space is shown in Fig. 2.5. The sample is an Au/ZnMnTe nanowire grown by molecular-beam epitaxy (MBE). The gold is located at the top of the ZnMnTe nanowire, around the nanowire is vacuum. The supporting carbon film is at the bottom of the nanowire and out of the field of view. The interference fringes are clearly visible in the enlarged hologram.

After applying a Fourier transform to the hologram, the corresponding Fourier spectrum was obtained. The spectrum shows three distinguished parts, one center band and two symmetrically distributed side bands. In order to have a thorough understanding of the physical meanings of the spectrum, we calculate the Fourier transform of Eq. 2.20. Then, we get

$$\begin{aligned}\mathbf{FT}[I_{tot}(\vec{r})] = \\ &\delta(\vec{q}) + \mathbf{FT}[A(\vec{r})^2] + \\ &\delta(\vec{q}+\vec{q_c}) \otimes \mathbf{FT}[A(\vec{r}) \cdot e^{i\phi(\vec{r})}] + \\ &\delta(\vec{q}-\vec{q_c}) \otimes \mathbf{FT}[A(\vec{r}) \cdot e^{-i\phi(\vec{r})}],\end{aligned} \tag{2.21}$$

where the symbol $\otimes$ denotes the convolution operation. The first and the second term of Eq. 2.21 correspond to the center band in Fig. 2.5, while the third and the fourth term correspond to the other two side bands. Equation 2.21 clearly indicates that the center band contains only the information about the amplitude. On the other hand, each of the two side bands (the third and the forth item in Eq. 2.21) contains both the amplitude and the phase information. Thus, from the physical point of view, the two side bands are identical and any of them could be used for the reconstruction of the full object wave. The separation of the two side bands is due to the off-axis tilting of the object and reference wave.

The next step is to find the center of the side band, which represents the carrier frequency $\vec{q_c}$ in Fourier space. Normally, this is the highest intensity pixel in the side band and most of the commonly used reconstruction pro-

grams can find it automatically. For some special cases the side band can be strongly distorted. Then, the real center of the side band should be found with the help of a reference hologram. A detailed discussion of this procedure will be given later.

In the third step, one of the side bands will be selected by a numerical aperture as indicated by the white ring in Fig. 2.5. The centers of the aperture and the side band should be aligned to each other with a high accuracy. Then, the sub-image of the side band will be cut and created as a new image for reconstruction. This step corresponds to the selection of the third or the fourth term in Eq. 2.21. Since the side band is shifted now to the center of the new image, according to Fourier transform theory, the convolution operations $\otimes$ with $\delta(\vec{q} \pm \vec{q_c})$ in the third and the fourth terms of Eq. 2.21 will be canceled out. Then only the terms $\mathbf{FT}[A(\vec{r}) \cdot e^{\pm i\phi(\vec{r})}]$ will be kept.

Several types of a numerical aperture can be used for this step. The simplest one is called hard aperture, which means the image intensity outside of the aperture will be set to zero while the intensity inside the aperture will be kept with the original value. However, this kind of aperture will cause some artifacts, so it is in general only used in high resolution holography. In medium resolution holography, a so-called Butterworth filter is often applied. Detailed description of Butterworth filter can be found in Ref. [15, 22].

Finally, after an inverse Fourier transform to the side band image (corresponds to the terms $\mathbf{FT}[A(\vec{r}) \cdot e^{\pm i\phi(\vec{r})}]$), the phase and amplitude of the object wave will be reconstructed, as shown in Fig. 2.5.

2.2.3 Reference hologram

In practice, after each hologram has been recorded, the sample should be moved away immediately and an empty hologram of the vacuum should be recorded under the same optical conditions. This empty hologram will be used as a reference hologram during the reconstruction. There are two reasons for using this reference hologram: First, to compensate the geometric distortions induced by the electron optical system. Second, to find easier the real center of the side band.

Electron optical distortion on phase image

The geometric distortions induced by the electron optical system are coming from several different sources: Lens distortion, CCD optical fiber coupling, the charging and contamination as well as a varying thickness of the biprism itself [15, 23].

Lens distortion is a kind of spherical aberration which mainly affects the projection lens. This is because the projection lens magnifies the large area of the intermediate image which has been magnified by the objective lens. The different rays starting from the same point in the intermediate image plane should be reunited at the final image plane. However, due to the lens distortion, the magnification will vary at this plane and the final image will be distorted. The different types of lens distortion are schematically illustrated in Fig. 2.6. Though the lens distortion can be directly measured and corrected by some particular methods (see Ref. [24]), for electron holography the easiest way is to use a reference hologram during the reconstruction. This is because the distortions will be recorded in both the object hologram and the reference hologram under the same imaging conditions.

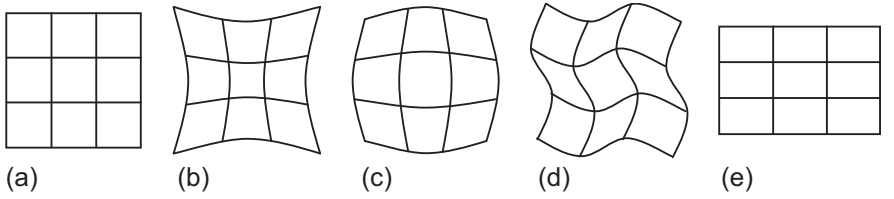

Figure 2.6. Illustration of lens distortion: (a) undistorted object; (b) pincushion distortion; (c) barrel distortion; (d) spiral distortion; (e) elliptical distortion [24].

Another distortion source is coming from the optical fiber couplings in the CCD camera. In a CCD camera for recording electron images, the incident electrons will be first transformed to photons (light signals) by a single crystal YAG scintillator. Then the light signals will be further transferred to CCD

sensor through an optical fiber coupling system [25]. During this optical transfer, some additional image distortions which are inevitable in the process of fabrication will be induced. The distortions will be recorded in the final images.

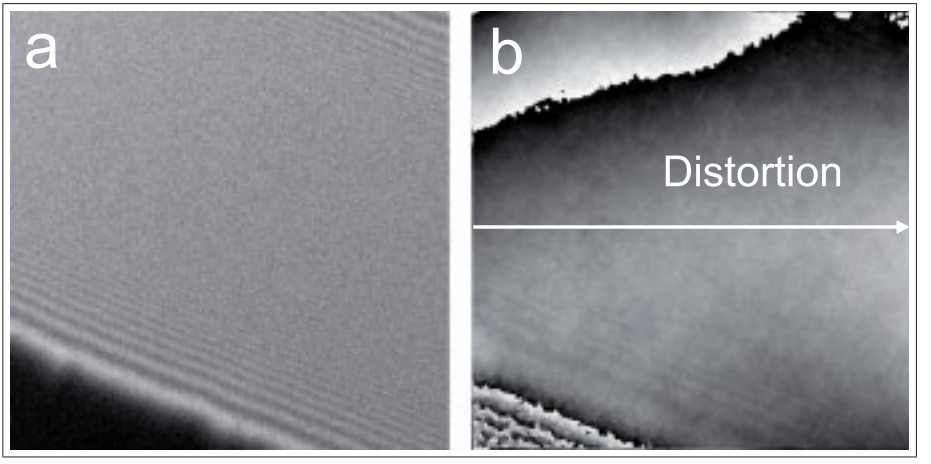

Figure 2.7. Electron optical distortion on (a) an empty electron hologram and (b) the corresponding reconstructed phase image. The electron hologram was imaged in the JEOL 2200FS transmission electron microscope using HOLO-M mode (magnification 250 kX). A Gatan 794 slow scan CCD camera was used to record the image.

Although the geometric distortions are existing in conventional TEM images, they cause more significant impact on phase images. This is due to the following reasons. First, the phase information is encoded in the relative shift of the interference fringes. Then a small geometric distortion in the hologram will be "magnified" into a large phase distortion in the reconstructed phase image. For example, if we assume each of the interference fringes consists of ten pixels, then a geometric distortion with one pixel in the hologram will be transformed into a significant phase error of $2\pi \times \frac{1}{10} = \frac{1}{5}\pi$ after the reconstruction procedure. Addtionally, for most applications of the electron holography, only the phase difference between two specific points has a physical meaning. Thus, the local phase error will be summed along the path connecting the two points. An example of geometric distortions is shown in Figure 2.7.

Figure 2.7a is an empty hologram recorded in the vacuum area. No obvious distortions can be seen across the whole hologram. However on the corresponding reconstructed phase image as shown in Fig. 2.7b, the distortions can be easily recognized. A phase line profile along the white arrow is plotted in Fig. 2.8. The minimum phase has been offset to 0. The phase difference between the two ends of the line is 2.2 rad, which is too large for most of the electron holography applications. Since the distortions are recorded in both of the object hologram and the reference hologram, they can be easily subtracted by comparing the two images during the reconstruction.

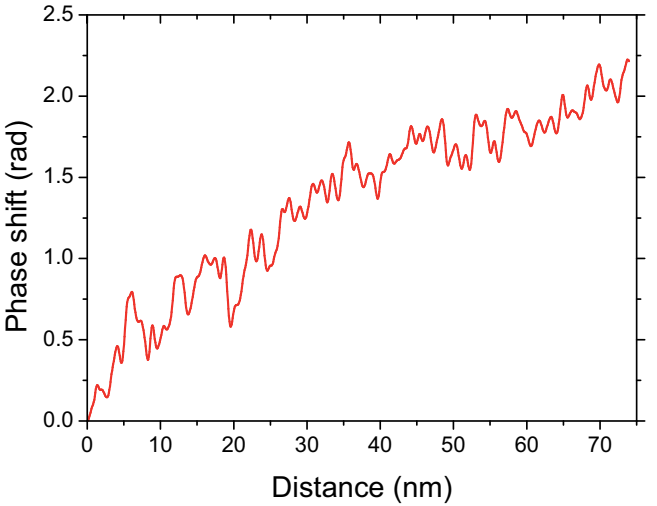

Figure 2.8. Line profiles of the phase distortion induced by electron optical distortions. The position of the line profile is marked as white line in Fig. 2.7.

Find the real center of the side band

Another reason for using a reference hologram during the reconstruction is to find out the real center of the side band more easily. In some situations, such as imaging magnetic samples with a strong stray field, both the object wave and the reference wave in the vacuum will be strongly distorted by the

magnetic field (see Fig 2.9). Then, the highest intensity pixel in the Fourier spectrum image may not indicate the real center of the side band (the carrier frequency). General, this can be avoided by selecting the reference wave far from the sample and without being distorted. However, in practice the finite spatial coherence of the electron source will limit this free selection of the reference wave. In this situation, the undistorted reference hologram should be used for finding out the real center of the side band [15].

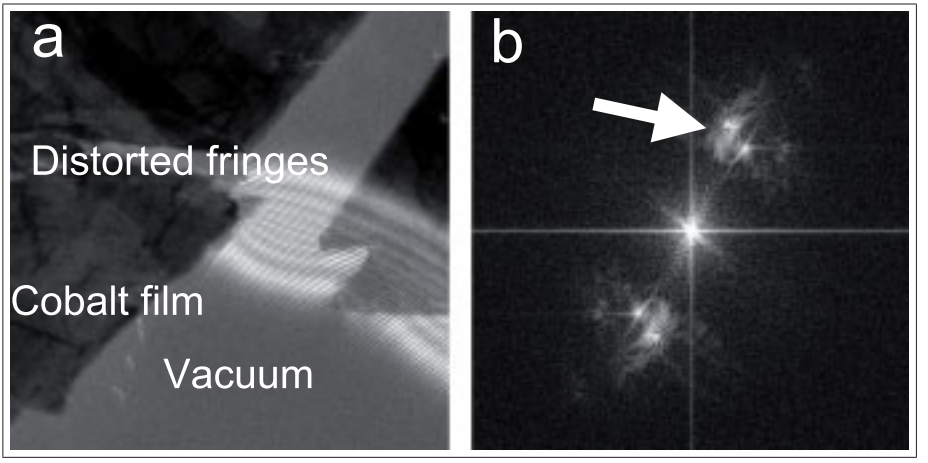

Figure 2.9. (a) Electron hologram and (b) the corresponding Fourier spectrum image of a cobalt film. Both the interference fringes and the side bands are strongly distorted by the magnetic field of the sample.

2.2.4 Phase image processing

After successful reconstruction of the phase image from the electron hologram, some further phase image processing could be performed to get a better visualization of the phase information. The mostly used phase processing methods in this work are phase unwrapping and phase amplification.

Phase unwrapping

For a raw phase image, the dynamical range is always limited in $[-\pi, \pi]$ or $[0, 2\pi]$. This is due to the following reasons: During the reconstruction, after

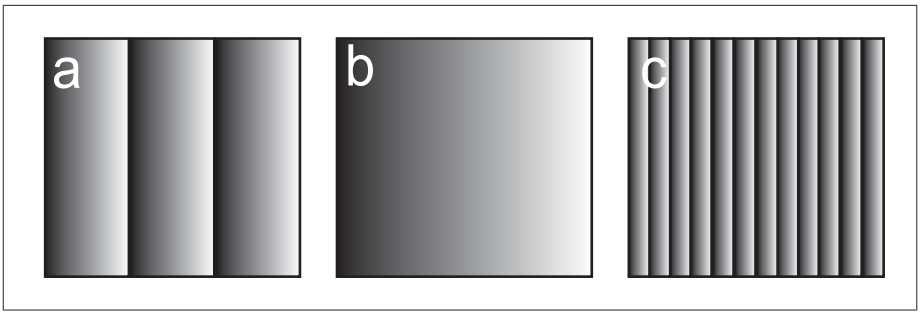

Figure 2.10. Simulated phase images with true dynamical range from 0 to 6π: (a) wrapped phase image, the dynamical phase range is limited to [0, 2π]; (b) unwrapped phase image; (c) amplified phase image ($4\times$).

one of the side bands is selected and an inverse Fourier transform is applied to it, a complex image which represents the object wave Ψ_{obj} in Eq. 2.18 will be acquired. Subsequently the phase part is separated from this complex image with the operation:

$$\Psi_{obj} = \arctan \frac{I}{R}, \tag{2.22}$$

where R and I represent the real and imaginary part of the complex image, respectively. From Eq. 2.22 we can see that the phase is constrained to the interval $[-\pi, \pi]$ or $[0, 2\pi]$ due to the arctan function. If the dynamic range of the real phase is larger than 2 π, then the interpretation of this phase image is difficult and not suitable for further analysis. The true phase dynamical range should be reconstructed from the wrapped phase image by means of the phase unwrapping algorithm. Figure 2.10a and b show a simulated phase image before and after the phase unwrapping. Both images are visualized by 256 gray levels and the true phase dynamical range is $[0, 6\pi]$. In the wrapped phase image the maximum displayed phase value is limited to 2π, which is represented by the maximum gray value 255 (white). The whole dynamical range is wrapped into three shorter ranges with $[0, 2\pi]$. After phase unwrapping, the 256 gray level values are rearranged to represent the true phase range $[0, 6\pi]$. The phase jump at 2π disappears as shown in Fig. 2.10b.

An example of the phase image before and after phase unwrapping is given in Fig. 2.11. The sample is again the Au/ZnMnTe nanowire as given in Fig. 2.5. Since the gold at the top of the nanowire is a sphere, the thickness and the phase shift due to the mean inner potential are continuously increased from the edge to the center region. The line profile along the wrapped phase image indicates that the phase steps at 2π and then goes back to zero. A phase jump is obtained and causes an artificial discontinuity. After unwrapping, the phase jump is removed (Fig. 2.11b).

The basic procedure for a two-dimensional phase unwrapping is to perform a phase scan pixel by pixel [26]. If the phase difference between the adjacent pixels exceeds some preset threshold, then the next pixel value will be automatically added by 2π. In a real phase image, the presence of noise can cause serious problems. Some advanced phase unwrapping algorithms, e.g. a combination of Fourier techniques, can help solve this problem [27].

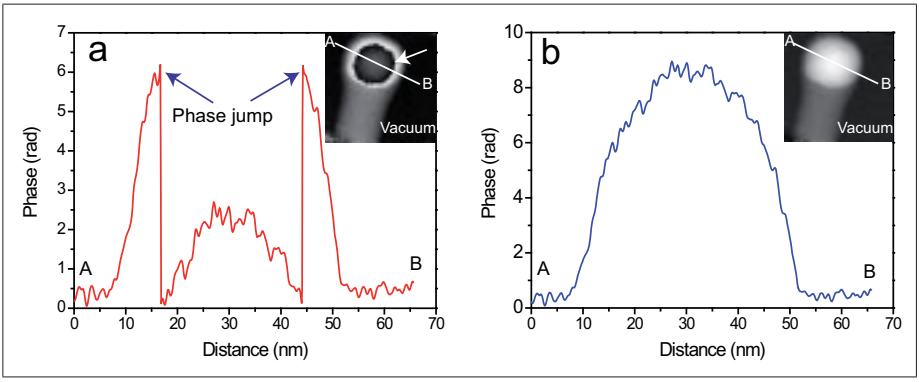

Figure 2.11. Phase images and the corresponding phase profiles of an Au/ZnMnTe nanowire: (a) before and (b) after the phase unwrapping.

Phase amplification

Contray to phase unwrapping, phase amplification is another phase processing technique for visualizing small phase shifts. A simulated amplified phase image is shown in Fig. 2.10c. Contour mapping is a similar technique in order to display small phase shifts. Here, we will not describe the methods in detail.

2.2.5 Resolution of phase image

The purpose of electron holography is to retrieve the desired information from the phase image of the electron exit wave. During the electron hologram formation, recording and reconstruction, the ideal electron exit wave is convoluted with some instrumental limitations. Thus, the resolution of the ultimate phase image becomes one of the crucial factors for the materials analysis by electron holography. Two different resolutions are included in the phase image, the lateral resolution and the phase resolution (phase detection limitation).

Lateral resolution

The lateral resolution of the phase image depends on two factors: The resolution of the microscope and the fringe spacing of the recorded hologram. As a TEM-based method, the lateral resolution of electron holography is firstly limited by the resolution of the microscope, which is mainly determined by the resolution limit due to the action of the objective lens. In high-resolution electron holography and some applications of medium-resolution electron holography, a conventional objective lens is used for focusing electrons and the objective lens resolution is at the atomic level. For example, the point resolution for the JEOL 2200FS microscope equipped with an ultra-high resolution pole piece is 0.19 nm. For the other applications of medium resolution electron holography which need a larger field of view or an environment without any external magnetic field, the conventional objective lens is switched off and an objective mini lens is used for focusing. Due to the large spherical aberration, the resolution of such objective mini lens is poor. The lateral resolution using the objective mini lens of the JEOL 2200FS is limited to 2 nm.

The lateral resolution of the phase image not only depends on the influence of the objective lens, but also on the fringe spacing of the hologram. This can be explained as follows.

During the reconstruction, one of the side bands is selected by a numerical aperture. According to Fourier transform theory, the resolution of the phase image in real space d_{res} is associated with the radius of this numerical aperture q_r ($d_{res} = 1/q_r$). In order to reconstruct the phase image correctly, the selected side band should not overlap with the center band. Then the radius of the aperture q_r is limited. For strong amplitude and phase objects where the amplitude A(r) is strongly modulated by the scattering potential, the center band can be extended as far as $\frac{2}{3}q_c$ (the blue dash ring shown in Fig. 2.12), where q_c denotes the distance from the center band to the side band (carrier frequency) [28, 29]. In this case, q_r should be smaller than $\frac{1}{3}q_c$. In another extreme case, as e.g. pure phase objects the amplitude of the scattering wave will not be changed. Then after the Fourier transform the constant amplitude A becomes a delta function $\delta(q)$. So the numerical aperture radius could be as large as the whole q_c.

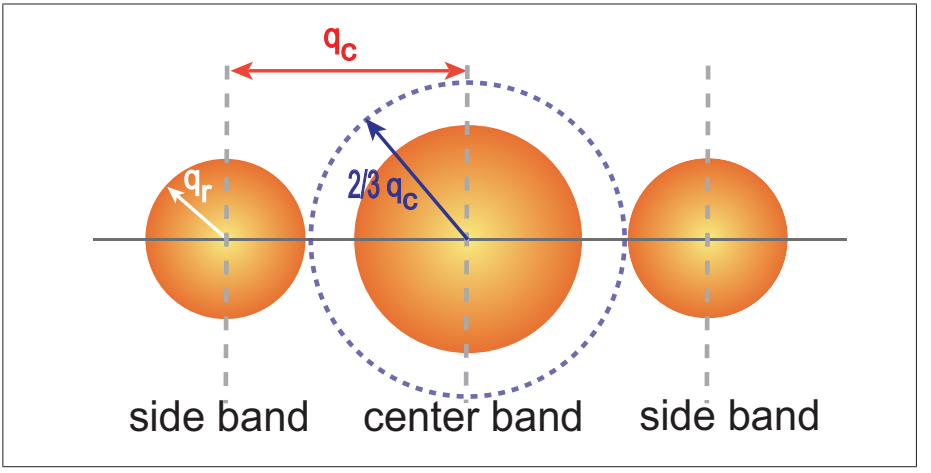

Figure 2.12. Limitation of lateral resolution of phase image in Fourier space. The parameter q_c is the distance between the side band and the center band, and q_r is the radius of the numerical aperture.

For example, working at the JEOL 2200FS in low-mag mode (focusing by the objective mini lens), a reasonable fringe contrast can be achieved with the fringe spacing d of 9.7 nm (carrier frequency $q_c = 1/9.7$ nm^{-1}). This means, the resolution of the reconstructed phase image is in the range from

9.7 nm to 29.1 nm, depending on the type of object. Compared with the point resolution of the objective mini lens of about 2 nm, we can find that in low-mag mode, the lateral phase resolution is actually limited by the fringe spacings, but not by the resolution of the objective mini lens.

Another important factor associated with the fringe spacing is the total lens magnification. For digital recording such as by CCD camera, according to the sampling theory, each of the fringes should be recorded at least by four pixels. For a given CCD camera, the pixel size is fixed. For example, a Gatan 794 slow-scan CCD camera (1k x 1k pixels) which was used in this work has a pixel size 24 μm $\times$ 24 μm. Thus, 4 pixels correspond to a physical distance of 96 μm on the CCD camera. The minimum fringe spacing d associated with the object is then given by

$$d = \frac{96}{M}\ \mu m, \tag{2.23}$$

where M is the total lens magnification.

For JEOL-2200FS microscope working in low-mag mode (Lorentz mode), the preset maximum magnification is M=15 k$\times$. According to Eq. 2.23, the minimal fringe spacing is limited to 6.4 nm due to total lens magnification. Further improvement of the magnification can be gained by using the free lens control. However, the contrast of the interference fringes will become poor. For microscopes equipped with a post-column energy filter, an additional magnification can be achieved.

Phase resolution

The phase resolution, which means the minimum phase shift which can be detected by electron holography is another important parameter for the applications of electron holography. For example, the mean inner potential of a Si crystal is 12.57 V. Thus, a thin Si film with a thickness of 5 nm will cause a phase shift of 0.458 rad for 200 keV incident electrons (A detailed discussion is given in chapter 5). In order to image such phase shift, the phase resolution should be better than 0.458 rad. The detection limit of the

electron phase shift is given by

$$\phi_{limit} = \frac{\sqrt{2}\ SNR}{C\sqrt{N}}, \tag{2.24}$$

where SNR is the Signal to Noise ratio, C is the fringe contrast and N is the number of electrons collected per reconstructed pixel [30].

In ideal case, intensity distribution of a hologram is given by Eq. 2.20. In practice, the intensity will be damped by several factors. The hologram intensity is then expressed as

$$I_{HOLO}(\vec{r}) = 1 + A(\vec{r})^2 + 2C{\cdot}A(\vec{r})cos(2\pi\vec{q_c}{\cdot}\vec{r} + \phi(\vec{r})), \tag{2.25}$$

where C is the fringe contrast and defined as

$$C = \frac{I_{max} - I_{min}}{I_{max} + I_{min}} \tag{2.26}$$

I_{max} and I_{min} are the maximum and minimum intensity of the fringes. The fringe contrast of an experimental hologram is determined by [28]

$$C = |\mu|\ C_{inel}C_{inst}C_{MTF}, \tag{2.27}$$

where $|\mu|$ is the degree of the coherence, C_{inst} is the contrast loss due to the electron energy loss by inelastic scattering, and C_{inst} is the contrast loss due to instabilities of the object, the biprism and the instrument as well as the environmental magnetic and electric field distortion. The last parameter C_{MTF} is the contrast loss due to the modulation transfer function (MTF) of the CCD camera.

On the other hand, the average number of collected electrons N in Eq. 2.24 is determined by [28]

$$N = -\ln(|\mu^{sc}|)\frac{B}{ek^2}\frac{1}{(2q_{max}\omega)^2}\varepsilon\tau DQE, \tag{2.28}$$

where μ^{sc} is the degree of spatial coherence, B is the illumination brightness, k is the wave number, q_{max} is the lateral resolution, ε is the ellipticity of

illumination, τ is the exposure time, and the last parameter DQE is the detection quantum efficiency of the CCD camera.

2.3 Experimental techniques

In this section, the experimental techniques for electron holography are described. The conventional TEM investigations and the electron holography experiments in this work were performed on a JEOL 2200FS transmission electron microscope installed at the Institute of Physics of Humboldt University of Berlin. In Fig. 2.13 the experimental setup is shown.

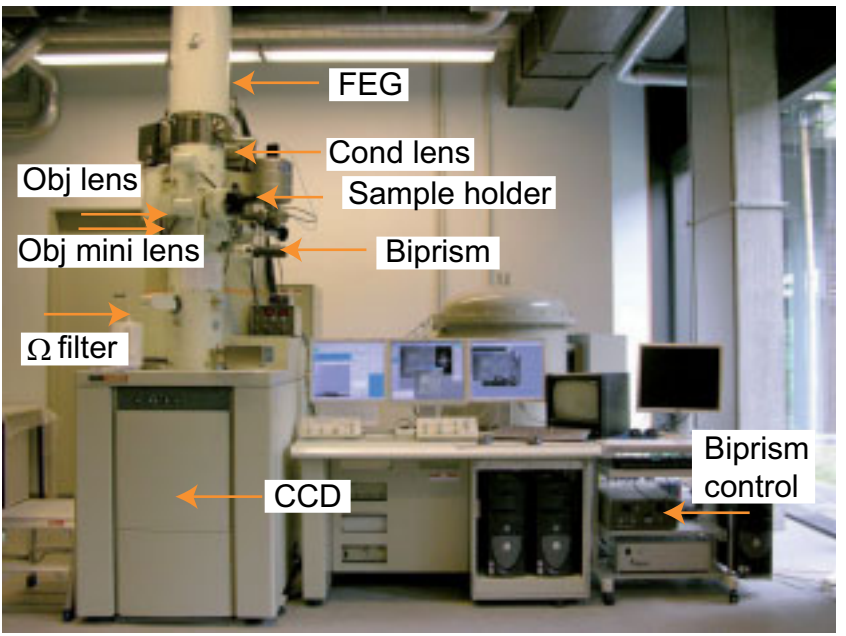

Figure 2.13. JEOL 2200FS transmission electron microscope at HU-Berlin.

2.3.1 Electron source

As a phenomenon of wave interference, the formation of an electron hologram requires electron sources with high brightness and high coherence. The most

commonly used electron sources in TEM are thermionic emission electron guns and field emission (cold FEG and thermal FEG) electron guns. Table 2.1 provides an overview of the main characteristics of various electron gun systems [31]. First, the process of the electron emissions is briefly described. Then, the characteristics of different electron guns are compared. Finally, their influence on electron holography experiments is discussed.

	Thermionic emission		Field emission		
			Thermal FEG		Cold FEG
	W	LaB_6	ZrO/W(100)	W(100)	W(310)
Brightness(A/cm^2sr)	$\sim 5 \times 10^5$	$\sim 5 \times 10^6$	$\sim 5 \times 10^8$	$\sim 5 \times 10^8$	$\sim 5 \times 10^8$
Source size	50μm	10μm	0.1-1.0μm	10-100nm	0-100nm
Energy spread(eV)	2.3	1.5	0.6-0.8	0.6-0.8	0.3-0.5
Pressure(Pa)	10^{-3}	10^{-5}	10^{-7}	10^{-7}	10^{-8}
Temperature(K)	2800	1800	1800	1600	300
Current (μA)	~ 100	~ 20	~ 100	20-100	20-100

Table 2.1. Comparison of characteristic parameters of various electron guns [31].

Electron emission

Electrons are unable to escape from the surface of a metal or compound unless an external energy helps to overcome the work function ϕ (the difference between the Fermi energy and the potential at infinity). Several sources can provide such kind of external energy to emit electrons, such as heating (thermionic emission), external strong electric field (field emission), charged particles (secondary emission) or photons (photo-electric emission). In TEM thermionic emission and field emission guns are comonly used.

Thermionic emission When a metal is heated, the Fermi distribution at the Fermi level of the metal will be broadened. If the heating temperature is sufficiently high, the electrons in the tail of the Fermi distribution can obtain enough kinetic energy to overcome the work function and will be emitted to the vacuum. This is the so-called thermionic electron emission [13]. Thermionic emission guns are cheap and simple to maintain. They are

widely used in conventional TEM systems. However, due to the large source size and the high working temperature (see Table 2.1), both the spatial and temporal coherence of thermionic emission gun are limited. Thus in practice, they are not used for electron holography experiments.

Cold field emission If a very intense external electric field E is applied to the metal, the potential barrier between the metal and vacuum boundary will become very thin and large quantities of electrons can be emitted to the vacuum by means of quantum tunneling effect. This kind of electron emission is called field emission (or cold field emission) [13]. Due to the small source size and the low working temperature (room temperature), a cold field emission gun has extremely high spatial and temporal coherence. The disadvantage is that cold field emission gun need a regular maintenance which is called flashing procedure to remove the contamination on the surface of the emitter [31].

Thermal field emission The current density of thermionic emission depends on the materials work function ϕ. When an external electric field E is applied to the material, the work function ϕ will be decreased due to the combination of the image potential and the applied field [32].

$$\phi - \phi_{eff} = \sqrt{\frac{e^3 |E|}{4\pi\varepsilon_0}}, \tag{2.29}$$

ϕ_{eff} is the effective work function and ε_0 is the vacuum permittivity. This phenomenon is called Schottky effect. According to the Schottky effect, if a strong electric field is applied to the emitter, a lot of electrons still can be emitted even at a much lower temperature (1600-1800K) than the thermionic emission temperature. An electron gun working according to this emission mechanism is called thermal field emission gun or Schottky electron gun.

Thermal field emission guns keep the good characteristics like the high degree of spatial and temporal coherence as cold field emission guns, but they are much easier for maintaince. In the JEOL 2200FS microscope, a thermal field emission gun with a ZrO/W(100) emitter is installed.

Coherence

Coherence, which describes the correlations between the phase of the wave, plays an important role in electron holography. In general, the concept of coherence can be divided into temporal coherence and lateral coherence, while the former is determined by the source monochromaticity and the later are determined by the size of the emitter. Figure 2.14 presents a simple model of temporal coherence and spatial coherence.

Temporal coherence In the model for temporal coherence, we can assume that the electron source is an ideal point source, but the emitted wavelength λ (or wave number k_0) will change with time. This means, the source has an energy spread ΔE. For example, if the emitted wavelength is λ_1 and λ_2 at moment 1 and 2, respectively, then we will find at each of the moments, two scattered objective wave $\Psi(A)$ and $\Psi(B)$ will form a set of interference fringes on the screen without any loss of contrast. However, at different moment the interference fringes will be shifted, since the fringe spacing and fringe positions depend on the wavelength λ. Then during the total exposure time, the fringe contrast will be decreased while the intensity of the two set of fringes will be summed up.

Fortunately, in reality the temporal coherence of the electron source has tiny effect on the fringe contrast. This is due to the high stability of the electron source with small energy spread [28]. For example, the energy spread ΔE of JEOL 2200FS (FEG, ZrO/W(100) Schottky emitter)is only 0.7 eV when the microscope works at an accelerating voltage of 200 kV. This means, the maximum deviation of the wavelength $\Delta\lambda/\lambda$ is only 3.5×10^{-6}, as well as the maximum deviation of fringes. Even for thermal emission electron guns with a higher energy spread $\Delta E = 3$ eV, the fringe deviation is only 1.5×10^{-5} of the original fringe spacing. Therefore, the effects of temporal coherence on the fringe contrast can be neglected.

A more quantitative description of temporal coherence is given by the van Cittert-Zernike theorem, where the temporal coherence function $\mu^{tc}(n)$

is defined as

$$\mu^{tc}(n) = \int_{source} s(\kappa) exp(i2n\pi\kappa/\kappa_0) d\kappa, \tag{2.30}$$

where $\kappa = k - k_0$ is the difference between the nominal wave number and the real wave number [28].

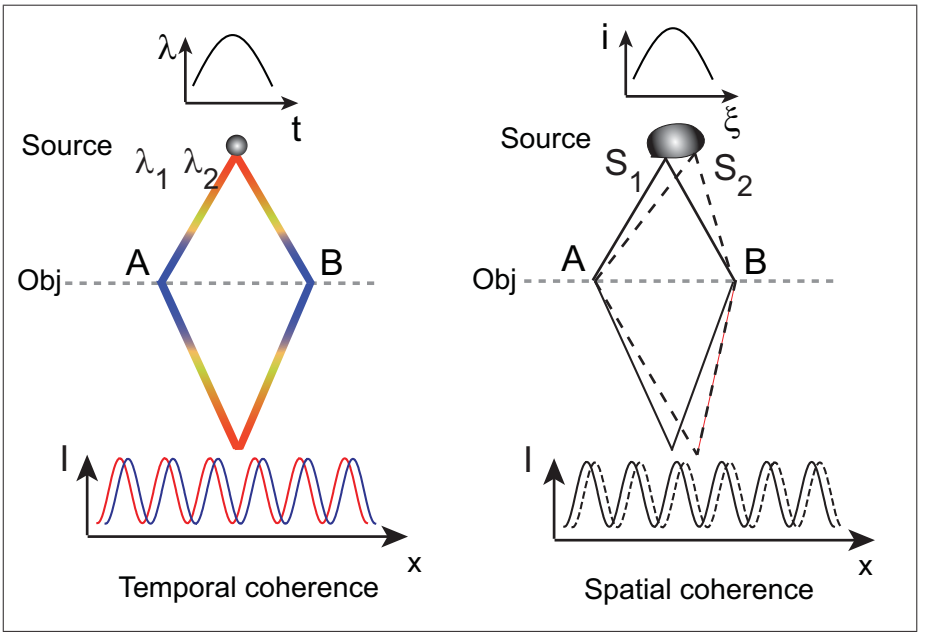

Figure 2.14. Schematic illustration of temporal coherence and spatial coherence.

Spatial coherence Compared with temporal coherence, spatial coherence has much larger effect on the fringe contrast. As shown in Fig. 2.14, we assume that the electron source is a monochromatic source with a spatial distribution i(s). Then each point of the source will separately emit a coherent wave and form fringes on the screen. This will cause a relative shift of the fringes emitted from different positions of the source. Thus, the total fringe contrast will be decreased. A detailed analysis has been given by H. Lichte and M. Lehmann in Ref. [28]. Due to partial spatial coherence, the

intensity of the interference fringes is given by

$$I(x) = 2I_0\{1 + |\mu^{sc}| \cos(2\pi q_c x + \Phi(s))ds\}, \tag{2.31}$$

where

$$|\mu^{sc}| = \mu^{sc} e^{i\Phi(s)} \tag{2.32}$$

is defined as the degree of spatial coherence. According to van Cittert-Zernike theorem (see Ref. [28, 33]),

$$\mu^{sc} = \int_{source} s(i) e^{i\Phi} ds, \tag{2.33}$$

where s(i) is the spatial distribution of the source. Equation 2.33 directly reflects the fact that the spatial coherence is connected with the Fourier transform of the spatial distribution of the source. Thus, only a FEG with small source size (see Table 2.1) can provide sufficient spatial coherence for electron holography experiments.

Since smaller size yields a better coherence, single atom emitter can provide the brightest and most coherent electron beam. Recently a lot of progresses have been achieved in this field [34]. It can be expected that such single atom emitters will provide electron beam with full spatial coherence for electron holography experiments in the future.

2.3.2 Illumination system

Ellipital illumination

For most of the TEM experiments which are performed in parallel illumination mode, a circular illumination is necessary. This can be achieved by careful adjustment the condenser lens stigmators. In electron holography experiments, a highly astigmatic elliptical illumination is often used. This can be explained as follows.

First, in order to guarantee a good coherent illumination on the specimen, the beam should be spread as far as possible by defocusing the condenser lens. After that, an only very small fraction of the source electrons (central part)

will illuminate the sample. This part of electrons has a better coherence. Unfortunately, the spread of the beam will decrease the coherent current density. Subsequently the fringes intensity will be decreased. This can be compensated by an elliptical illumination [21, 35].

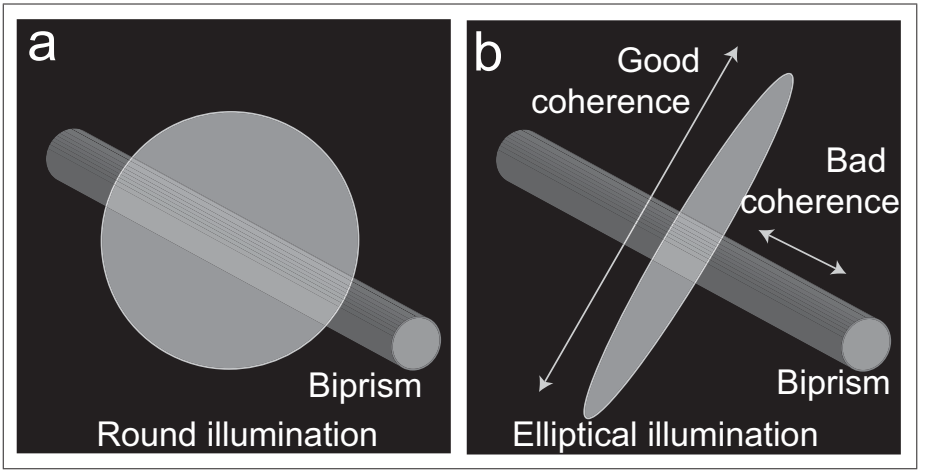

Figure 2.15. Different illumination conditions in TEM: (a) conventional round illumination; (b) elliptical illumination for electron holography.

In off-axis electron holography, the high degree of coherence is only needed in one direction, which is perpendicular to the biprism [21]. This is because the electrons only interfere with those which are also along this direction under the deflection of the biprism. And this direction is called as "good coherence" direction while the other direction (parallel to the biprism) is called as "bad coherence" direction. Since the total coherent current is fixed, we only can redistribute the current. The current along the "good coherence" direction will be increased while the current along the other direction will be decreased. This is the elliptical illumination condition for off-axis electron holography, as shown in Fig. 2.15. In practice, it can be achieved by adjusting the two stigmators of the condenser lens. First, one of the stigmator is set close to the maximum value to get a large astigmatism. Then the other stigmator will be carefully adjusted to make the major axis of the ellipse exactly perpendicular to the biprism, as shown in Fig. 2.15b. Then, an illumination with optium spatial coherence will be obtained while keeping

the high beam current. A more detailed discussion of elliptical illumination in electron holography is given by M. Lehmann in ref. [35].

2.3.3 Biprism

The biprism (wire electrode) is normally located near the first image plane for deflecting the beam in off-axis electron holography. As the selected area aperture is located at this plane, one of the choices is to use the selected area aperture as the biprism holder. In this case, the first image plane should be lowered. In the JEOL-2200FS microscope, the biprism is built in a separate specially designed biprism holder. The biprism holder can be easily inserted and retracted from the column, so it will not affect the other conventional TEM operations. A thin platinum wire with 0.6 μm diameter and 5 mm length is installed at the top of the holder as a biprism (wire electrode). The holder is designed in such a way that the biprism can be easily moved in two horizontal directions and can be rotated in-plane by 180°. The movable range for the x direction (biprism axis direction) and y direction is $\pm$ 1.5 mm and $\pm$ 1.0 mm, respectively. This kind of design provides maximum flexibility for the holography experiment, since the biprism can be easily aligned parallel to the interface between the vacuum and the specific sample area. On the other hand, the stability of the biprism will be slightly decreased when it is rotated away from the axis of the holder. So in practice, the rotation of the biprism away from the holder axis can be avoided by careful alignment of the sample when it is mounted into the sample holder. If it is not possible, we can rotate the biprism after the sample is inserted into the column.

The biprism is controlled by a separated control unit, including a power supply. The maximum voltage applied to the biprism is 320 V. If the biprism is exactly located in the first image plane, the electron hologram can not be formed. Then the first image plane should be lowered by changing the lens current. In the JEOL 2200FS microscope, there are four pre-defined mode for holography with different lens current setting stored in the computer, as shown in Table 2.2.

Fringe spacing and fringe width are two of the most important parameters

Preset mode	Magnification
HOLO-L	×1000 to ×15 k
HOLO-M	×100 k to ×250 k
HOLO-M2	×10 k to ×40 k
HOLO-H	×300 k to ×1.5 M

Table 2.2. Preset electron holography mode in JEOL 2200FS.

for the applications of electron holography. As it was already mentioned, finer fringe spacing corresponds to a better lateral resolution, while wider fringe width can cover more interesting area to be investigated. The two parameters can be improved by increasing the biprism voltage. Due to the limited spatial coherence of the electron source, the biprism voltages can not be infinitely increased, otherwise the fringe contrast will become very poor. The fringe spacing, the fringe width as well as the fringe contrast as a function of the biprism voltage have been experimentally measured for the JEOL-2200FS. The measurement was performed in low-mag mode (Lorentz mode) with a magnification of 12 k×.

As shown in Fig. 2.16, both the fringe spacing and the fringe contrast are decreased with increasing biprism voltage. When the biprism voltage exceeds 70 V, the fringe contrast drops faster than the fringe spacing. So the best working voltage in Lorentz mode is between 70 V to 80 V. The fringe spacing is in the range of 12.09 nm to 10.74 nm, while the fringes contrast is between 25.27% and 19.79%.

simultaneously the fringe width is linearly increased with increasing biprism voltage, as shown in Fig. 2.17. When the biprism voltage is set between 70 V to 80 V, the corresponding fringe width is varying from 2.62 μm to 3.09 μm.

2.3.4 Recording system

The commonly used recording systems in TEM are photo-film, image plate and CCD camera. Photo-film is the oldest recording medium and it is very economical. However, it has several obvious shortages, such as the low op-

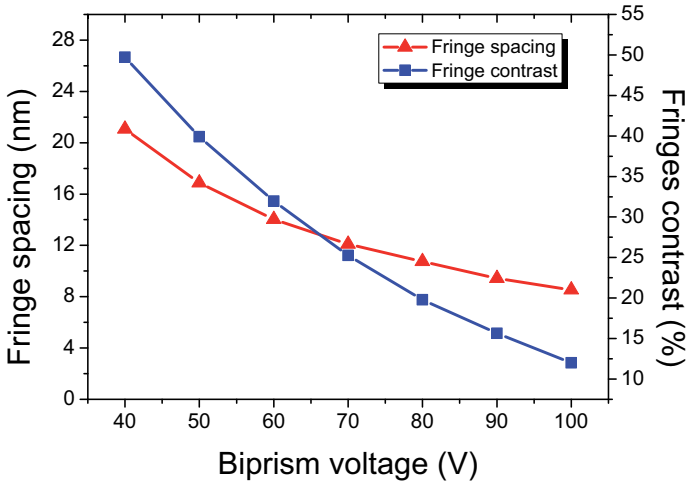

Figure 2.16. Fringe spacing and fringe contrast of electron hologram as a function of biprism voltage. (JEOL-2200FS, low-mag mode with magnification 12k×.)

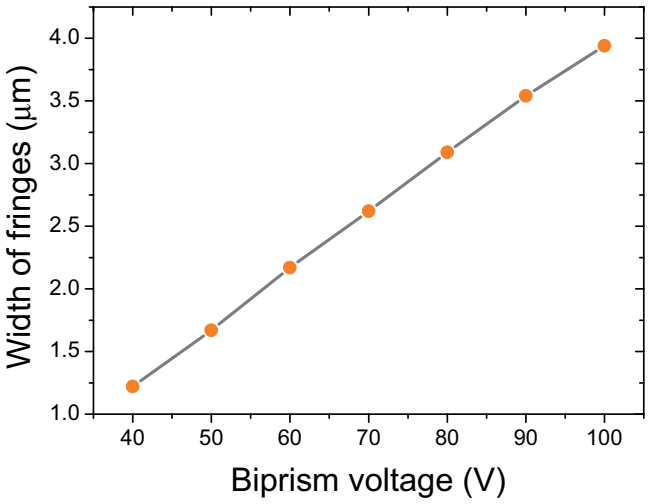

Figure 2.17. Fringe width of electron hologram as a function of biprism voltage. (JEOL-2200FS, low-mag mode with magnification 12k×.)

tical density, low signal/noise ratio (S/N) and narrow dynamical range [31]. Additionally, the photo-film emulsion on a polymer support can contaminate the high vacuum instrument as well as the specimen. Today, photo-film is replaced by image plate and CCD camera.

image plate

The image plate was originally developed for recording X-ray signals with high-sensitivity. Later it was adapted for electron detection [31]. Compared with photo-film, an image plate has a very good linearity between the incident electron intensity and the intensity of the output signal. An image plate also has a high sensitivity and a large dynamical range. It can be used for recording TEM images with high quality. In the JEOL 2200FS microscope at HU-Berlin, a DITABIS image plates are installed to replace the conventional photographic films. Unfortunately, the disadvantage of an image plate is that the image can only be read out in a special instrument outside the microscope. This limits the application of image plates for on-line operation, such as for electron holography. During the investigations, the phase image should be reconstructed immediately after the acquisition of the hologram to check if it contains the desired information. Therefore, image plate can only be used for some extreme cases of electron holography investigations.

CCD camera

In this work, we use a Gatan 794 1k $\times$ 1k slow scan CCD (charge-coupled device) camera for both recording of conventional TEM images and of electron holograms. CCD was first invented by Boyle and Smith at Bell labs in 1970 [36]. The core part of CCD is an array of isolated metal-oxide-semiconductor (MOS) capacitors (pixel). When photons or other ionizing particles impinge on the CCD electron-hole pairs are generated in Si substrate. The generated electrons are collected and accumulated in the potential well in each of the pixel until they are read out. The total amount of accumulated electron charges is proportional to the number of incident photons before the potential well is saturated [37]. With this optic-electronic transformation

characteristic, CCD is widely used as sensor in optical image devices. The first application of CCD in electron detection is reported by Chapman et al. in 1982 [38]. They used a 100 x 100 pixel CCD directly exposed to the electrons in a TEM. However, this caused several problems. First the energy of electrons used in TEM (80 keV to 400 keV) is much higher than the production energy of electron-hole pairs in Silicon (3.64 eV). Then, one incident electron can generate several tens of thousands electrons or more. This means when the CCD is directly exposed to the electrons, a very high sensitivity is given. This also means that the pixels are very easily saturated [37]. As Chapman have reported in their first experiment, the saturation level is only 45 electrons with 100 keV incident energy [38]. Second, the high energy electrons will cause serious radiation damage to the CCD.

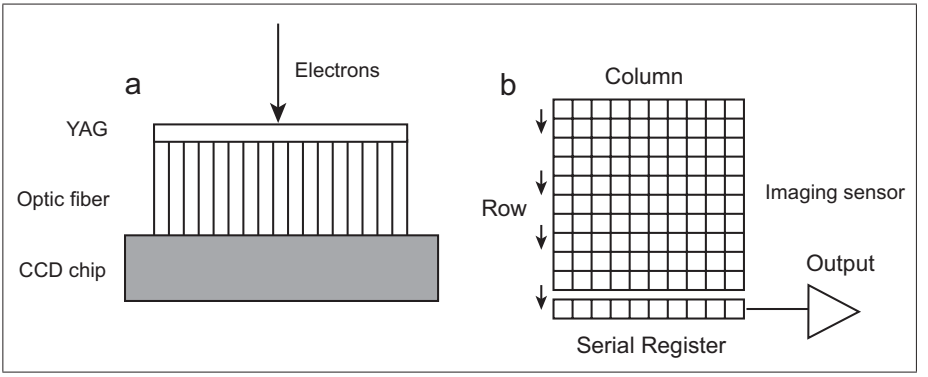

Figure 2.18. CCD camera for the detection of electrons in a TEM: (a) Schematically illustration of CCD camera; (b) Working mode for the read out of electron charges in slow-scan mode.

To avoid these problems, J.M. Zuo and J.C.H. Spence first designed and tested an indirect route for electron detection by CCD in 1988 [39]. The incident high-energy electrons are transformed to a light signal by a scintillator. Then the photons are further transferred to the CCD sensor through the optical coupling system. The most commonly used optical coupling system in TEM-CCD cameras is an optical fiber which has a high-efficiency. The general principle of optical fiber coupling CCD is shown in Figure 2.18a. The negative effect of this design is the electron propagation in the scintillator and

the optical coupling system will decrease the resolution [39]. Additionally, the optical fiber coupling can cause some distortions in the final image and lead to a significant effect on the reconstructed phase image of the electron hologram. Fortunately, such distortions can be removed by using a reference hologram during the reconstruction, as it was already discussed.

Modulation transfer function (MTF) and detection quantum efficiency (DQE) of the CCD camera are two important parameters for electron holography experiments, since they directly determine the limit of the phase detection (see Eq. 2.24 and Eq. 2.27). A detailed description of the methods for measuring MTF and DQE of a CCD is given in Ref. [37].

Beam shutter

For slow scan CCDs, the charges in the pixel arrays are read out in a special way, as shown in Fig. 2.18b. First, the charges in the last row are shifted to the parallel register. After being amplified and digitized pixel by pixel, they will be output as electronic signal. Then the charges in the other rows are transferred down to the adjacent row. This will be repeated until all of the charges are shifted to the parallel register from the last row. It takes some time for the whole data read out. During this time, the beam should be blocked by a shutter to avoid the multi-exposure (except for very few modern TEM-CCD such as Gatan DualVision camera, the CCD is operated in a higher speed that there is no need for a shutter). It is difficult to fabricate a high speed mechanical shutter on a CCD. Normally the beam deflectors of the TEM are used as a CCD shutter. For the JEOL 2200FS, two beam deflectors can be used, the gun deflector and the projective lens (PL) deflector. The difference between both is that they are located in different positions in the column. The gun deflector is located above the sample and the biprism while PL deflector is below of both. The shutter will be automatically closed when the CCD camera has been inserted into the column and the fluorescence screen is lifted up. It will only be opened during the exposure time and then it will be closed again for charge read out. In practice, it was found that both deflectors have different effects on the fringe contrast as shown in Fig.

2.19. Both holograms are taken for the same optical conditions and same exposure time. The contrast of the hologram recorded with gun shutter is very poor due to some distortions (see Fig. 2.19a). While the hologram recorded with PL shutter has a much better contrast. This could be due to the following reasons. As the biprism is located below the gun shutter, it is only illuminated by the electrons during the short exposure time. The sudden exposure to the electron beam can cause some variation of the biprism (or charging) and decrease of the fringe contrast. While using a PL shutter the biprism is always illuminated by the electron beam. In this situation the biprism has much better stability. Additionally, it can not be excluded that the gun shutter is unstable itself.

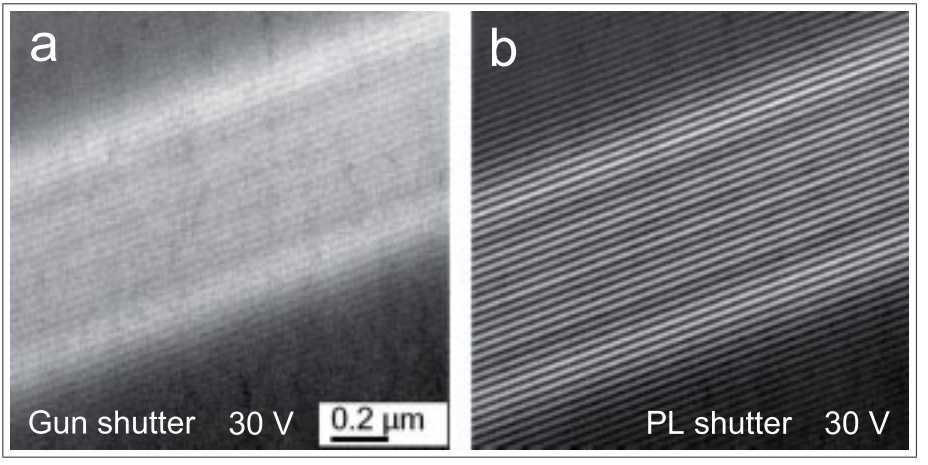

Figure 2.19. Electron holograms recorded with (a) gun shutter and (b) projector lens shutter.

2.4 Lorentz microscopy

TEM is an unique tool for the analysis of the microstructure and the composition of the modern materials with high resolution. Conventional TEM working modes can not directly image the magnetic structure of samples. The high concentration of the magnetic field of the magnetic lenses can de-

stroy the magnetic domain structure of the sample. The details are explained in the following.

The magnetic objective lenses used in TEM are composed of a pair of pole pieces (upper and lower) which are made from soft magnetic materials and a coil of copper wire around the pole pieces. When the current passes through the coil, the magnetic field will be generated between the gap of the pole pieces [40]. When electrons enter this magnetic field, they will be deflected by the Lorentz force

$$F = -e(v \times B), \tag{2.34}$$

where e is the electron charge, v is the electron velocity and B is the magnetic field. The magnetic lens is designed in such a way that the excited magnetic field is an inhomogeneous rotationally symmetric field. The electrons far from the axis will be deflected stronger than those passing through the center. Then parallel electrons are focused into a spot [41].

In a modern TEM, the sample is located between the upper and the lower pole piece of the objective lens, as shown in Fig. 2.20. The magnetic flux direction close to the sample is along the optic axis and perpendicular to the sample plane. This magnetic field could be as strong as 2 Tesla, then the magnetization of the most of magnetic samples is forced along the direction of the optic axis. Thus, the magnetic domain structure is destroyed and can not give any in-plane magnetic contrast.

In order to solve this problem, the objective lens should be switched off. In some older types of microscopes, the subsequent intermediate lens is used as a replaced objective lens for focusing the beam. However, the resolution is significantly decreased. Therefore in most of the modern TEMs as in the JEOL 2200FS, a special mini objective lens, which is located below the lower pole piece of the normal objective lens is installed for focusing the beam to keep a relatively high resolution. For example, the objective mini lens of the JEOL 2200FS microscope has a point resolution of 2 nm and Cs of 4600 mm. Then the residual magnetic field near the sample plane will be decreased to several hundreds of micro Tesla.

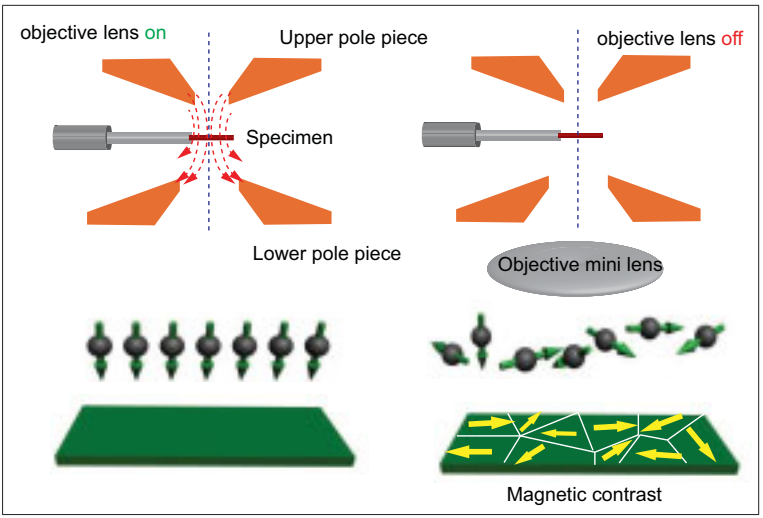

Figure 2.20. Two different working modes in TEM: (a) conventional mode; (b) Lorentz mode.

In Lorentz mode, when electrons interact with magnetic samples, they will be deflected by the Lorentz force which is connected with the magnetic flux of the samples, as shown in Fig. 2.21. The Lorentz force $\vec{F}$ is given in Eq. 2.34.

The direction of the Lorentz force is determined by Fleming's left hand rule. In the example as shown in Fig. 2.21, the electrons transmit through the sample from top to bottom and the magnetic flux is oriented perpendicular to the display. Thus the Lorentz force will deflect the electrons to the right. The deflection angle can be estimated as follows. If we assume the sample is a thin cobalt film with saturated density of the magnetic flux for bulk material of 1.87 T, the film thickness is 100 nm and the incident electrons energy is 200 keV. Considering the relativistic effect, the electrons velocity is given by

$$\upsilon = c[1 - \frac{1}{1 + \frac{E}{m_0 c^2}}]^{1/2}, \tag{2.35}$$

where E is the energy of incident electrons, m_0 is electron rest mass and c is the velocity of light. For electrons of an energy of 200 keV, the relativistic speed is 2.086×10^8 m/s. Then the electrons will transmit through the sample

within a time of

$$T = t/v = 4.794 \times 10^{-16} \text{ s} \tag{2.36}$$

Using Eq. 2.34, the Lorentz force F is calculated as 6.241×10^{-11} N. Thus, the lateral shift s of the electrons at the exit plane is given by

$$s = \frac{1}{2}\frac{F}{m}T^2 = 5.66 \times 10^{-3} \text{ nm}, \tag{2.37}$$

where m is the relativistic mass of electrons for 200 keV. The deflection angle is

$$\theta = \frac{s}{t} = 5.66 \times 10^{-5} \text{ rad}, \tag{2.38}$$

which is much smaller than the Bragg diffraction angle (cobalt (111) lattice plane 6.11×10^{-3} rad).

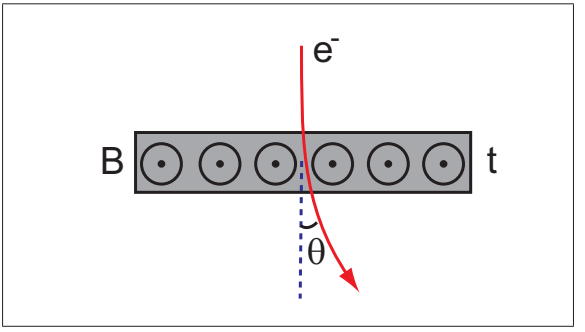

Figure 2.21. Deflection of electrons due to the magnetic field.

Due to the deflection of electrons by Lorentz force, the magnetic domain structure of magnetic samples can be visualized under special imaging conditions, such as large defocus (Fresnel method) or selecting only one of the deflected beams for imaging (Foucault method). In this work, we use the Fresnel method for imaging the domain structure of FeCo-based nanocrystalline alloys and compare the results with electron holography investigations.

The contrast formation of magnetic domains using the Fresnel method of Lorentz microscopy is illustrated in Fig. 2.22. We assume the sample being a thin magnetic film with a standard 180° magnetic domain structure. The magnetic flux has then opposite directions in adjacent domains. When

electrons transmit through the different domains, they will be deflected to the different directions (left or right) according to the magnetic flux directions in the domains. When the electrons leave the bottom surface of the sample, the intensity of the electrons will redistribute. However, due to the small deflection angle, this intensity redistribution can only be observed under large defocus imaging conditions. This means, the imaging plane is far below or above the sample plane. In the over-focused mode the convergent and divergent electrons will show bright and dark contrast at the position of domain walls, while in the under-focused mode, the contrast is inversed. The domain walls as well as the magnetic domain configuration could therefore be visible. An example of the magnetic domain structures of cobalt film is shown in Fig. 2.23.

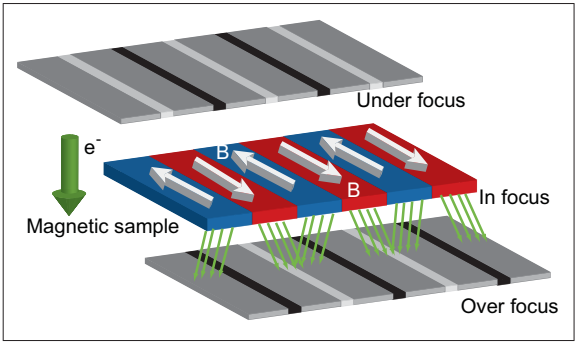

Figure 2.22. Formation of magnetic contrast in the Fresnel mode of Lorentz microscopy.

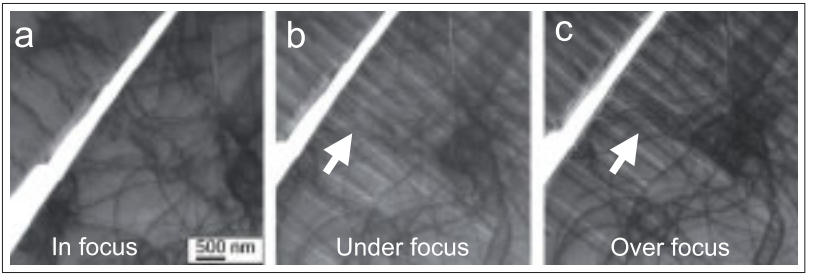

Figure 2.23. Lorentz microscopy images of cobalt (Fresnel mode): (a) in focus; (b) under-focus; (c) over-focus.

Chapter 3

Microstructure of FeCo-based alloys

FeCo-based nanocrystalline alloys are important soft magnetic materials for industrial applications. The alloys were fabricated by annealing an amorphous precursor at various temperatures above its primary crystallization point to form a nanocomposite state alloy. For further tailoring the soft magnetic properties by controlling the crystallization process, the correlations between microstructure and magnetic domain structure of the alloys processed at different heating temperatures have to be studied in detail. In this chapter we will present a detailed analysis of the microstructure of the alloys by combining different TEM techniques, including plan-view bright-field (BF) and dark-field (DF) imaging, selected area electron diffraction (SAED) and nano-beam diffraction (NBD) analysis, high resolution transmission electron microscopy (HRTEM) as well as scanning transmission electron microscopy using the high-angle annular dark-field detector (STEM-HAADF). The results will be used in chapter 4 for a fully discussion of the magnetic domain structure investigations by means of Lorentz microscopy and electron holography.

3.1 Introduction

3.1.1 Soft and hard magnetic materials

Ferromagnetic materials are widely used in industrial applications. According to the different hysteresis loop behavior, ferromagnetic materials can be divided into two categories: soft magnetic materials and hard magnetic materials. Soft magnetic materials are those who have a very low coercivity and can easily be magnetized and demagnetized in a weak applied field, while hard magnetic materials show an inverse behavior. The different magnetic hysteresis loops of soft and magnetic materials are compared in Fig. 3.1. Several important loop parameters have been marked on it, where the coercivity H_c is defined as the field required to reduce the magnetization to zero, $\mu = B/H$ is the permeability which describes the flux density B produced by a given applied field H, and B_m is the saturation flux density. Since soft magnetic materials have a very low H_c and a high μ, they are widely used as flux multiplies in various devices to generate or distribute the electric energy, such as in transformers, generators or motors [42].

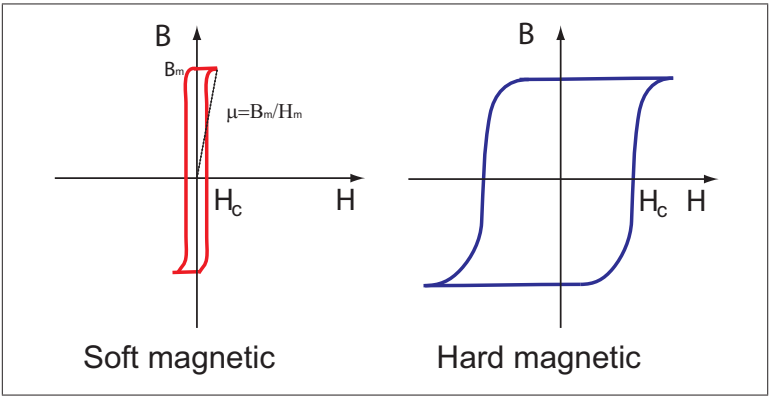

Figure 3.1. Magnetic hysteresis loops of ferromagnetic materials: (a) soft magnetic materials; (b) hard magnetic materials.

3.1.2 Coercivity and grain sizes

Coercivity of ferromagnetic materials strongly depends on their microstructure. Traditionally, good softmagnetic properties can be obtained from those crystalline materials with very large grain sizes ($D \geq 100\ \mu$m). This is due to the fact that bulk magnetic materials are subdivided into magnetic domain structures. Changes in overall magnetization in relatively low fields are almost due to the rearrangement of domains through domain wall motion [43].

In polycrystalline materials, the grain boundaries could act as impediments to the domain walls motion when the grain sizes exceeding $\sim 0.1-1\ \mu$m (the domain wall width). Then the coercivity is roughly inversely proportional to the grain size since larger grains can significantly reduce the number of grain boundaries [44, 45]. This $1/D$ dependence of coercivity and grain size is plotted in the right part of the famous Herzer diagram (Fig. 3.2) [45]. In general, fine grained systems are magnetically harder than large grained system. Thus, good soft magnetic properties of magnetic materials require very large grain sizes. However the generation of large grained system is not an economic way for industrial applications.

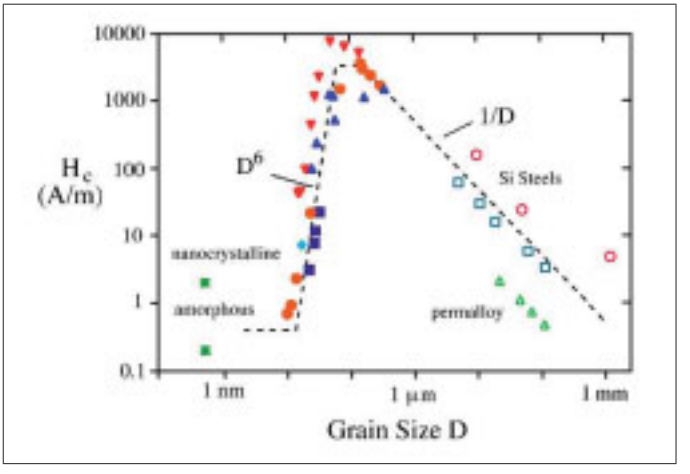

Figure 3.2. Herzer diagram of coercivity H_c versus grain size D [45].

Recently, amorphous alloys whose "grain" size is in the order of atomic

distance, and nanocrystalline alloys which are formed from randomly oriented ferromagnetic nano-crystals embedded in an amorphous matrix, provide a new way for achieving good soft magnetic properties.

Both amorphous and nanocrystalline alloys exhibit a different coercivity behavior compared with large grain systems. The coercivity of amorphous and nanocrystalline materials will be dramatically decreased with decreasing grain size. This D^6 dependence relationship is plotted in the left part of the Herzer-diagram (Fig. 3.2). The abnormal coercivity behavior of these amorphous and nanocrystalline alloy systems is due to the fact that the structural correlation length or grain sizes are smaller than the ferromagnetic exchange length which is in the order of the width of the domain walls. The local anisotropies are averaged out by the random orientation of different grains [45]. Nanocrystalline softmagnetic alloys are more interesting for commercial applications, since the chemical and structural variations at nanoscale allow a new dimension for tailoring the softmagnetic properties.

3.1.3 Nanocrystalline softmagnetic alloys

For technical applications, the following soft magnetic properties of nanocrystalline alloys are desired: High permeability μ (normally inversely proportional to the coercivity H_c), low hysteresis loss (the energy consumed in one cycle or the area inside the hysteresis loop), large saturation magnetization M_s and remnant magnetization M_r as well as high Curie temperature T_c. These properties could be achieved by carefully optimizing the intrinsic and extrinsic magnetic properties of the alloys, respectively. However they should be performed from different routes. The intrinsic magnetic properties, such as the saturation magnetization M_s and the Curie temperature T_c are mostly determined by the alloy chemistry and crystal structure of the ferromagnetic nano-crystal phase, while the extrinsic magnetic properties such as the magnetic permeability μ and the coercivity H_c, are determined by the microstructure of the alloys [44].

The first nanocrystalline soft magnetic alloy system was introduced by Yoshizawa, Oguma and Yamauchi in 1988. Subsequently, various nanocrys-

talline alloy systems like Fe-Si-B-Nb-Cu alloys (trade name FINEMET®) and Fe-M-B-Cu (M=Zr, Nb, Hf,...) alloys (NANOPERM®) have been developed. The relationship between the permeability μ_e (at 1kHz) and the saturation polarization for different softmagnetic materials are compared in Fig. 3.3.

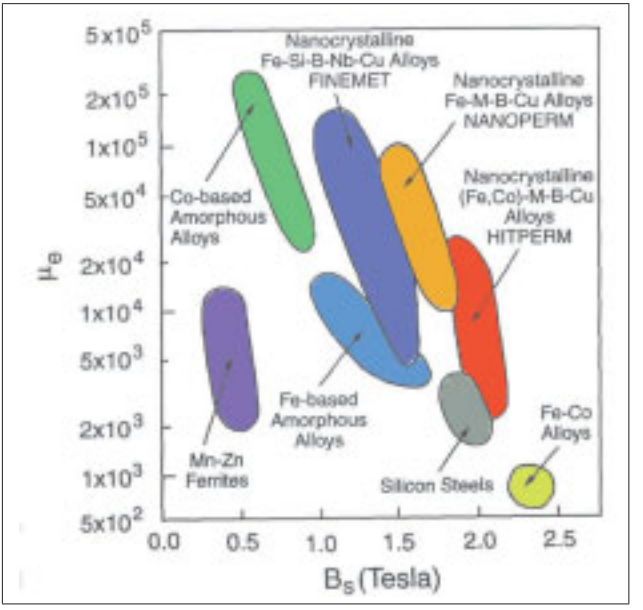

Figure 3.3. The relationship between the permeability μ_e (at 1kHz) and the saturation polarization for different softmagnetic materials. Adapted from Ref. [44, 46].

In this work, we are mainly focused on the particular nanocrystalline soft magnetic alloy system FeCo-M-B-Cu (M= Nb, Hf or Zr) with the trade name HITPERM®. It was first discovered by Prof. M. E. McHenry and Prof. D.E. Laughlin of the Carnegie Mellon University. In this kind of FeCo-based nanocrystalline alloy system, the late ferromagnetic transition metals Fe and Co are acting as the ferromagnetic nano-crystal phase, while the remaining early transition metal Nb and metalloid B are added to promote the glass formation in the precursor, and the noble metal element Cu acts as nucleation agent.

3.1.4 FeCo-based nanocrystalline alloys

Intrinsic magnetic properties

As mentioned, the intrinsic magnetic properties of nanocrystalline alloys like the saturation magnetization and the Curie temperature are mainly determined by the alloy chemistry. Therefore this should be taken into consideration during the alloy design. According to the Slater-Pauling curve [47], which illustrates the change of mean atomic magnetic dipole moment as a function of composition in the transition metal alloy system, FeCo alloys have the largest magnetic inductions (Fig. 3.4). Similar results have also been obtained from band structure theory calculations. Both Fe ($T_c = 770°C$) and Co ($T_c = 1100°C$) have high Curie temperatures, thus it is obvious that FeCo-based alloys are particularly suitable for high temperature applications with large saturation magnetization [44].

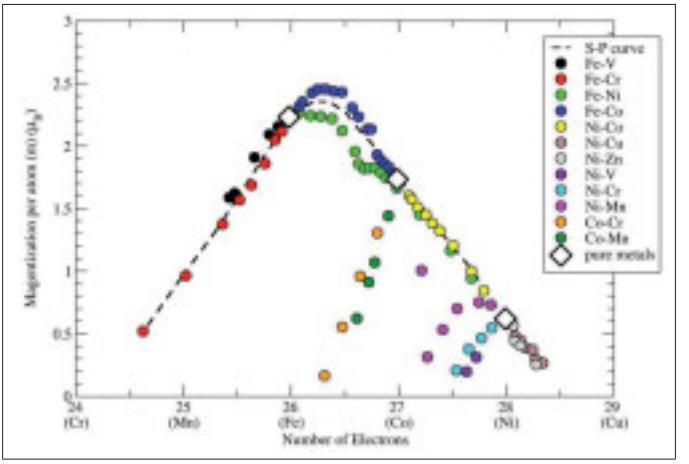

Figure 3.4. Slater-Pauling-curve for ferromagnetic alloys. It indicates that FeCo alloys have the largest magnetic inductions. Data taken from Bozorth [47] and adapted by K.R. Podolak [48].

External magnetic properties and fabrication

The external magnetic properties are determined by the microstructure of the nanocrystalline alloys, which should be optimized during the generation

process. The commonly used method is a two step synthesis method. First an amorphous precursor is fabricated, and then the nanocrystalline alloys are obtained by annealing the amorphous precursor. The fabrication procedure is schematically illustrated in Fig. 3.5.

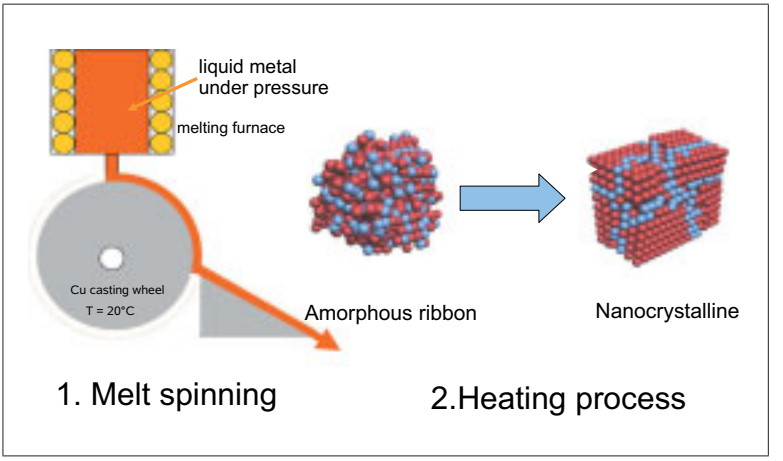

Figure 3.5. Illustration of synthesis of nanocrystalline softmagnetic alloys. An amorphous ribbon is first fabricated by melt spinning. Subsequently, the amorphous precursor is transformed to the nanocrystalline phase by annealing.

The amorphous ribbon was fabricated by a rapid quenching technique, which is commonly called "melt spinning". A molten charge with nominal composition $(Fe_{0.5}Co_{0.5})_{80}Nb_4B_{13}Ge_2Cu_1$, prepared by an arc melter was loaded into a quartz crucible which was placed approximately 1 cm over a copper spinning wheel. An overpressure of argon gas inside the crucible forced the molten charge out of the hole in the bottom of the crucible. Due to high surface velocity (rotating at 50 m/s) and high thermal conductivity of the copper wheel, the molten charge solidified at high rate. Then an amorphous ribbon was formed. The casting was performed in an argon atmosphere in a vacuum chamber and the prepared amorphous ribbon is about 30 μm in thickness and 3mm in width.

Subsequently, the amorphous ribbon was crystallized by sealing them in evacuated silica tubes, placed in a preheated furnace at prescribed tempera-

tures and followed by quenching cooling in water to room temperature. Three different samples, which were heated at 500°C, 550°C and 610°C, resp., for one hour have been prepared and investigated in this work.

Important temperature for crystallization

The magnetic moment of the alloys as a function of temperature was measured by a Lakeshore vibrating sample magnetometer equipped with a high temperature furnace. The amorphous ribbon $(Fe_{0.5}Co_{0.5})_{80}Nb_4B_{13}Ge_2Cu_1$ was heated from 80°C to 800°C at 2°C/min heating rate in a 5 kOe applied magnetic static field. Figure 3.6 presents results of the thermo-magnetic measurements. The gradual decrease in magnetization from the initial state reflects the approach of the amorphous phase to its Curie temperature. It can be seen that the Curie temperature of the amorphous phase is rather low. This is due to the alloying with the glass forming element as well as the distributed exchange interaction which alter the temperature dependence of the magnetization. Then again an increase of the magnetic moment beginning at 410°C will be obtained as a consequence of the primary crystallization process where bcc FeCo is formed. The evidence for secondary crystallization is observed at around 740°C, where is again a small increase in magnetization. From the thermo-magnetic measurements, we could see that the three $(Fe_{0.5}Co_{0.5})_{80}Nb_4B_{13}Ge_2Cu_1$ alloy samples heated at 500°C, 550°C and 610°C, resp., are located between the temperatures for primary and secondary crystallization.

3.2 TEM plan-view imaging and electron diffraction analysis

The microstructure and morphology of the alloys heated at various temperatures were investigated by different TEM techniques, including conventional plan-view bright-field (BF) and dark-field (DF) imaging, electron diffraction (ED), high resolution transmission electron microscopy (HRTEM) as well as scanning transmission electron microscopy using the high angle annular dark

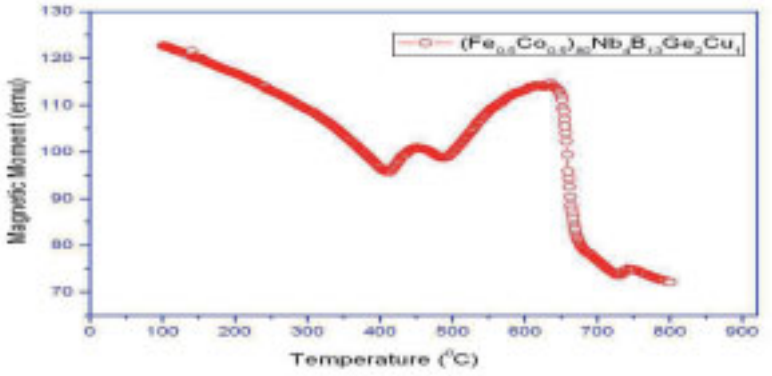

Figure 3.6. Magnetization versus temperature of the alloy $(Fe_{0.5}Co_{0.5})_{80}Nb_4B_{13}Ge_2Cu_1$.

field imaging technique (STEM-HAADF). All of these TEM investigations were performed on a JEOL 2200FS FEG transmission electron microscope. The objective lens was strongly excited. Thus the samples were magnetized along the optical axis and only structural contrast could be visualized. The spherical aberration of the objective lens is $C_s = 0.5$ mm and then providing a point-to-point resolution of 0.19 nm. A Gatan 794 slow-scan CCD camera with 1024×1024 pixels was used for recording the TEM images. A JEOL high-angle annular dark-field detector was installed above the Ω energy filter for recording the STEM-HAADF images.

Standard TEM plan-view samples were prepared by ion milling. The annealed amorphous ribbon sample was first cut into a circular disk with 3 mm diameter. Before these small disk specimens were placed on copper grid, they were manually mechanical grinded to remove the possible surface oxidation layer formed during annealing. A Gatan Precision Ion Polishing System Model 691 (PIPS) was used to polish the specimens. Typically, the procedure was carried out at 4.5kV accelerating voltage with a tilt angle of 10°. The procedure was applied for 30-40 minutes, then the final process was done at a lower voltage of 2.8-3 kV with a tilt angle 5° (10-20 minutes).

3.2.1 500°C sample

Figure 3.7 shows the TEM plan-view BF image and the corresponding electron diffraction patterns (SAED and NBD) of the sample heated at 500°C for one hour. The BF image was taken from a thin area close to the edge of a big hole in the sample. This hole was formed during the sample preparation. It is also used as the reference vacuum area in the electron holography experiments. As for a standard ion milling sample, the thickness is increased from the edge of the hole to the central area and only the thin area close to the edge is suitable for TEM observation. The BF image shows that very small grains with dark contrast are embedded in the matrix. The range of the grain size is from 4 nm to 20 nm. The average grain size was measured about 12 nm from higher magnification images.

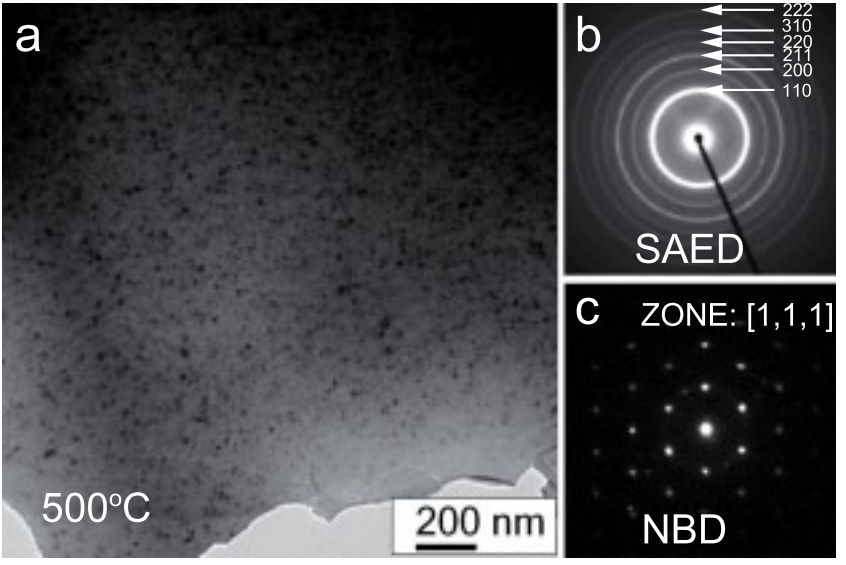

Figure 3.7. $(Fe_{0.5}Co_{0.5})_{80}Nb_4B_{13}Ge_2Cu_1$ alloys heated at 500°C for one hour: (a) bright field image; (b) corresponding SAED pattern from large area and (c) NBD pattern from a single grain.

The microstructure of the alloys was investigated by electron diffraction. The recorded intensity represents the Fourier transform of the electron exit wave. Thus, the electron diffraction directly reflects the structure informa-

tion of the materials in reciprocal space. Two different diffraction modes, the selected area electron diffraction (SAED) and the nano-beam diffraction (NBD) were applied to the investigations.

In SAED diffraction mode, the contributed electrons are coming from a large area which is limited by the selected area aperture (SAA). The SAA is located at the image plane of the objective lens. With the different aperture sizes, the selected area could be varied from 100 nanometers to several micrometers. A typical SAED pattern taken from the sample heated at 500°C for one hour is shown in Fig. 3.7b. The continues diffraction rings indicate that the sample is polycrystalline and the grains have a complete random orientation. The width of the rings is bordered due to the small size effect, since the diffractions were coming from the small crystalline grains.

Furthermore, by measuring the distance L between the diffraction rings and the central spot (transmitted beam), according to the geometrical relationship

$$R \cdot d = L \cdot \lambda, \tag{3.1}$$

where R is the camera length (in this work R=80 cm), d is the lattice plane distance and λ is the electron wavelength ($\lambda = 0.025$ Å for 200 keV electrons), the diffraction pattern can be interpreted as α-FeCo phase with bcc structure, and the lattice constant is a=2.85Å. The indices of the diffraction planes have been marked on the SAED pattern. From inside to outside, the diffraction rings are corresponding to (110), (200), (211), (220), (310) and (222) planes, subsequently. The α-FeCo structure model is illustrated in Fig. 3.8, the main lattice plane distances are listed at the right-hand side for comparison.

It should also be noticed that a wide halo ring is overlapped on the (110) ring. This halo ring is coming from the diffraction of the amorphous phase. It indicates that the sample was not fully crystallized and there is still a large residual amorphous phase inside the alloy.

Though useful structure informations have been obtained from SAED pattern, the conventional SAED technique still has some limitations. One of the limitations is that it can not be used to identify the microstructure of a single grain. This is due to the fact that the smallest area selected by the

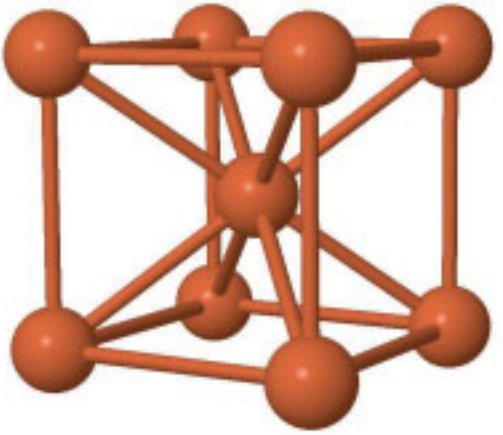

h k l	d (Å)
1 1 0	2.02
2 0 0	1.43
2 1 1	1.16
2 2 0	1.01
3 1 0	0.90
2 2 2	0.82
3 2 1	0.76
4 0 0	0.71
3 3 0	0.67
4 1 1	0.67
4 2 0	0.64

Figure 3.8. BCC structure of α-FeCo phase. Part of the lattice plane distances are listed on the right-hand side.

SAA is about 100 nm, which is much larger than the size of a single grain. This limitation can not be solved by using a smaller aperture. This is not only due to the difficulties of fabricating smaller mechanical apertures (In JEOL 2200FS, the smallest aperture size is 10 μm), but more due to the fact that the SAA is actually located at the image plane of the objective lens. Then, comparing with the physical size of SAA, the selected area is demagnified by the objective lens. The objective lens is not perfect and has a spherical aberration. Thus, even using smaller apertures, the electrons contributed to the diffraction pattern will not be the same observed and selected by the aperture in the imaging mode [40].

In order to overcome this problem, a novel nano-beam diffraction (NBD) was used to obtain the electron diffraction from a single grain. Instead of using SAA, an nearly parallel nano-sized beam was directly illuminated on the sample. The beam was generated with a spot size of 0.7 nm and a condenser lens aperture (CLA) 4 (10 μm in diameter) in NBD mode. After carefully moving the sample, an NBD pattern from a single grain was observed and recorded as shown in Fig. 3.7c. The NBD pattern looks like a conventional single crystal electron diffraction pattern. It could be indexed as α-FeCo

(bcc structure) with [1 1 1] zone axis orientation. Both of SAED and NBD indicate that the alloys are formed with small randomly oriented single crystalline FeCo particles which are embedded in an amorphous matrix.

The structure of the alloys was further investigated by means of DF images. This kind of diffraction contrast images were formed with the particular diffracted beam which have been selected by an aperture located at the back focal pane of the objective lens. In JEOL-2200FS with UHR resolution, a high contrast aperture (HCA) below the lower pole piece was installed instead of the normal in-gap aperture due to the small distance of the pole pieces.

First, the microscope was switched to SAED diffraction mode, then part of the (110) or (200) diffraction ring was selected by HCA 4 (5 μm in diameter), the aperture positions are indicated on the SAED pattern in Fig. 3.9. In order to get a high quality DF image, the selected diffracted beams were aligned along the optical axis by tilting the incident beam. When the microscope was switched to the imaging mode, the DF images were formed. The DF images at the center and at the right of Fig. 3.9 are corresponding to the HCA positions 1 and 2, respectively. Both of the two images were taken from the same area according to the BF image in Fig. 3.7a. Since only selected diffracted electrons have contributed to the dark-field image, the vacuum and the matrix show now a dark contrast, whereas the FeCo crystallites with bright contrast are clearly separated from the matrix and the other grains which were not oriented to the same diffraction conditions. The DF images further proved that the nano-grains have the FeCo bcc structure.

3.2.2 550°C and 610°C sample

Figure 3.10a and Fig. 3.11 show the BF and DF images of the sample heated at 550°C for one hour, respectively. It could be seen that though the heating temperature is increased, the morphology of the alloys did not change too much. Again the small grains with dark contrast were embedded in the matrix. The average grain size is only slightly increased from about

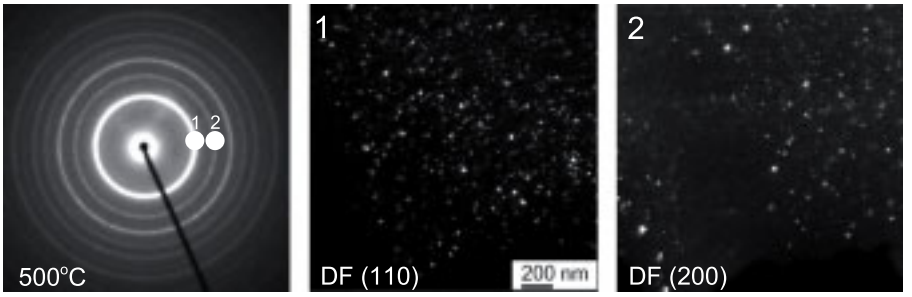

Figure 3.9. Dark-field images of $(Fe_{0.5}Co_{0.5})_{80}Nb_4B_{13}Ge_2Cu_1$ alloys heated at 500°C for one hour. The corresponding HCA positions are marked on the SAED pattern.

12 nm to about 18 nm. The SAED pattern in Fig. 3.10 shows the similar polycrystalline microstructure as for the 500°C sample, where small randomly oriented FeCo grains are embedded in an amorphous matrix. The amorphous phase could be recognized from the halo ring superimposed to the (110) ring in the SAED pattern. Again, the NBD pattern in Fig. 3.10c from a single grain proves that the grains are crystallized in the α-FeCo phase.

However, when the heating temperature was increased to 610°C for one hour, the grain sizes are dramatically increased to about 90 nm, as shown in the BF image of Fig. 3.10d. The grains are very closely clustered to each other. This indicates that the residual amorphous phase is very little. This was also proved by the SAED pattern as shown in Fig. 3.10e. The halo ring from the diffraction of the amorphous phase disappeared. For this heating temperature, the polycrystalline diffraction rings are not continually closed due to the larger grain size.

Though most of the polycrystalline diffraction rings corespond to the α-FeCo phase, it should be noted that several diffraction spots are located nearby the primary beam inside of the (110) ring, as marked by an arrow in Fig. 3.10e. These diffraction spots are corresponding to the fcc $(FeCoNb)_{23}B_6$ phase which has large lattice parameters (a=10.9 Å). This phase indicates that the secondary crystallization has already taken place at the heating temperature of 610°C.

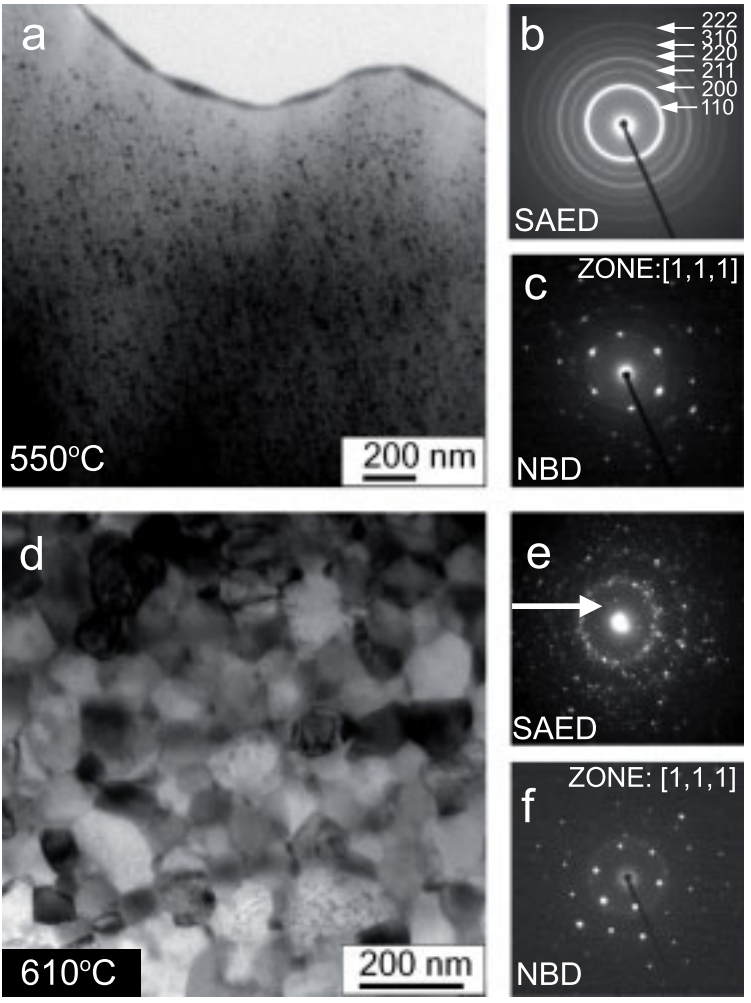

Figure 3.10. Morphology and structure of $(Fe_{0.5}Co_{0.5})_{80}Nb_4B_{13}Ge_2Cu_1$ alloys: (a-c) heated at 550°C for one hour and (d-f) heated at 610°C for one hour.

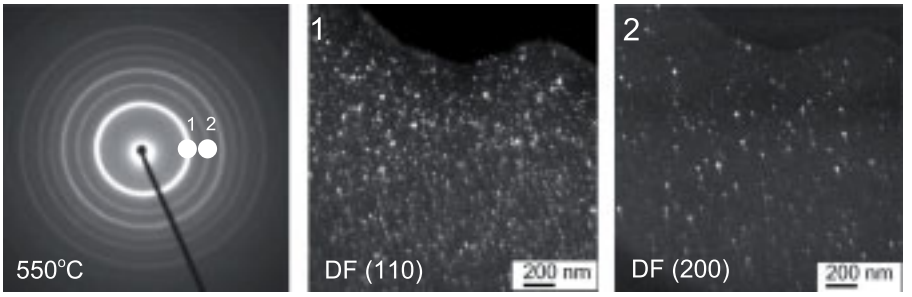

Figure 3.11. Dark field images of $(Fe_{0.5}Co_{0.5})_{80}Nb_4B_{13}Ge_2Cu_1$ alloys heated at 550°C for one hour. The corresponding HCA positions are marked in the SAED pattern.

3.3 HRTEM investigation

The microstructure of the alloy samples was further investigated by HRTEM. Different from the BF and DF imaging technique, HRTEM uses a so-called multi-beam (transmitted beam and diffracted beams) to form an interference fringe image. Since higher spatial frequencies represented by higher order diffraction are included, HRTEM can achieve the ultimate lateral resolution and directly indicate the atomic or crystal lattice plane arrangements in the materials investigated.

3.3.1 HRTEM image of 500°C sample

Figure 3.12 shows the HRTEM image of the sample heated at 500°C for one hour. The image size is 32 nm ×32 nm. From the HRTEM image, the two-phase microstructure of the nanocrystalline phase with fringe contrast and of the amorphous phase with maze contrast is clearly distinguished. The nanocrystalline grains are embedded in the amorphous matrix. One of the grains which is very close to the top of the image clearly shows two-dimensional lattice fringes contrast. The two sets of the lattice fringes are perpendicular to each other, and both of the fringe spacings were measured as 2.0 Å, which corresponds to the (110) plane of the α-FeCo phase. The Fourier transform spectrum of this grain is inserted at the top right of the

image compared with the simulated SAED pattern in Fig. 3.13. We can recognize that this grain is imaged close to the [0 0 1] zone axis. The size of the grain is about 7.3 nm, and the distances to the neighbor grains are about 6.5 nm, 8.1nm and 10.9 nm, respectively. There is a clear boundary between the grain and the residual amorphous matrix.

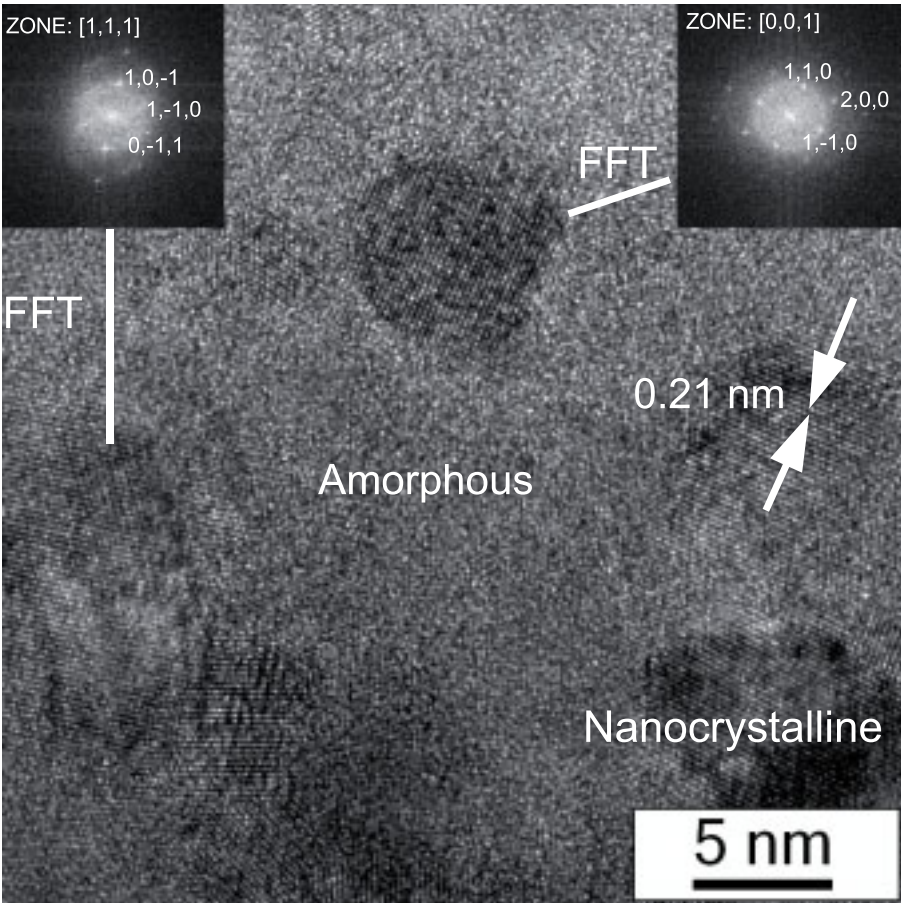

Figure 3.12. HRTEM image of $(Fe_{0.5}Co_{0.5})_{80}Nb_4B_{13}Ge_2Cu_1$ alloy heated one hour at 500°C.

Another grain, which shows a hexagonal arrangement of columns is located close to the right-hand side of the image. By comparing the Fourier transform spectrum inserted at the top left of the image and the simulated

SAED pattern in Fig. 3.13b, we could find that the orientation of this grain is close to the [1 1 1] zone axis, which is different from the orientation of the grain described previously. Several other grains only show one-dimensional structure image due to the non-zone axis orientation. However all of the fringe spacings are measured as 2.0 Å, which belongs to the (110) plane of α-FeCo phase. The atomic arrangement in the HRTEM image further proved that the FeCo grains with random orientation are embedded in the amorphous matrix.

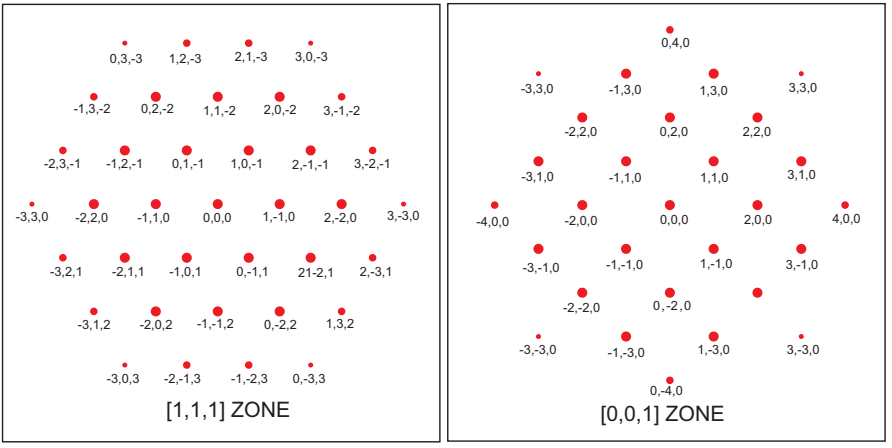

Figure 3.13. Simulated SAED pattern of FeCo alloy: (a) [1 1 1] zone axis; (b) [1 0 0] zone axis.

3.3.2 HRTEM images of 550°C and 610°C sample, respectively

The HRTEM images of the samples heated one hour at 550°C and 610°C respect., are compared in Fig. 3.14. The sample annealed at 550°C exhibits again small nanocrystalline grains with lattice fringe contrast. The nanocrystalline grains are surrounded by an amorphous phase with maze contrast (Fig. 3.14a). The grains have different orientations. But both of the lattice plane distances are measured to be around 2.0 Å, which corresponds to the (110) plane of α-FeCo phase and is consisting with electron diffraction results.

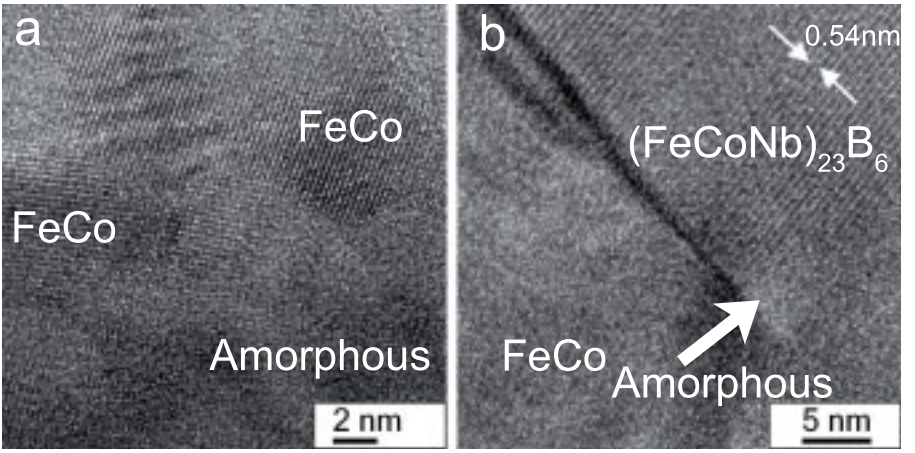

Figure 3.14. HRTEM image of $(Fe_{0.5}Co_{0.5})_{80}Nb_4B_{13}Ge_2Cu_1$ alloy: (a) 550°C and (b) 610°C sample.

Figure 3.14b shows the HRTEM image of the sample heated one hour at 610°C. The grain sizes are much larger then those of the 550°C sample. Only a small part of the amorphous phase could be found among the boundaries of the grains. This indicates that most of the residual amorphous phase has been crystallized. Additionally, the grain boundary is very straight. The fringe spacings d=2.0 Å again give evidence that the grain (bottom left) belongs to the α-FeCo phase.

The grain (top right of Fig. 3.14b) shows a different structure, where the fringe spacing was measured to 5.4 Å. Compared with the d-spacings of α-FeCo phase listed in Fig. 3.8, the largest fringe spacing which could be shown in a HRTEM image is d_{110}= 2.0 Å (the diffraction from the (100) plane with the spacing 2.85 Å is conventionally forbidden in bcc structure). It indicates that the grain at the upper right of the image is not crystallizing in the α-FeCo phase, but belongs to the fcc $FeCoNb_{23}B_6$ phase which has a much larger lattice constant (a=10.9 Å). $FeCoNb_{23}B_6$ is formed during the secondary crystallization. The d-spacing for (002) plane is 5.45 Å, which is close to the fringe spacing measured in Fig. 3.14b.

The $FeCoNb_{23}B_6$ phase is a derivation of the $Fe_{23}B_6$ phase, which adopts the $Cr_{23}C_6$ prototype structure with space group $Fm\bar{3}m$ and Pearson symbol

cF116. The $Fe_{23}B_6$ phase is a metastable phase and can easily decompose into Fe_3B and $\alpha-Fe$ in the Fe-B alloy system. However, when the Fe atom site is partially substituted by another transition metal atom such as Nb, Co, or Ni, the phase is stabilized and can easily be retained. The structure view is presented in Fig. 3.15.

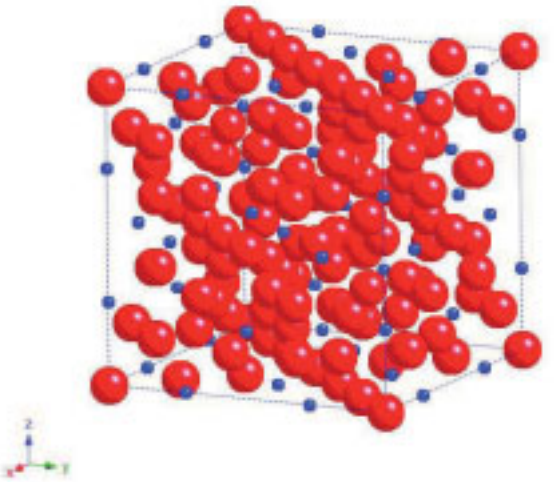

Figure 3.15. Structure model of the $Fe_{23}B_6$ phase.

The existence of the $FeCoNb_{23}B_6$ phase at higher heating temperature (at 820°C for one hour) samples have been proved by X-ray diffraction (XRD) and three-dimensional atom probe (3DAP) analysis [49]. From the HRTEM analysis and the SAED analysis in Fig. 3.10c, we directly observed that a few crystallites of the $FeCoNb_{23}B_6$ phase have been formed at 610°C, which is much lower than the secondary crystallization temperature (740°C) measured by thermo-magnetic measurements.

3.3.3 Moiré patterns

Besides the normal lattice fringes, sets of coarse fringes which are called moiré fringes were also observed in samples annealed at 500°C and 550°C,

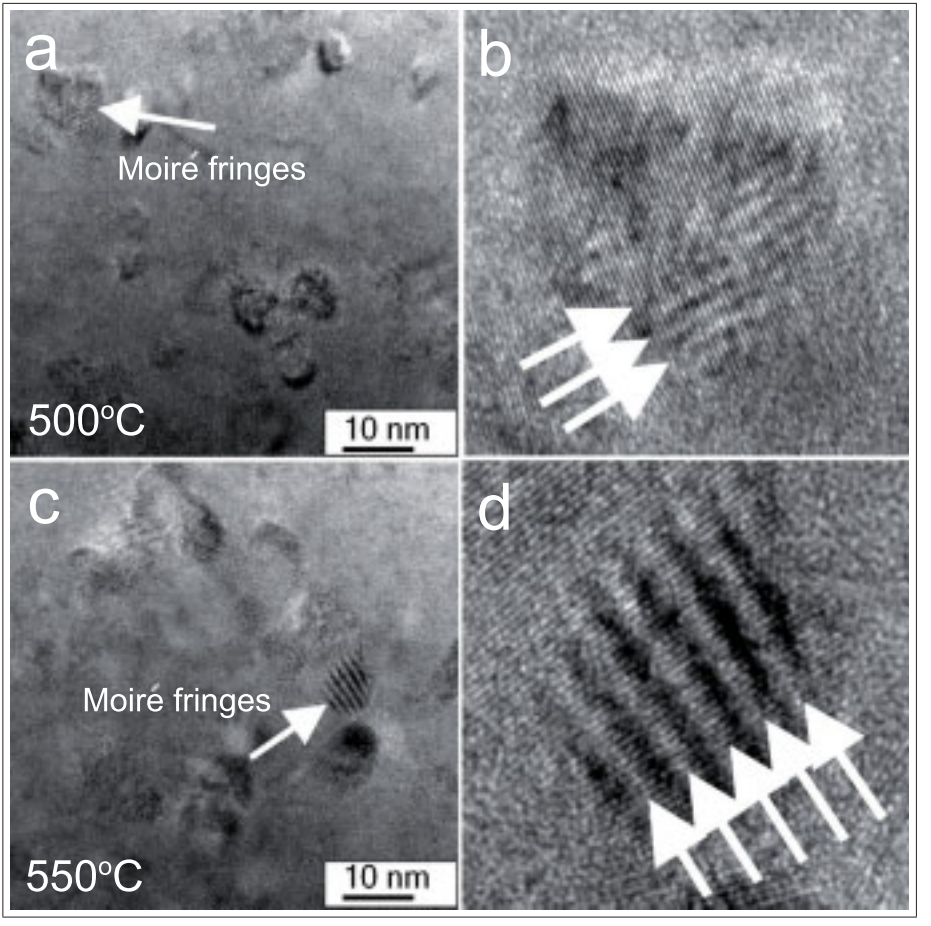

Figure 3.16. Moiré fringes in $(Fe_{0.5}Co_{0.5})_{80}Nb_4B_{13}Ge_2Cu_1$ alloys. (a) and (b): HRTEM image of 550°C sample and enlarged moiré fringe image; (c) and (d): HRTEM image of 550°C sample and enlarged image.

respectively. From the HRTEM images with large field of view, as shown in Fig. 3.16a and c, the moiré fringes which are marked by the white arrows could be easily recognized. The corresponding enlarged images are presented in Fig. 3.16b and d. The moiré fringe spacings in Fig. 3.16b and d were measured as d_m=6.2 Å and d_m=11.6 Å, respectively. Both of them are much larger than the conventional lattice fringe spacings d_{110}=2.0 Å, which are also visible in the enlarged images. The formation mechanism of moiré fringes is illustrated in Fig. 3.16.

If two grains are overlapping each other along the electron beam direction, then the beam is transmitting both of the grains subsequently. Under proper condition, which means that the lattice planes in both of these two grains are satisfying the Bragg diffraction condition, then two sets of diffraction fringes will be formed. If there is a relative in-plane rotation between them as shown in Fig. 3.16, the moiré fringes will be formed as a consequence of the rotation.

If the $\vec{g}$ vector of the top and bottom lattice planes are $\vec{g_1}$ and $\vec{g_2}$, resp., then the $\vec{g}_m$ vector for moiré fringes is given by

$$\vec{g_m} = \vec{g_1} - \vec{g_2} \tag{3.2}$$

In our example yields, $g_1 = g_2 = 1/d_{110}$, and $g_m = 1/d_m$, so the rotation angle θ could be calculated as

$$\theta = 2 \arctan\left(d/2d_m\right) \tag{3.3}$$

From Eq. 3.3 the rotation angles in Fig. 3.16a and b can be determined as 18.3° and 9.9°, respectively. The moiré fringes provide the information that the grains located in different depths perpendicular to the ribbon plane also have different orientations.

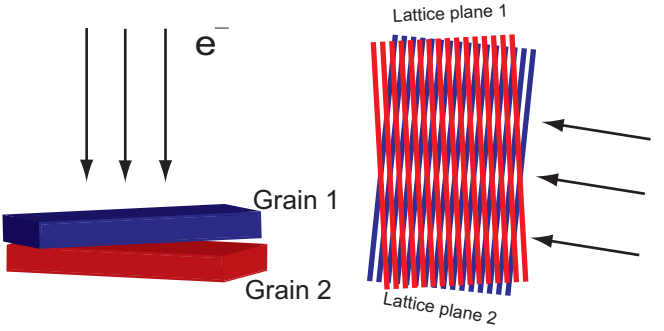

Figure 3.17. Illustration of the formation of moiré fringes.

3.4 STEM-HAADF imaging

Conventional TEM techniques such as BF- or DF-TEM use the transmitted undiffracted beam or one of the diffracted beams for imaging. Whereas in HRTEM the interference pattern of the undiffracted and many diffracted beams is observed. Contrary to that, high angle incoherent electrons are used in STEM-HAADF. The electrons are recorded by a high-angle annular dark-field electron detector, and the whole system is working in the scanning mode. Then in STEM-HAADF, transmitted electrons, Bragg diffracted electrons and inelastically scattered electrons which are mostly concentrated at low scattering angles are all excluded. The scattering cross-section could be obtained by integrating the Rutherford scattering cross-section from the inner angle to the outer angle with respect to the detector. Then the signal intensity in STEM-HAADF is proportional to the power of the atomic number, Z. This technique is therefore also called Z-contrast imaging technique. Thus, STEM-HAADF can not only provide the structure information, but also the information of the chemical composition of the materials to be investigated [31].

The STEM-HAADF images of $(Fe_{0.5}Co_{0.5})_{80}Nb_4B_{13}Ge_2Cu_1$ alloys heated at different temperatures are presented in Fig. 3.18. The images were recorded with a spot size of 1.5 nm and a camera length of 60 cm. Figure 3.18a shows the STEM-HAADF image of the sample heated for one hour at 500°C. We can see that small grains with bright contrast are distributed

in the dark contrast matrix. This contrast behavior is similar to the conventional DF image given in Fig. 3.9. However, here the contrast could be explained in a more straight way. The strong signal intensity in the grains is due to the high concentration of the relative heavy elements Fe and Co, while the residual matrix consists of the light element B. STEM-HAADF image contains about information of both the structure and chemical composition information in the alloys.

The STEM-HAADF images of the samples heated at 550°C and 610°C are shown in Fig. 3.18b and c, respectively. The size of the grains is only slightly increased to about 20 nm for the sample heated at 550°C, while in the size for the sample heated at 610°C is much larger (about 90 nm).

3.5 EDX spectrum analysis

In addition, the chemical composition of the alloys was investigated by energy dispersive X-ray spectroscopy (EDXS). The spectra were required from STEM-HAADF images. When high energy electrons transmit through the material, the inner electrons of the atoms will be excited to high energy level and leave a hole. Subsequently the hole will be filled again by a high energy level electron which occupies the low energy level. During the transition, a characteristic X-ray will be emitted. Since the emitted X-ray is characteristic for each element, EDXS can be used to identify the elements.

The EDX spectra of the sample heated one hour at 500°C are shown in Fig. 3.19. The spectra were taken in the HAADF-STEM point analysis mode with beam spot size 1.5 nm. Two different spectra, from the area outside and inside of a grain were recorded, respectively. The positions have been marked on the STEM-HAADF image in Fig. 3.19. The EDX spectrum a, which was taken outside of the grain, indicates the existence of Fe, Co, Nb, Ge and Cu elements. The light element B could not be detected because of the limitations of the EDX detector. For quantification, the atom ratio between Fe and Co has been calculated to Fe:Co=0.92. Considering the accuracy of the EDX method, this is close to the nominal ratio 1:1 in the predecessor.

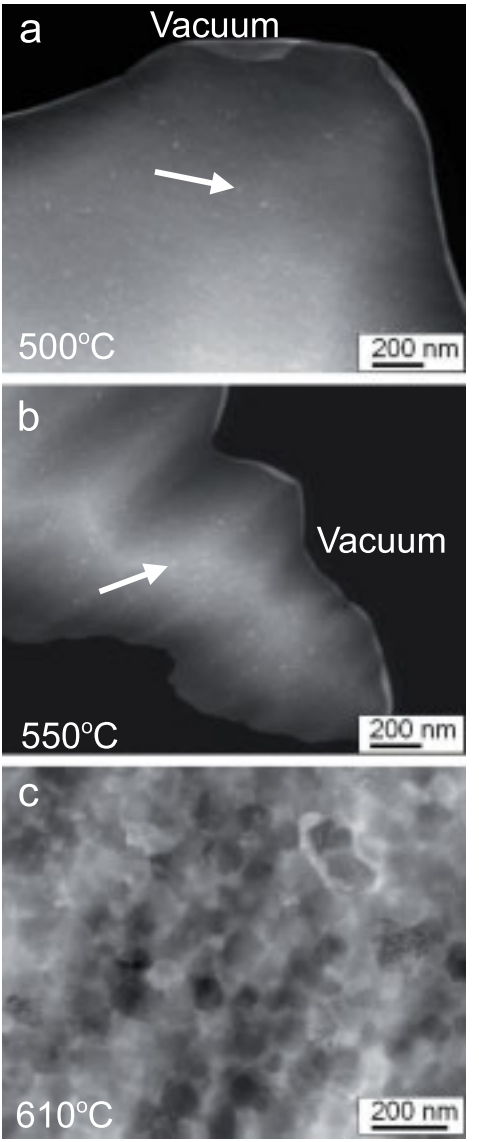

Figure 3.18. STEM-HAADF images of $(Fe_{0.5}Co_{0.5})_{80}Nb_4B_{13}Ge_2Cu_1$ alloy: (a) 500°C sample, (b) 550°C sample and (c) 610°C sample.

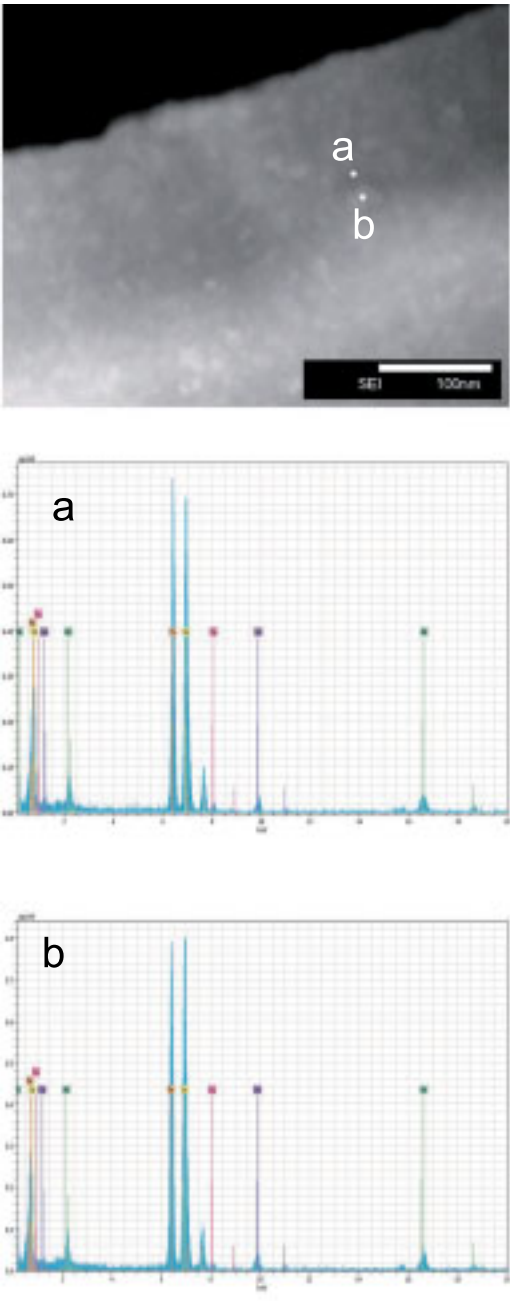

Figure 3.19. EDX spectrum of $(Fe_{0.5}Co_{0.5})_{80}Nb_4B_{13}Ge_2Cu_1$ alloy heated for one hour at 500°C: (a) spectrum outside of the grain; (b) spectrum inside the grain.

From the EDX spectrum b, which was taken from the area inside of the grain, the atom ratio between Fe and Co was again determined as Fe:Co=0.92. However the signal from the elements Nb, Ge and Cu also can be found in the spectrum. This can be arise, while the grain is actually surrounded by the amorphous phase. Then the beam transmitted both the grain and the amorphous area. Therefore we can not distinguish the composition difference from the EDX spectrum. A more detailed investigation of the alloys composition was performed by 3D atom probe analysis (3DAP) described elsewhere.

3.6 Summary

In this chapter, we have described the investigation of microstructure and chemical composition of the FeCo-based nanocrystalline softmagnetic alloys by combining different analytical TEM techniques. Besides the conventional BF- and DF-TEM, electron diffraction (SAED and NBD), HRTEM, HAADF-STEM as well as EDX analysis were applied. The obtained results already show that the alloys formed consist of small randomly orientated α-FeCo nano particles which are embedded in an amorphous matrix. The size of the crystalline grains is strongly depending on the crystallization temperature. The average grain size is about 12 nm and 18 nm when the samples are heated one hour at 500°C and 550°C, respectively. However when the heating temperature was increased to 610°C, the average grain size is drastically increased to about 90 nm. This is a hint for low softmagnetic properties. The so-called secondary crystallization phase $FeCoNb_{23}B_6$ was also present in the alloys heated at this temperature. The results discussed in chapter 3 will be correlated with the investigations of the magnetic domain structure by Lorentz microscopy and electron holography in chapter 4.

Chapter 4

Magnetic domain structure of FeCo-based alloys

In this chapter, we will discuss the investigation of magnetic domain structure of FeCo-based nanocrystalline soft magnetic alloys by Lorentz microscopy and electron holography. First, we will give a brief introduction to the formation of magnetic contrast using electron holography. Then the magnetic domain configurations of the FeCo-based nanocrystalline soft magnetic alloys heated at different temperatures (500°C, 550°C and 610°C for one hour) will be compared. The domain wall width has been quantitatively measured and compared with numerical simulations. The magnetic flux density of the alloys was also determined from the reconstructed phase image of the electron hologram. The sample thickness necessary for the determination of the flux density was measured by the log-ratio method of electron energy loss spectroscopy (EELS). Furthermore, by tilting the samples in a weakly excited objective lens field, the dynamical magnetization process was observed in both the Lorentz microscopy and the electron holography mode. Finally the correlation between the microstructure and the magnetic domain structure of the alloys will be discussed.

4.1 Introduction

4.1.1 Magnetic domain structure and magnetic imaging

Bulk ferromagnetic material commonly consists of a magnetic domain structure. This means the magnetic moments of the individual atoms are aligned in each domain, but varies from domain to domain [50]. The intermediate area which separates the different domains is called magnetic domain wall. As pointed out by Landau and Lifshitz, the formation of domain structure is a result of the minimization of the total energy in ferromagnetic materials,

$$E = E_{ex} + E_k + E_\lambda + E_D + E_H, \tag{4.1}$$

where E_{ex} is the exchange energy, E_k is the magnetocrystalline anisotropy, E_λ is the magnetoelastic energy and magnetostriction energy, E_D is the magnetostatic energy and E_H is the Zeeman energy in the presence of an applied field [51].

Several different techniques have been developed for imaging magnetic structures (including magnetic domain structures), such as the measurement of the magneto-optical Kerr effect (MOKE), magnetic force microscopy (MFM), spin-polarized scanning tunneling microscopy (SP-STM) and scanning electron microscopy with polarization analysis (SEMPA) [52]. Compared with these techniques, Lorentz microscopy and electron holography, which are carried out in TEM enable us not only to imaging the magnetic structure with high resolution (down to nanometer scale) and high sensitivity (1×10^{-16} wb), but could also be combined with conventional TEM analytical techniques to study the correlations between microstructure and magnetic structure. In addition, Lorentz microscopy and electron holography can be extended to study the dynamic magnetic behaviors by using special sample stages like an in-situ heating or cooling sample stage. Furthermore, the magnetic field excited by the objective lens itself can be used as an applied field to study the in situ magnetization behavior without any additional equipment.

Conventional scanning probe microscopy (SPM) techniques (MFM or SP-STM) detect the magnetic stray field around the surface of the sample. Comparing to these techniques, high energy electrons in TEM are transmitting the whole sample and carry the bulk information of the magnetization. Though today most of the electron holography techniques can record only the integrated information along the electron path, it can be expected that by using electron holographic tomography, the three-dimensional distribution of magnetization can be obtained in near future.

4.1.2 Magnetic contrast formation in electron holography

The formation of magnetic contrast in electron holography is caused by electron scattering due to the magnetic vector potential. Figure 4.1 shows the hologram and the reconstructed phase image of the nanocrystalline soft magnetic alloy $(Fe_{0.5}Co_{0.5})_{80}Nb_4B_{13}Ge_2Cu_1$ heated one hour at 500°C. The image was taken in Lorentz mode when the main objective lens was switched off. As shown in the electron hologram, both the sample and the vacuum area are covered by interference fringes. An enlarged part of the hologram is inserted at the upper right of the hologram. It indicates that the fringes which are connected with the phase shift of the electrons are strongly distorted across the sample. The phase shift can be recognized more easily from the Fourier transform spectrum of the hologram. The side bands are strongly dispersed due to the magnetic field.

The reconstructed amplitude image from the electron hologram looks like a conventional BF-TEM image, no special magnetic contrast can be seen. However, the reconstructed phase image shows a distinct feature, that large contour lines are distributed in and around the sample. The spacing between the two adjacent contour lines corresponds to an electron phase shift of 2π. The contour lines in the vacuum area indicate the stray field, which can not be visualized in the amplitude image. The interpretation of the phase image is given below.

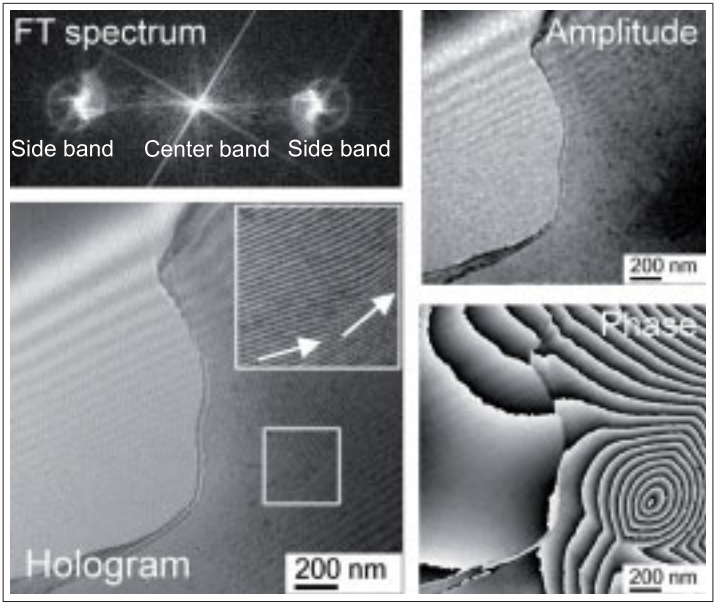

Figure 4.1. Electron hologram, reconstructed amplitude and phase images of $(Fe_{0.5}Co_{0.5})_{80}Nb_4B_{13}Ge_2Cu_1$ alloys heated one hour at 500°C.

Electron phase shift due to electrostatic potential and vector potential

When electrons transmit a thin magnetic film, they will be scattered by the electrostatic potential V and the magnetic vector potential $\vec{A}$. The Schrödinger equation is written as

$$[\frac{1}{2m}(-i\hbar\nabla + e\vec{A})^2 - eV]\psi = E\psi, \tag{4.2}$$

where m is the electron mass, $\hbar$ is the reduced Planck constant, e is the electron charge and E is the electron energy [53]. After solving the equation by using the WKB (Wentzel-Kramers-Brillouin) approximation, there is a phase difference ϕ between the electrons which take different paths l_1 and l_2,

$$\phi = \phi_{ele} + \phi_{mag} = C_E \int_{l_1-l_2} V ds - \frac{e}{\hbar}\int_{l_1-l_2} \vec{A}d\vec{s}, \tag{4.3}$$

where ϕ_{ele} and ϕ_{mag} are the electrostatic potential and the magnetic vector potential contributions, respectively [14, 15].

In the part of electrostatic potential contribution, C_E is an energy dependent interaction constant ($C_E = 0.00729$ (V nm)$^{-1}$ for 200 keV electrons), and V is the electrostatic potential distribution in three-dimensional space. Even without any external source, the electrostatic potential still exists in the samples. This inner electrostatic potential is generated by the positive charge of nuclei and negative charge of the electrons inside the atoms. It depends on the atomic arrangement and it is determined by the microstructure and chemical composition of the materials. A more detailed discussion of the inner potential will be given in chapter 5. In medium resolution, we only need to consider the average potentional contribution. Further, when the microstructure and the composition of the sample are homogenous, then V(x,y,z) can be written as $V(x, y, z) = V_0$, where V_0 is the material mean inner potential (MIP). For simplification we assume the sample thickness t is only varying in x direction (one-dimensional case). Then, as shown in Fig. 4.2b, when the electrons take different paths l_1 (through the sample with $V = V_0$) and l_2 (through the vacuum with V=0), according to Eq. 4.3 the phase difference due to electrostatic potential contribution $\phi_{ele}(x)$ is given by

$$\phi_{ele}(x) = C_E \int_{l_1} V_0 dz - C_E \int_{l_2} 0 \cdot dz = C_E V_0 t(x) \tag{4.4}$$

From Eq. 4.4 it can be seen that the phase shift of the electrons caused by the MIP contribution is connected with the sample thickness.

The phase shift caused by the magnetic vector potential contribution ϕ_{mag} is related with the Aharonov-Bohm effect [54]. As illustrated in Fig. 4.2a, two coherent electron beams are emitted from a point source and transmit the magnetic vector potential zone along different paths l_1 and l_2. According to Eq. 4.3, after they are arriving the same point, there is a phase difference between them,

$$\phi_{mag} = -\frac{e}{\hbar}\left(\int_{l1} \vec{A} d\vec{s} - \int_{l2} \vec{A} d\vec{s}\right) = -\frac{e}{\hbar} \oint \vec{A} d\vec{s}. \tag{4.5}$$

The magnetic vector potential $\vec{A}$ is defined as $\vec{B} = \nabla \times \vec{A}$, where B is the magnetic field.

There could be a particular situation that the magnetic field B is limited in a small region and electrons travel along two different paths l_1 and l_2 outside of this region. Then, the electrons can not feel any magnetic field. However, the integration $\vec{A}d\vec{s}$ in Eq. 4.5 indicates that there is still a phase difference between the electrons along the different paths, which is actually caused by the magnetic vector potential $\vec{A}$. This pure quantum phenomena is called Aharonov-Bohm effect (AB effect) and has been proved by various experiments [53, 54].

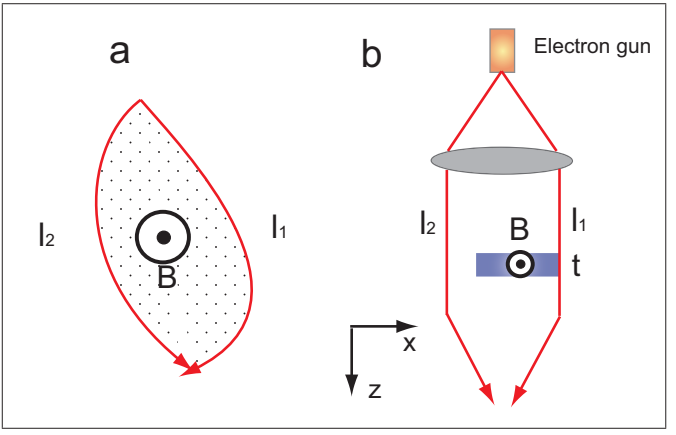

Figure 4.2. (a) Illustration of the Aharonov-Bohm effect. (b) Electron scattering by the electrostatic potential and the magnetic vector potential in TEM.

Similarly in TEM (see Fig. 4.2b), when electrons travel along the different paths l_1(the thin magnetic film) and path l_2 (the vacuum), the phase difference due to the magnetic vector potential is also described by Eq. 4.5. Then by using $\vec{B} = \nabla \times \vec{A}$, the integration in Eq. 4.5 can be transformed to

$$\oint \vec{A}d\vec{s} = \iint (\nabla \times \vec{A})d\vec{S} = \iint B_n dS, \tag{4.6}$$

where B_n is the component of the magnetic flux density perpendicular to the plane formed by the paths l_1 and l_2 (along y direction), as shown in Fig.

4.2b. Again we assume the magnetic flux B_n only varies along the x direction (one-dimensional case), Eq. 4.5 is rewritten as

$$\phi_{mag}(x) = -\frac{e}{\hbar}\iint B_n dS = \frac{e}{\hbar}\iint B_n(x)dxdz = \frac{e}{\hbar}\int B_n(x)t(x)dx. \quad (4.7)$$

By combination of Eq. 4.4 and Eq. 4.7, we will get

$$\phi(x) = \phi_{ele} + \phi_{mag} = C_E V_0 t(x) - \frac{e}{\hbar}\int B_n(x)t(x)dx. \quad (4.8)$$

From Eq. 4.8 it is obvious that the phase shift of the electrons is coming from both the MIP and the magnetic vector potential contributions. In general it is necessary to separate them before further investigation. Several methods can be applied for this purpose.

1. Recording the electron holograms at different accelerating voltages. According to Eq. 4.8, only the MIP contribution depends on the accelerating voltage through the interaction constant C_E. Then the magnetic potential contribution will be excluded in the difference of the two phase images which are recorded before and after changing the accelerating voltage. Afterwards the MIP contribution as well as the magnetic potential contribution will be calculated. However, the whole electro-optical system need to be readjusted after changing the accelerating voltage.

2. Turning over the sample. Obtaining two different holograms before and after turning over the sample. According to Eq. 4.8, the sign of the MIP contribution will keep the same, but the sign of the magnetic contribution will be changed. So by summing or by subtracting the two phase images, the two different potential contributions can be separated [55]. Alternatively, instead of a fully reverse, the sample can be tilted to $\pm\theta$ and fully magnetized in two opposite directions by the field of the objective lens [56]. Both of the two methods require a precise alignment of the two phase images. They are not suitable for samples of large magnetic films with strong stray field, as given in our investigation. Since the reference wave can be strongly distorted by the stray field.

3. Recording the electron holograms in both conventional TEM mode (focusing with objective lens) and Lorentz mode (objective lens off). As it has been mentioned, in CTEM mode, the magnetization of the sample will be aligned along the optical axis due to the objective lens field. Thus, only the mean inner potential contributions to the phase shift will be recorded. The difficulty is it is hard to get same field of view in CTEM mode as in Lorentz mode.

4. Preparing a sample with homogenous thickness. According to Eq. 4.8, the MIP contribution to the phase gradient will be zero. Then the magnetic potential contribution will be separated from the phase gradient. But this needs a special TEM sample preparation technique like the focused ion beam (FIB) technique.

The samples investigated in this thesis are wedge-shaped prepared by ion milling. No additional process was performed to remove the MIP contribution from the phase image. However, this will not cause a significant effect for imaging the magnetic flux distributions. This is due to the fact that the most important information connected with the magnetic flux distribution in magnetic samples is determined by the phase gradient, but not the phase itself. On the other hand, if the thickness variation is slow, then the mean inner potential contribution to the phase gradient is small and can be neglected. A quantitative analysis is given below. According to Eq. 4.8, the phase gradient is given by

$$\frac{d\phi(x)}{dx} = C_E V_0 \frac{dt(x)}{dx} - \frac{e}{\hbar} B_n(x) t(x). \tag{4.9}$$

As illustrated in Fig. 4.3 (one-dimensional case), we assume the thickness of the ion milling sample is linearly increased along the x direction, the magnetic flux direction is perpendicular to the xz plane and the magnetic flux density B_n is assumed to be constant. Then from the geometrical

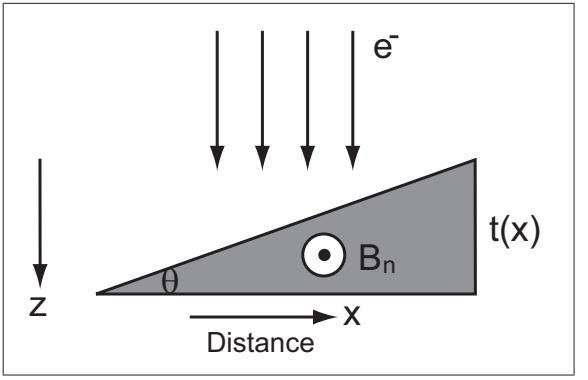

Figure 4.3. Sketch of wedge-shaped TEM sample prepared by ion milling.

relationship, the thickness t(x) is given by

$$t(x) = x \cdot \tan\theta, \tag{4.10}$$

where θ is the wedge angle. After inserting Eq. 4.10 into Eq. 4.8 and Eq. 4.9, we will get the total phase shift caused by both the electrostatic potential and the magnetic vector potential contributions,

$$\phi(x) = \phi_{ele} + \phi_{mag} = C_E V_0 \tan\theta \cdot x - \frac{e}{2\hbar} B_n \tan\theta \cdot x^2, \tag{4.11}$$

and the phase gradient is given by

$$\frac{d\phi(x)}{dx} = \frac{d\phi_{ele}}{x} + \frac{d\phi_{mag}}{dx} = C_E V_0 \tan\theta - \frac{e}{\hbar} B_n \tan\theta \cdot x. \tag{4.12}$$

From Eq. 4.12 it is obvious that the MIP contribution to the phase gradient is constant, while the magnetic contribution increases linearly with x.

For quantitative analysis, we assume the MIP of $(Fe_{0.5}Co_{0.5})_{80}Nb_4B_{13}Ge_2Cu_1$ alloy is 17.48 V (the average value of Fe (16.95 V) and Co (17.90 V)), the magnetic flux density B_n is 1.30 T (saturation flux density in bulk sample) and the sample wedge angle $\theta = 7.5°$. Then the MIP, the magnetic vector potential and the total potential contribution to the phase shift and to the

phase gradient are calculated and plotted in Fig. 4.4a and b, respectively.

$$\frac{d\phi(x)}{dx} = [1.68 \times 10^{-2} + 1.99 \times 10^{-3} t(x)](rad/nm) \tag{4.13}$$

The results indicate that in such wedge-shaped film sample with slow thickness variation, compared to the magnetic potential contribution, the mean inner potential contribution to both the phase and the phase gradient can be neglected . A similar result is also shown in Fig. 4.5, where the phase shift has been wrapped into 2π, corresponding to the raw phase image after the reconstruction.

4.2 Investigation of magnetic domain structure

4.2.1 Samples annealed at 500°C

Lorentz microscopy images and a reconstructed phase image of electron hologram of the alloys $(Fe_{0.5}Co_{0.5})_{80}Nb_4B_{13}Ge_2Cu_1$ heated one hour at 500°C are shown in Fig. 4.6. The Lorentz microscopy image under in-focus imaging condition is given in Fig. 4.6a. The image looks like a conventional BF-TEM image, no special magnetic contrast can be seen. However when the image condition was changed to a large defocus value, the image contrast was significantly changed. Figure 4.6b shows such a typical over-focused Lorentz microscopy image at the same area. Due to the reduced object distance, the image magnification is slightly increased and the Fresnel fringes can be seen near the edge of the sample. Besides these changes, the most distinct feature is the appearance of few black and white lines across the sample. As we have already explained, these bright or dark contrast lines were formed by the convergence or divergence of the deflected electrons due to Lorentz force. These contrast lines indicate the positions of the magnetic domain walls. Compared with the average size of the nanocrystalline grains of about 12 nm, the magnetic domains looks much larger and some of them are larger than one micrometer. On the other hand, the large domain sizes have re-

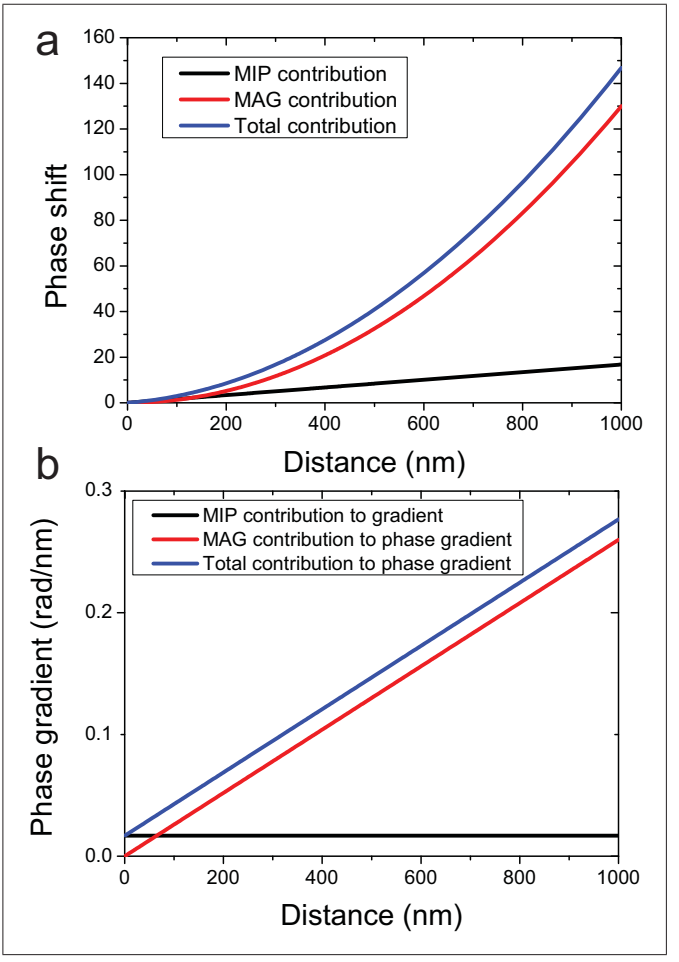

Figure 4.4. (a) Simulated electron phase shift and (b) phase gradient of a wedge-shaped $(Fe_{0.5}Co_{0.5})_{80}Nb_4B_{13}Ge_2Cu_1$ alloy sample.

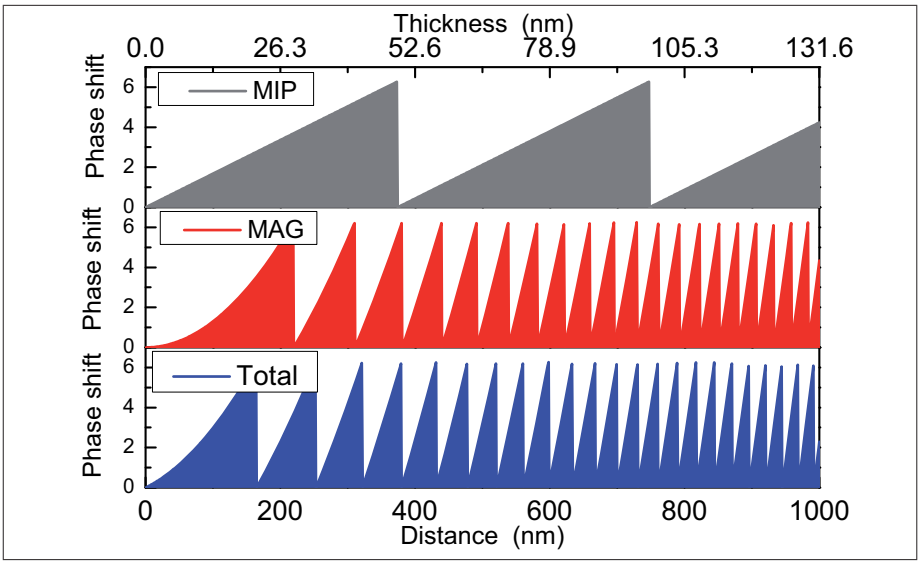

Figure 4.5. Simulated electron phase shift (wrapped with 2π) of a wedge-shaped $(Fe_{0.5}Co_{0.5})_{80}Nb_4B_{13}Ge_2Cu_1$ alloy sample.

duced the pinning sites which were marked by white arrows and hinting to good soft magnetic properties.

When the imaging condition was changed from over-focus to under-focus, the domain wall contrast was reversed, as shown in Fig. 4.6c. Unfortunately, in both the over-focused and the under-focused images, only the domain wall positions can be visualized. Therefore, electron holography investigations were further performed.

Before taking an electron hologram in the microscope, the imaging conditions were reset to in-focus. Additionally, a reference hologram taken in the vacuum area far away from the sample was used for the reconstruction. The reconstructed phase image is shown in Fig. 4.6d. Large phase contour lines can be directly seen from the raw phase image and indicate the magnetic flux distribution inside the sample. The phase difference between the two adjacent lines is 2π, corresponding to a magnetic flux of 4.1×10^{-15}wb. Compared with the Lorentz microscopy image in Fig. 4.6b, it can be seen that the magnetic flux change directions when they pass the domain walls

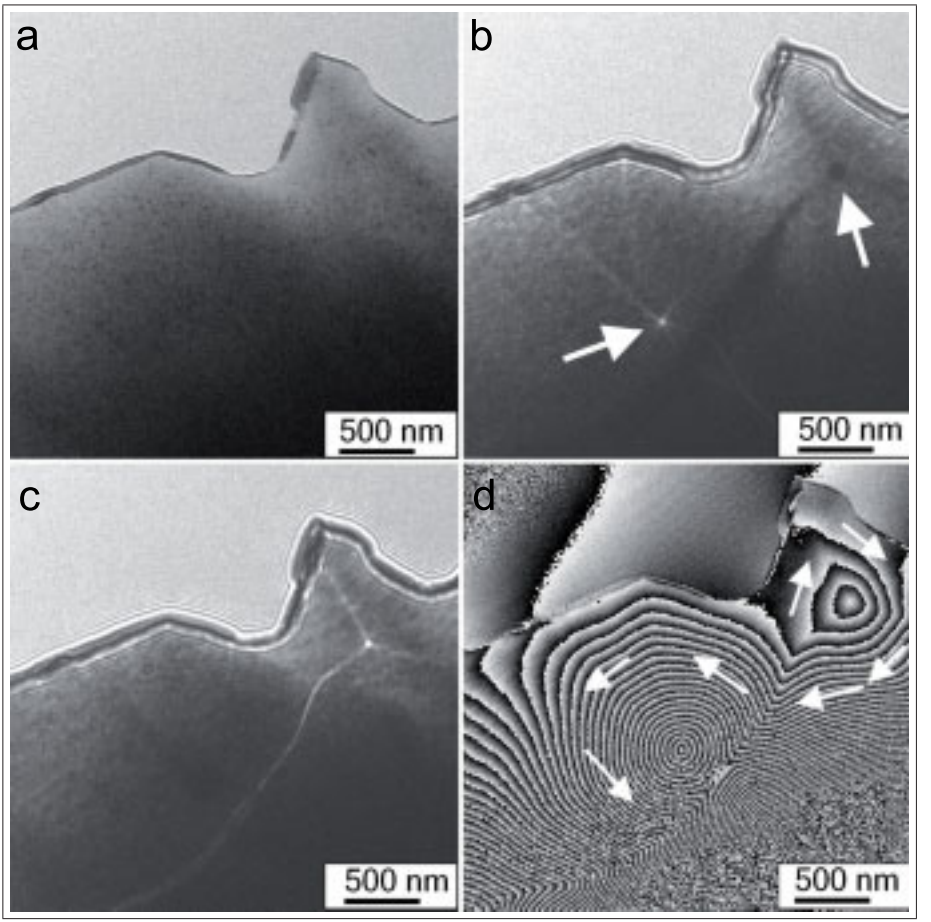

Figure 4.6. Magnetic domain structures of $(Fe_{0.5}Co_{0.5})_{80}Nb_4B_{13}Ge_2Cu_1$ alloy heated one hour at 500°C: (a) in-focus, (b) over-focused and (c) under-focused Lorentz microscopy images; (d) reconstructed phase image of the electron hologram within the same area. The magnetic flux directions are indicated by white arrows.

and form vortex structures. The vortex centers correspond to the cross points of the adjacent domain walls. The magnetic flux directions marked in the figure were determined by comparing with the Lorentz microscopy images. As illustrated in Fig. 4.7, the Lorentz force generated by the magnetic flux with counterclockwise rotation deflect the electrons to the center area and form bright contrast in the over-focused image, while the magnetic flux with clockwise rotation cause the inverse contrast. Both of the Lorentz microscopy images and the phase image show that the sample consists of large domains, hinting to good soft magnetic properties.

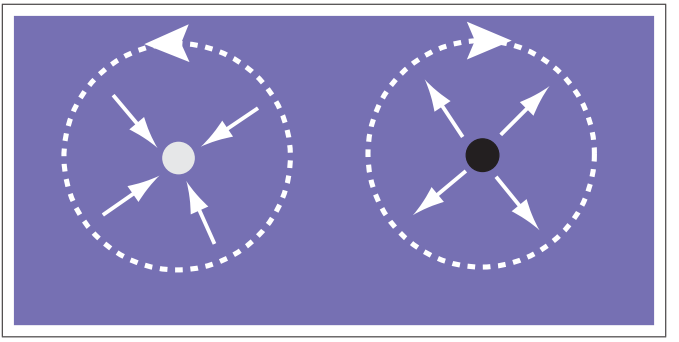

Figure 4.7. Sketch of the image contrast in over focused Lorentz microscopy images using the Fresnel mode. The magnetic flux indicated by the dash lines are viewed along the optical axis above the sample.

Figure 4.8 shows the magnetic domain configurations in a different area. From the over-focused Lorentz microscopy image in Fig. 4.8 it can be seen that the magnetic domain structure in this area is more regular and most of the domain walls look straight. This can be caused by the relative homogenous thickness distribution in this area. By comparing with the over-focused Lorentz microscopy image in Fig. 4.8b, the domain walls can also be easily recognized from the reconstructed phase image of the hologram as shown in Fig. 4.8c. Several of the domain walls have been marked by white lines. Among them, a typical 180° domain wall which is marked by 'dw'can be seen. By comparing with the Lorentz microscopy image, the magnetic flux directions in the adjacent domains are indicated by white arrows. It also should be noted that near the edge of the sample, this 180° wall further splits into

two 90° walls and form a closure structure. The left 90° wall even further splits into two small 45° walls, then the magnetic flux is parallel to the edge of the sample. The formation of such kind of closure structure is illustrated in Fig. 4.9.

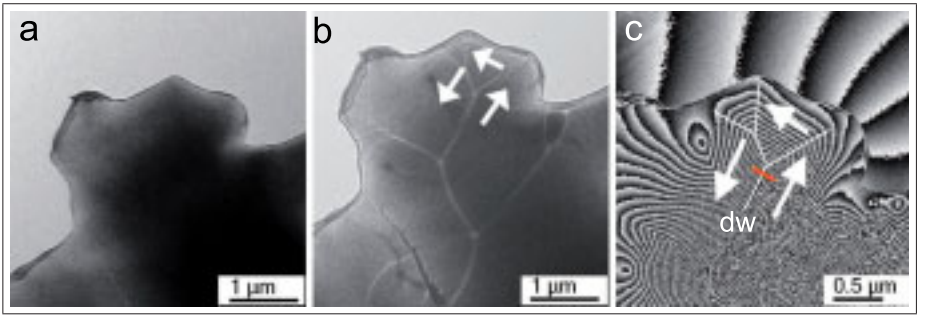

Figure 4.8. Lorentz microscopy images and the reconstructed phase image of $(Fe_{0.5}Co_{0.5})_{80}Nb_4B_{13}Ge_2Cu_1$ heated one hour at 500°C showing a regular magnetic domain structure: (a) in-focus, (b) over-focused Lorentz microscopy image; (c) reconstructed phase image with decreased field of view. A typical 180° domain wall can be recognized from the phase image.

As we have explained, when a large single domain is divided into two small domains with opposite magnetization, the stray field energy will be decreased. If the additional closure structure is formed near the surface of the sample, as shown in Fig. 4.9, the stray field energy could be further decreased. On the other hand, this closure structure also indicates that the sample has a very weak magnetic anisotropy since the magnetic flux can change along the edge of the sample.

To compare with the behavior of the magnetic materials with strong magnetic uniaxial anisotropy, we also imaged the magnetic domain structure of a single crystal cobalt film by Lorentz microscopy. The cobalt crystal with hcp structure has a strong magnetic uniaxial anisotropy. From the over-focused Lorentz microscopy image (Fig. 4.10a) we can see that instead of the formation of the closure structure, due to the strong uniaxial anisotropy, a branch magnetic domain structure is formed near the edge decreasing the stray field energy. As also shown in Fig. 4.10a, the magnetization directions in the branch domains are only parallel or anti-parallel to the main domains,

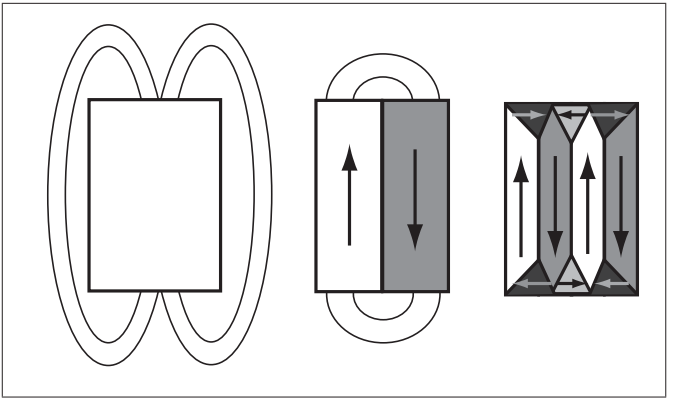

Figure 4.9. Illustration of the formation of the closure structure near the edge of the sample in weak uniaxial anisotropy materials. The closure structure can help to further decrease the stray field energy. Adapted from [57].

but will not change to other non-parallel directions. The formation of this branch structure is illustrated Fig. 4.10b. A more detailed analysis can be found in [57, 58].

4.2.2 Sample annealed at 550°C

Figure 4.11 shows the Lorentz microscopy images of the sample heated one hour at 550°C (a: in-focus, b: over-focused ($\Delta f = -1024\ \mu m$) and c: under-focus ($\Delta f = +1024\ \mu m$)). The images were taken in low magnification with a large field of view ($5.76 \times 5.76\ \mu\text{m}^2$). They give a general information of the magnetic domain distribution in the sample. Though the heating temperature is increased from 500°C to 550°C, the magnetic domain configurations did not change too much. The sizes of the domains are still very large ranging from several hundred nanometers to more than one micrometer.

Before obtaining the electron hologram for visualizing the magnetic flux distribution, the total magnification of the microscope is increased by changing the intermediate lens current to improve the fringe contrast of the electron hologram. The field of view was decreased to $1.82 \times 1.82\ \mu\text{m}^2$ and only the upper end of the peninsula-like structure in Fig. 4.11 was imaged. The large vacuum surrounding the peninsula provides enough space for transmission

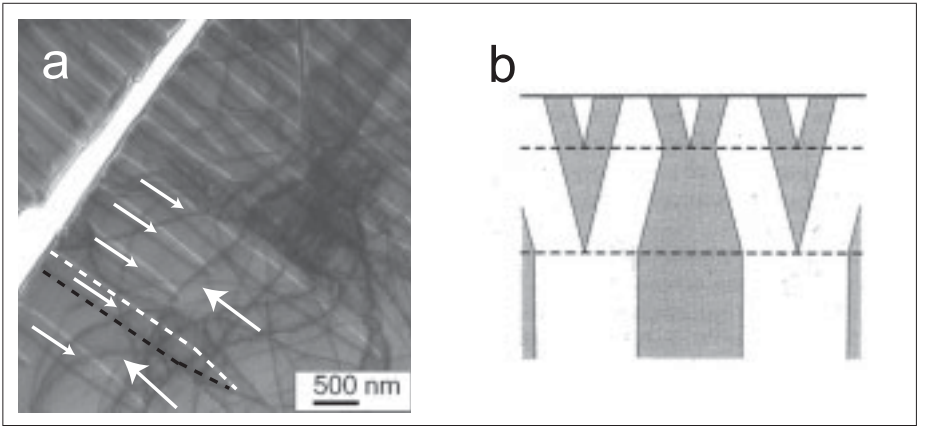

Figure 4.10. Branch structure of magnetic domains in a single crystalline cobalt film near the edge: (a) over-focused Lorentz microscopy image, the magnetization directions marked by white arrows indicate a two phase branching; (b) schematic illustration of the iterated generation of domains towards the surface in strong uniaxial anisotropy materials. (b) taken from [57].

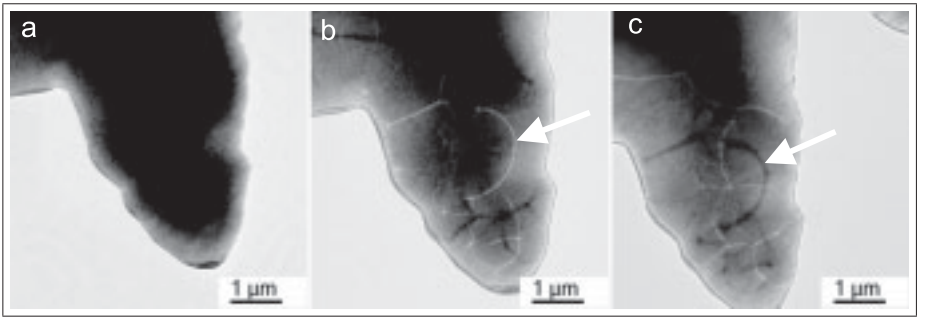

Figure 4.11. Low magnification Fresnel mode Lorentz microscopy images of $(Fe_{0.5}Co_{0.5})_{80}Nb_4B_{13}Ge_2Cu_1$ alloys heated one hour at 550°C: (a) in-focus, (b) over-focus ($\Delta f = -1024\ \mu m$) and (c) under-focus ($\Delta f = +1024\ \mu m$).

of the reference wave. The in-focus and over-focused Lorentz microscopy images with the same field of view were also imaged and compared in Fig. 4.12a and b, while the reconstructed phase image is presented in Fig. 4.12c.

Since a higher magnification is applied, the fine grains can be clearly imaged embedded in the residual matrix (Fig. 4.8a). The average grain size has been measured to about 18 nm from conventional BF images, this value is only slightly larger than that of the 500 °C sample (about 12 nm). It should be noted that a smaller number of the grains are located at the edge of the sample. However this does not mean the sample has an inhomogeneous microstructure. The reason is that the sample thickness at the edge is smaller than the thickness of the central area due to the TEM sample preparation technique. The grains are three-dimensionally distributed in the material. Then, the thinner area will contain fewer grains. Compared with the under-focus Lorentz microscopy image in Fig. 4.12b, we can find that one of the magnetic domain contains several tens or more of such grains.

The corresponding magnetic flux distribution is shown in the reconstructed phase image in Fig. 4.12c. It shows large vortex structures. This is an indication for good soft magnetic properties. The leakage field also could be found in the vacuum close to the edge of the sample. Between two adjacent fringes the phase difference is 2π. The geometric contour line spacing is nearly uniform in most parts of the area and this indicates the uniform magnetic flux density. Close to the lower end of the peninsula the contour line spacing is broadening, this is again due to the thinner thickness in this area. As it was shown in Eq. 4.9, the phase shift gradient also depends on the local thickness.

The reconstructed phase image was further unwrapped and color-mapped, as shown in Fig. 4.13a. The absolute phase values are represented by different colors. The color bar is inserted in the right side of the image. However from the unwrapped phase image, no special information can be obtained. This is because the most useful information is hidden in the phase gradient, not in the absolute phase itself. So the unwrapped phase image was further represented by a surface rendering, as shown in Fig. 4.13b. Similar 3D contour lines are also shown in Fig. 4.13c. Compared with the original phase

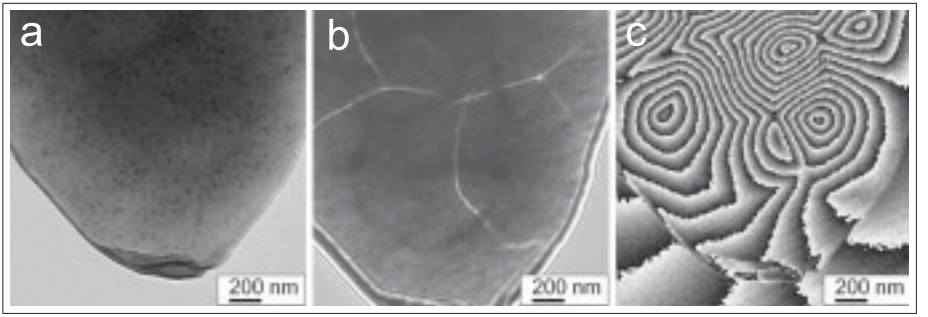

Figure 4.12. Magnetic domain structure of $(Fe_{0.5}Co_{0.5})_{80}Nb_4B_{13}Ge_2Cu_1$ alloys heated one hour at 550°C: (a) in-focus and (b) under-focus Lorentz microscopy images; (c) the reconstructed Phase image of the electron hologram.

image in Fig. 4.12c, we can find that parts of the vortex are shown as peaks, while others are shown as valleys, respectively. It indicates the magnetic flux surrounded by them have different rotational directions.

The raw phase image in Fig. 4.12 shows a detailed magnetic flux distribution in the sample. But it is not easy to distinguish the individual magnetic domains from it. For example, the vortex structures are actually formed with the magnetic flux belonging to different domains. In order to visualize the magnetic domain structures from the phase image, the directions of the phase gradient in each of the pixels were calculated.

The calculations were performed as following. First, the phase image was smoothed to reduce the noise. Second, the two perpendicular components (x and y direction) of the phase gradient $d\phi/dx$ and $d\phi/dy$ were calculated, respectively. Then, the gradient direction was given

$$\theta = \arctan(\frac{d\phi/dy}{d\phi/dx}), \tag{4.14}$$

where θ is the angle between the direction of the phase gradient and the x-axis. After that, the phase gradient directions were further rotated 90° or -90° to represent the magnetic flux directions, since they are perpendicular to each other. It should be noted that the different selections of the side band (top or bottom) during the phase reconstruction will cause a reversal

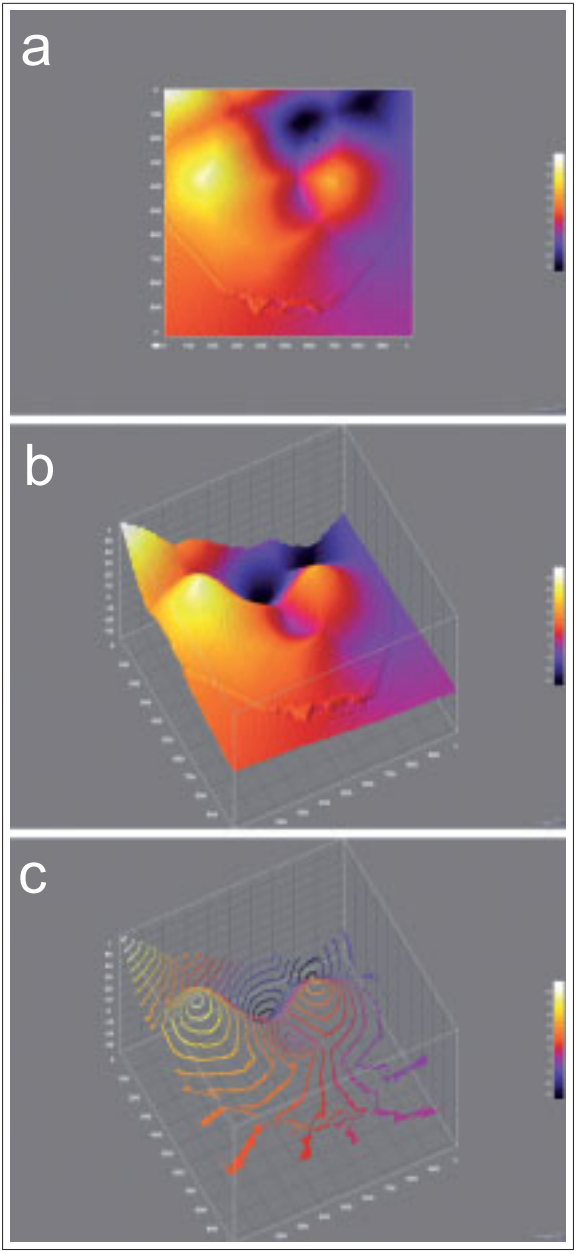

Figure 4.13. Unwrapped phase image of $(Fe_{0.5}Co_{0.5})_{80}Nb_4B_{13}Ge_2Cu_1$ alloys heated one hour at 550°C: (a) color-mapped unwrapped phase image; (b) surface rendering; (c) 3D contour lines. The raw phase image is shown in Fig. 4.12c.

of the phase gradient. The rotation direction should therefore be carefully considered. Here we determine it from the Lorentz microscopy image in Fig. 4.12b. The basic principle is similar as shown in Fig. 4.7. Finally, the magnetic flux directions were denoted by different colors (color plate) and presented in Fig. 4.14. From Fig. 4.14 not only the different domains, but also the magnetic flux directions in each of the domains can easily be recognized. Most of the magnetic domains walls can be determined as 90° type rather than 180° type.

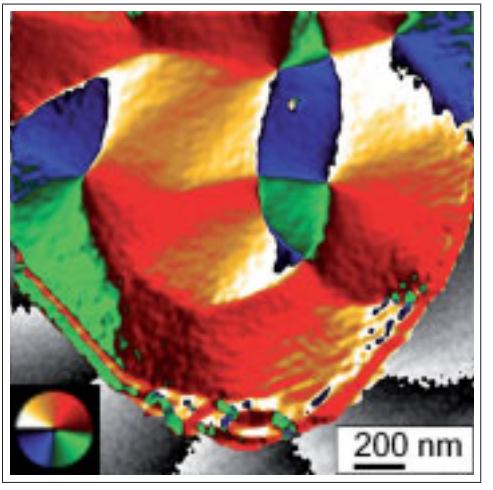

Figure 4.14. Magnetic flux distributions in $(Fe_{0.5}Co_{0.5})_{80}Nb_4B_{13}Ge_2Cu_1$ alloys heated one hour at 550°C. The flux directions are indicated by the color wheel inserted at the lower left. The image was calculated from the raw phase image as shown in Fig. 4.12c.

4.2.3 Sample annealed at 610°C

The microstructure and the magnetic domain structure of the sample heated one hour at 610°C is shown in Fig. 4.15. Similar to the results of BF-TEM and STEM-HAADF investigations, the in-focus Lorentz microscopy image (Fig. 4.15a) indicates that the average grain size is dramatically increased to about 90 nm at this heating temperature. Additionally, the size of the magnetic domains is also significant decreased. From the over-focused Lorentz

microscopy image in Fig. 4.15b, it can be seen that each of the magnetic domain only consists of two or three crystalline grains. The domain walls are pinned by the grains boundaries. The reconstructed phase image in Fig. 4.15c shows that the magnetic flux in this sample is very complex and disordered, which hints to poor softmagnetic properties.

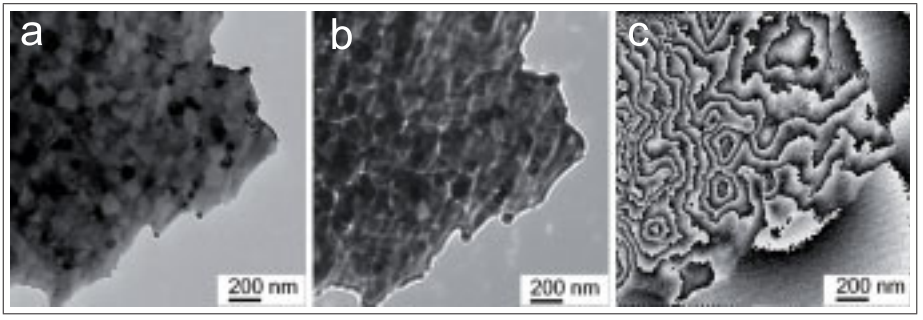

Figure 4.15. Magnetic domain structure of $(Fe_{0.5}Co_{0.5})_{80}Nb_4B_{13}Ge_2Cu_1$ alloys heated one hour at 610°C: (a) in-focus and (b) over-focused Lorentz microscopy images; (c) reconstructed phase image of an electron hologram.

4.3 Determination of domain wall width

As we have observed, the softmagnetic alloys are subdivided into a magnetic domain structure in order to reduce the total energy. Usually the reversal of the magnetic moments in the adjacent magnetic domains can not be finished within an atomic layer, otherwise an extremely high exchange energy will be involved. The magnetic domain walls always have a finite width and the magnetization directions are changed gradually within the wall. In bulk ferromagnetic materials or thick film ferromagnetic materials, Bloch walls, which means the change of the magnetization directions is out of plane, are often observed. This is due to the fact that in thick materials the wall energy and the wall width are mainly determined by the balance of the exchange interaction and the anisotropy energy. However, when the film becomes extremely thin, the demagnetization effect can not be neglected. Then, another type of magnetic domain wall the so called Néel wall will be formed. The

difference between Bloch wall and Néel wall is schematically illustrated in Fig. 4.16 [59]. It can been seen that the magnetization directions in the Néel wall always gradually change in the film plane.

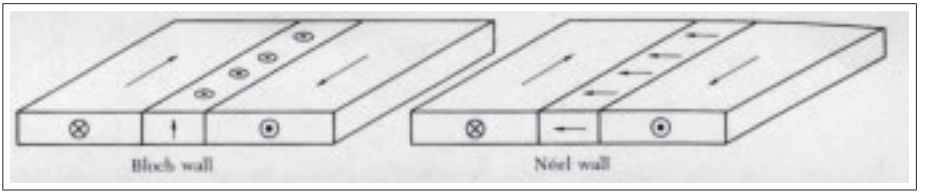

Figure 4.16. The model of Bloch wall and Neel wall [59].

In this section, we will present the experimental measurement of the domain wall width in the $(Fe_{0.5}Co_{0.5})_{80}Nb_4B_{13}Ge_2Cu_1$ alloys. For the sample heated one hour at 500°C , the domain wall width was directly measured from the phase line profile across a 180° domain wall. Alternatively, the domain wall width of the sample heated one hour at 550°C was determined from through-focus series images of Lorentz microscopy. The experimental results will be compared with numerical simulations.

4.3.1 Sample annealed at 500°C

A typical 180° magnetic domain wall of the sample heated one hour at 500°C was selected, where the width of the domain wall was directly measured from the phase image of the electron hologram. The selected domain wall was marked by 'dw', as shown in the reconstructed phase image in Fig. 4.8.

A phase profile along the red line in Fig. 4.8 is plotted in Fig. 4.17. The line scan path is perpendicularly across the domain wall from left to right. Before taking the line scan, the phase image has been unwrapped to remove the phase jump at 2π.

As shown in Fig. 4.17, the phase shift of the electrons firstly increases linearly and shows that the magnetizations in the left part are well aligned. Then the slope of the curve goes shortly approximately flat. This flat region corresponds to the magnetic domain wall where the magnetization directions are rotated. From the length of this part of the flat curve, the magnetic

domain wall width was measured to 32.1 nm. This is much larger than the average size of the grains of about 12 nm. After that, the curve drops and indicates that the magnetization directions in the right part are inversed. The whole curve shows a typical 180° domain structure with a wide domain wall.

In order to compare the experimental results with numerical evaluation of the domain wall width, it is also necessary to know the film thickness t at the wall position. The film thickness can be estimated from the phase gradient of the adjacent domains. According to Eq. 4.12, we assume the film thickness t is constant in this region, the phase gradient will be given by

$$\frac{d\phi(x)}{dx} = -\frac{e}{\hbar} B_n(x) t, \tag{4.15}$$

where e is the electron charge, $\hbar$ is the reduced Planck constant and $B_n(x)$ is the magnetic flux density. Then the film thickness t can be calculated as

$$t = -\frac{\hbar}{e} \frac{\frac{d\phi(x)}{dx}}{B_n(x)}. \tag{4.16}$$

The phase gradient $\frac{d\phi(x)}{dx}$ in the neighbouring domains I or II is indicated by the slope of the curve in Fig. 4.17. The magnetic flux density $B_n(x)$ was used with the value of bulk material B_n=1.30 T. Then the film thickness t near the domain wall was estimated to 70.1 nm.

4.3.2 Numerical evaluation of domain wall width

The experimental result will be compared with numerical evaluation of the domain wall width. The evaluation was carried out applying the method of S. Middelhoek originally used for the calculation of the domain walls (including the wall energy and wall width) in Ni-Fe films [60]. Both the Bloch wall and the Néel wall were calculated, since the samples we have investigated have been prepared as a thin film for electron transmission in TEM. In such thin films (thickness less than 100 nm), both of these two types of domain walls can exist.

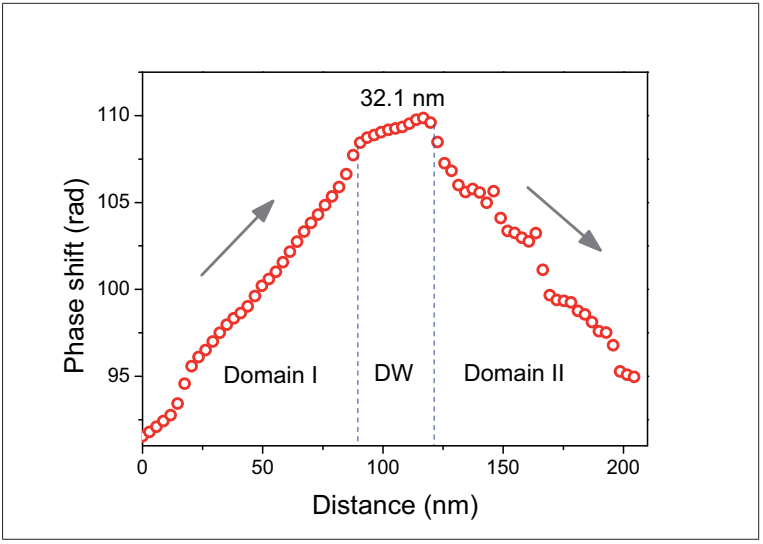

Figure 4.17. Phase profile across a typical 180° domain of the alloys heated one hour at 500°C. The profile is along the red line in Fig. 4.8.

Bloch wall

The model for Bloch wall simulation is assumed as an 180° wall parallel to the easy magnetization direction [60]. The magnetization directions inside of the wall can be expressed as:

$$\phi = \pi(x/a), \tag{4.17}$$

where ϕ is the angle between the magnetization and a direction in the plane of the wall and perpendicular to the film plane. a is the domain wall width and x range from $-a/2 \leq x \leq +a/2$. The exchange energy density E_A is written as

$$E_A = A(d\phi/dx)^2 = A(\pi/a)^2, \tag{4.18}$$

where A is the exchange energy constant. The mean anisotropy energy density is given by

$$E_K = \frac{1}{a}\int_{-a/2}^{+a/2} K\cos^2\phi dx = \frac{1}{2}K, \tag{4.19}$$

here K is the anisotropy constant. Finally, the demagnetization energy density E_D is given by

$$E_D = \frac{\mu_0}{4}\frac{a}{a+t}M_s^2, \tag{4.20}$$

where μ_0 is the permeability in the vacuum ($\mu_0 = 4\pi \times 10^{-7} H/m$), t is the sample thickness and M_s is the saturation magnetization. The detailed calculation of the demagnetization energy density E_D can be found in [60].

The total wall energy density E_B is the sum of the exchange, anisotropy and demagnetization energy densities,

$$E_B = E_A + E_K + E_D. \tag{4.21}$$

After multiplying the wall energy density E_B by the wall width a, we will get the total wall energy γ_B

$$\gamma_B = E_B \times a = A\pi^2/a + \frac{1}{2}aK + \frac{\mu_0}{4}\frac{a^2}{a+t}M_s^2. \tag{4.22}$$

Then the wall width a can be calculated from the minimized wall energy γ_B refered to a. This means

$$\frac{\partial \gamma_B}{\partial a} = -A\pi^2/a^2 + \frac{1}{2}K + \frac{\mu_0}{4}\frac{a^2+2at}{(a+t)^2}M_s^2 = 0 \tag{4.23}$$

For a thick film $t \gg a$, the third term in Eq. 4.23 can be neglected. In this case the wall energy γ_B and the wall width a is given by

$$\gamma_B = \sqrt{2}\,\pi\sqrt{AK}, \tag{4.24}$$

and

$$a = \sqrt{\frac{A}{K}}. \tag{4.25}$$

Néel wall

The evaluation of wall energy and wall width in a Néel wall is similar to that of a Bloch wall. Here the parameter ϕ in Eq. 4.17 refers to the angle between the magnetization and a direction normal to the plane of the wall and in the

film plane [60]. The wall energy γ_e for the Néel wall is given by [60]

$$\gamma_N = A\pi^2/a + \frac{1}{2}aK + \frac{\mu_0}{4}\frac{at}{a+t}M_s^2 \tag{4.26}$$

The minimization of the energy with respect to the wall width a is

$$\frac{\partial \gamma_N}{\partial a} = -A\pi^2/a^2 + \frac{1}{2}K + \frac{\mu_0}{4}\frac{t^2}{(a+t)^2}M_s^2 = 0 \tag{4.27}$$

Discussion

The numerical evaluation of domain wall energy against the sample thickness in the Bloch wall and the Néel wall are compared in Fig. 4.18. The following parameters are used for the simulation: The effective anisotropy constant K=1 J/m^3, the exchange constant A=2 $\times$ $10^{-11}J/m$, and the saturation magnetization Ms=1.088$\times 10^{-6}A/m$ (determined from experimental data).

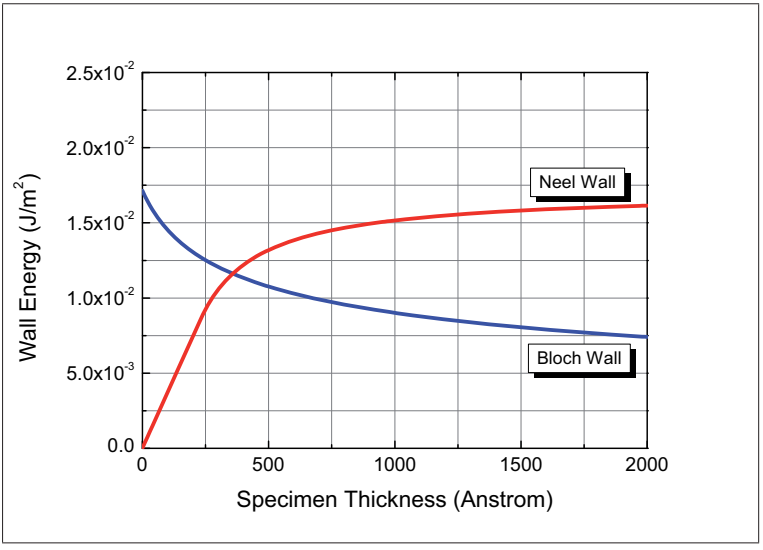

Figure 4.18. Wall energy of a Bloch wall and Neel wall as a function of the sample thickness.

Figure 4.18 exhibits when the sample thickness is larger than 36 nm, a Bloch wall energy γ_B is smaller than a Néel wall energy. This means the

Bloch walls can easily be formed. Below this thickness, the Néel walls will exist.

The film thickness at the domain wall marked by 'dw' in Fig. 4.8 has been determined as 70.1 nm. since this value is much larger than the critical thickness for the formation of Néel wall (36 nm), the domain wall type can then be determined as Bloch wall. Further, according to the relationship between the wall width and the film thickness as shown in Fig. 4.19 (Bloch wall), the evaluated Bloch wall width is 31.8 nm at such film thickness (70.1 nm). This value agrees well with the experimental measurement of the domain wall width of 32.1 nm.

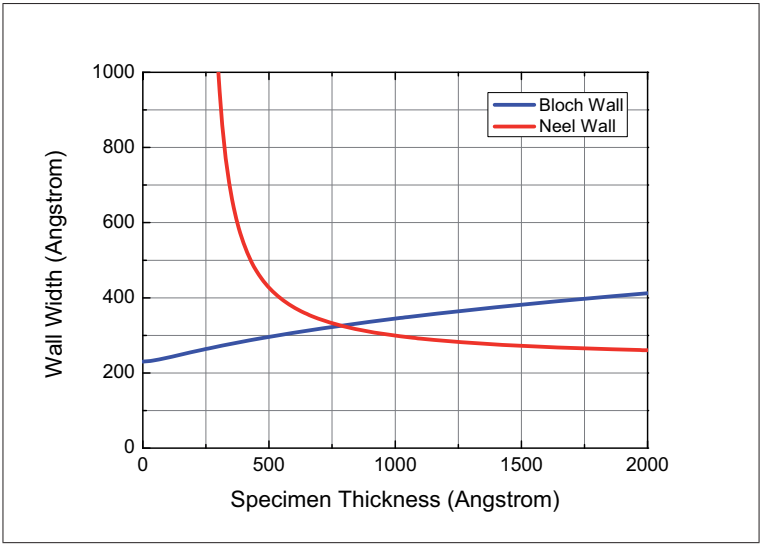

Figure 4.19. Wall width of a Bloch wall and Neel wall as a function of the sample thickness.

4.3.3 Sample annealed at 550°C

For the sample heated one hour at 550°C, most of the walls which we observed from the phase images are of 90°-type. It is not easy to measure the wall width from the phase line scan across a 90°-type wall. Therefore, another method, the so called defocus series of Lorentz microscopy images was used

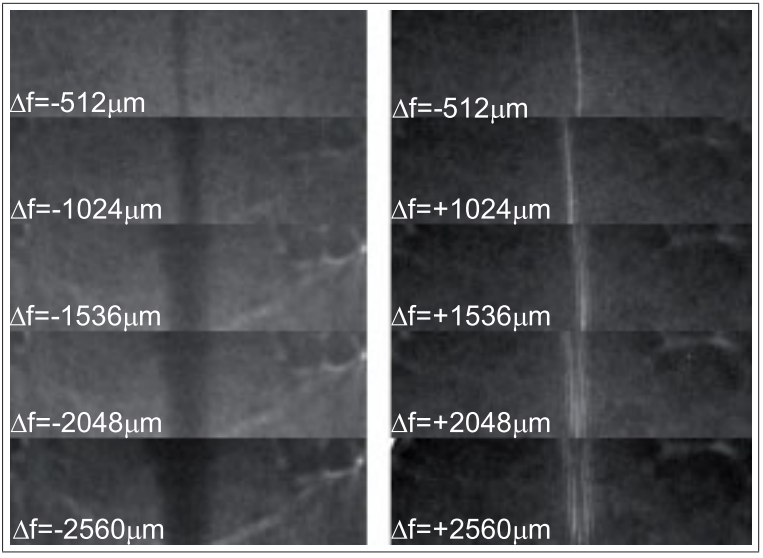

Figure 4.20. Defocus series of Lorentz microscopy images of $(Fe_{0.5}Co_{0.5})_{80}Nb_4B_{13}Ge_2Cu_1$ alloys heated one hour at 550°C.

for the wall width determination. Figure 4.20 shows such defocus series of Lorentz microscopy images of the domain wall in the above mentioned alloy sample. The left column shows the wall with divergent contrast whereas the right column shows the convergent contrast. For both focus conditions, the shadow of the domain wall D_{sw} is increased with the defocus distance Δf and is given by

$$d_{sw}(\Delta f) = D_w + 2\Delta f \bullet \Psi, \tag{4.28}$$

where D_w is the actual wall width and Ψ is the electrons deflection angle due to the Lorentz force. It can been seen, when the defocus value is zero, it yields $d_{sw}(0) = D_w$. However in practice we can not image the domain wall at the exact focus value ($\Delta f = 0$) since there will be no contrast. The $d_{sw}(0)$ can be estimated from a linear fit of the measured $d_{sw}(\Delta f)$ for different defocus values, as shown in Fig. 4.21. It should be noted that the images are recorded under large defocus values, the accuracy of the thickness determination of this method is less than the direct measurement from the phase images.

By a linear fit as shown in Fig. 4.21 we can estimate the domain wall

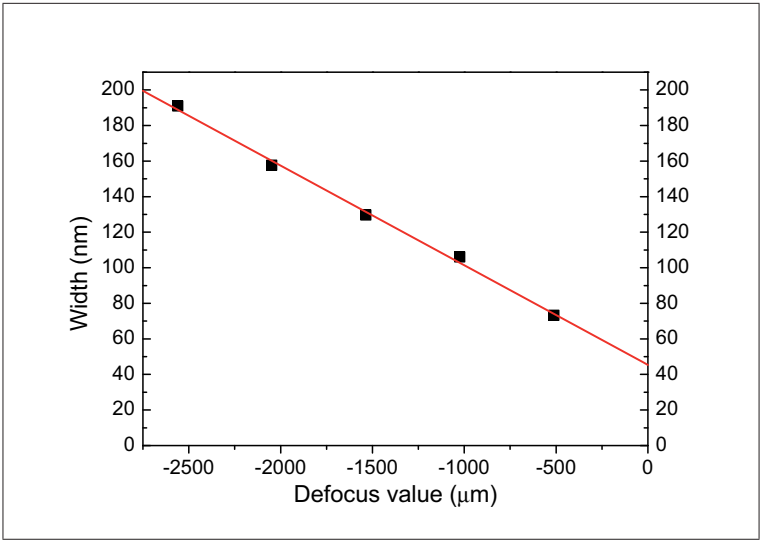

Figure 4.21. Determination of domain wall width of $(Fe_{0.5}Co_{0.5})_{80}Nb_4B_{13}Ge_2Cu_1$ alloys heated one hour at 550°C from defocus series of Lorentz microscopy images.

width D_w is 45.4 nm for Fig. 4.20. The average grain size is about 18 nm for this sample. Here the domain wall width is still much larger than the grain sizes.

4.4 Quantitative measurement of magnetic flux density

In the last section, we estimated the sample thickness from the phase image by using the saturation flux density of the bulk sample. On the other hand, if the sample thickness is known, we can quantitatively measure the local magnetic flux density from the phase image. According to Eq. 4.8, in an area with homogenous thickness the mean inner potential contribution to the phase gradient will be zero. Then the local magnetic flux density B is determined by

$$B = -(\frac{\hbar}{et})\frac{d\phi}{dx}, \tag{4.29}$$

where $\hbar$ is the reduced Planck constant, e is the electron charge, t is the sample thickness and $\frac{d\phi}{dx}$ is the phase gradient perpendicular to the x direction.

Several methods have been developed for thickness determination in TEM, including the convergent beam electron diffraction (CBED), the log-ratio method of electron energy loss spectroscopy (EELS) and the determination of mean inner potential (MIP) contribution to electron phase shift by electron holography. The last method will be used for reconstruction of 3D Ge-Si islands described in chapter 5. For the task described here we used the EELS log-ratio method. This selection is due to the following reasons: First, though the CBED method can provide a high accuracy for thickness determination, the method is only applicable for crystalline samples but not for nanocrystalline materials with an embedded amorphous phase. Second, as we will see the determination of MIP contribution to the electron phase can provide a fast thickness mapping of the large area. Unfortunately, it requires the determination of the independent contribution to phase shift from the MIP. As we have mentioned at the beginning of this chapter, it is not easy to separate this part of contribution from the total phase shift in nanocrystalline soft magnetic materials. It should be noted that this is different from the situation in Eq. 4.29. There, by selecting the area with homogenous thickness, we only remove the MIP contribution to phase gradient, but not the phase itself.

4.4.1 EELS log-ratio method for thickness determination

When high energy electrons transmit through the sample, they will lose some energy due to inelastic scattering. The energy loss can be quantitatively measured by using an EELS spectrometer installed at the TEM. The most commonly used spectrometer type in TEM is a magnetic-prism spectrometer, which can be divided into post column filter and in-column Ω-filter. In this work, the energy loss spectra were measured within an in-column Ω-filter which is built in the JEOL-2200FS microscope. Figure 4.22 shows a typical EELS spectrum collected from the sample $(Fe_{0.5}Co_{0.5})_{80}Nb_4B_{13}Ge_2Cu_1$

heated one hour at 550°C. This spectrum is extracted from a series of STEM-EELS line scan spectra as shown in Fig. 4.22. The strongest peak in the spectrum corresponds to the zero-loss energy, while the area in the right side of the zero-loss peak indicates the energy loss due to different inelastic processes. For example, the first peak in the right side of the zero-loss peak comes from the collective excitation of the valence electrons, which is also called plasmon excitation. For thickness determination, we will use the whole area of the energy loss.

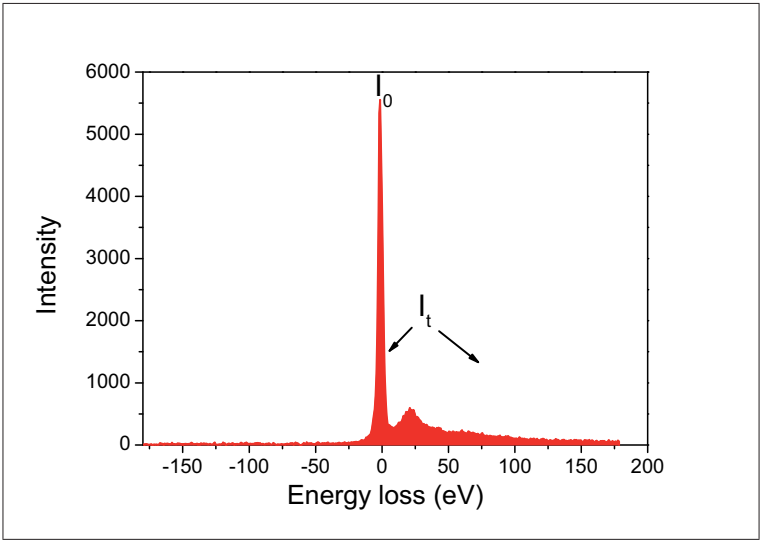

Figure 4.22. EELS spectrum of $(Fe_{0.5}Co_{0.5})_{80}Nb_4B_{13}Ge_2Cu_1$ alloys heated one hour at 550°C. I_0 indicates the area under the zero-loss peak while I_t indicates the total area of the spectrum. This spectrum was extracted from a series of EELS line scan spectra as shown in Fig. 4.23.

With the EELS log-ratio method, the thickness t will be determined as

$$t = \frac{1}{\lambda} \ln I_t / I_0, \tag{4.30}$$

where λ is the total mean free path length (MFP) for all the inelastic scattering, I_t is the area under the whole spectrum and I_0 is the area under the zero-loss peak [61]. As shown in Fig. 4.23, I_t and I_0 can be measured from the experimental spectrum, the unknown parameter is λ.

In practice, a collection aperture (objective lens aperture or energy filter entrance aperture) is used to restrict the scattering angles, λ must be interpreted as an effective mean free path length $\lambda(\beta)$, where β is the maximum collection angle [61].

However, only for few materials the MFP λ have been measured from EELS experiments where the sample thickness was known. Here we use the parameterization results based on many experimental investigations [61],

$$\lambda = \frac{106F\frac{E_0}{E_m}}{\ln(2\beta\frac{E_0}{E_m})}, \tag{4.31}$$

where λ is given in nm, E_0 is the incident electron energy and is given in keV, β is the collection semi-angle and given in mrad, F is a relativistic correction factor,

$$F = \frac{1+\frac{E_0}{1022}}{(1+\frac{E_0}{511})^2}. \tag{4.32}$$

For the accelerating voltage of 200 kV, the relativistic factor F is 0.618. The last unknown parameter in Eq. 4.31 is the average energy loss E_m, which is given in eV. The parameter E_m can be obtained from the approximation formula [62]:

$$E_m = 7.6Z^{0.36}, \tag{4.33}$$

where Z is the atomic number. For compounds, neglecting the solid-state effects, the effective atomic number Z could be given by

$$Z \approx \frac{\sum_i f_i {Z_i}^{1.3}}{\sum_i f_i {Z_i}^{0.3}} \tag{4.34}$$

The proportion of the various elements and their atomic numbers in the alloys $Fe_{40}Co_{40}Nb_4B_{13}Ge_2Cu_1$ are listed in Table 4.1.

Then the effective atom number Z_{eff} can be calculated as 25.57. By substituting Z_{eff} into Eq. 4.33, we get the average energy loss E_m of 24.412 eV. So the inelastic MFP λ can be written as

$$\lambda = \frac{900.63}{2.79647 + \ln\beta}\,(nm) \tag{4.35}$$

Element	Fe	Co	Nb	B	Ge	Cu
Atom number	26	27	41	5	32	29
Composition (%)	40	40	4	13	2	1

Table 4.1. The amount of the different elements and their atomic numbers in $Fe_{40}Co_{40}Nb_4B_{13}Ge_2Cu_1$ alloy.

The collection semiangle β can be selected either by the objective lens aperture (independent of the camera length) or by the entrance aperture (ENTA) of the energy filter. In the JEOL 2200FS microscope with ultra-high resolution (UHR) configuration, the normal in-polepiece gap objective lens aperture is replaced by a lower polepiece high contrast aperture (HCA) due to the confinement of the small gap space. On the other hand, the ENTA is installed after the intermediate lenses and before the Ω filter. Thus, when using ENTA, the collection semiangle β not only depends on the size of the ENTA aperture, but also changes with the camera length. Table 4.2 and Table 4.3 show the collection semiangle β for different HCA and ENTA (camera length 60 cm) in STEM mode in JEOL 2200FS microscope. The data were measured from the diffraction patterns by using a GaAS crystal.

HCA	1	2	3	4
β (mrad)	35.79	18.04	6.29	2.77

Table 4.2. Collection semiangles β for different high contrast apertures (HCA) in STEM mode (independent of the camera length).

ENTA	1	2	3	4
β (mrad)	32.74	15.45	10.82	6.01

Table 4.3. Collection semiangles β for different entrance apertures (ENTA) in STEM mode with a camera length 60 cm.

4.4.2 Determination of magnetic flux density

The EELS spectra were obtained in the JEOL 2200FS microscope with an in-column Ω filter. The operation was performed in STEM mode with a spot size of 0.2 nm and camera length of 60 cm. The collection semiangle was limited to 10.82 mrad by an ENTA located before the energy filter. From Eq. 4.35, the effective MFP λ for $Fe_{40}Co_{40}Nb_4B_{13}Ge_2Cu_1$ alloys can be estimated as 103.6 nm.

A series of EELS line-scan spectra were obtained in STEM-HAADF imaging mode and plotted three-dimensionally in Fig. 4.23. The two perpendicularly in-plane directions correspond to the line scan positions and the energy loss, respect., while the information from the height corresponds to the total count of energy loss. The path of the line scan (see Fig. 4.24) has been carefully selected in such a way that it is perpendicular to the phase contour lines on the phase image (Fig. 4.12c) and then parallel to the direction of the phase gradient.

Subsequently by using Eq. 4.30 with λ=103.6 nm, the spectra were transformed to the thickness profile, as shown in Fig. 4.24b. It can be seen that the thickness is relatively homogenous and the average value is t=74.2 nm. According to Eq. 4.9, the MIP contribution to the phase gradient is zero with homogenous thickness. And the magnetic flux density is given by Eq. 4.29.

The relative phase shift along the same path is compared in Fig. 4.24c. Before taking the phase profile, the raw phase image (Fig. 4.12c) has been unwrapped to remove the phase jump at 2π. We can see that with homogenous thickness, the phase shift is linearly increased along the path, and the gradient of the linear fitted phase profile is $d\phi/dx = 115.9$ rad/μm. By substituting the thickness t and the phase gradient $d\phi/dx$ in Eq. 4.29, the local magnetic flux density B is then calculated to about 1.0 T.

The determined magnetic flux density is about 20% smaller than the saturation flux density of 1.3 T measured from the bulk sample. This can be caused by the following reasons. First, the magnetic flux density of the thin film sample could be different from that of the bulk sample. Second,

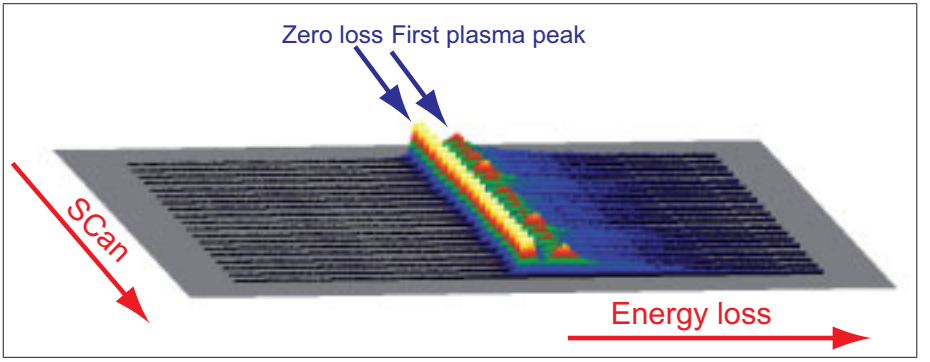

Figure 4.23. EELS line scan spectra of $(Fe_{0.5}Co_{0.5})_{80}Nb_4B_{13}Ge_2Cu_1$ alloys heated one hour at 550°C.

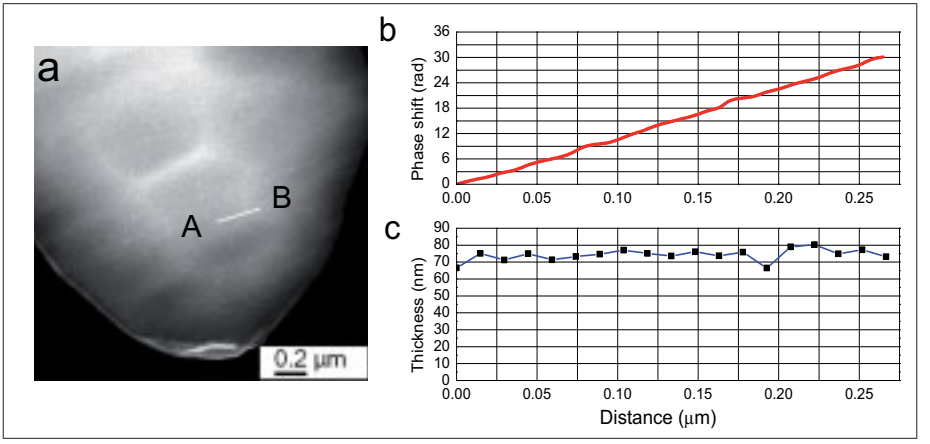

Figure 4.24. (a) STEM-HAADF image of $(Fe_{0.5}Co_{0.5})_{80}Nb_4B_{13}Ge_2Cu_1$ alloys heated one hour at 550°C; (b) unwrapped phase profile; (c) corresponding thickness profile obtained from the EELS spectrum. The profiles were taken along the path AB on the left-hand STEM-HAADF image.

electron holography can only image the in-plane component of the magnetic flux. Third, the largest error can occur in the EELS log-ratio method itself. For example, the mean free path is estimated from a parameterization based on many experimental measurements. Several approximations were used in this parameterization, such as the calculation of the mean energy loss E_m using the Lentz atomic model and neglecting the difference between the real structure of the materials. It predicts the same mean free path length for crystalline and amorphous samples [61]. Then, the accuracy of this method for the thickness determination can be differ in the range of $\pm 20\%$.

4.5 Dynamical magnetization

In this section, we will discuss the investigation of the dynamical magnetization behavior of the FeCo-based alloys by in-situ magnetizing experiments in TEM. An external magnetic field was applied to the samples and the domain wall motion and reversal of the magnetization were observed in both Lorentz microscopy and electron holography.

In general, there are two methods to generate the external applied field in TEM. One is using a magnetic sample holder. This method can provide an accurate applied field. This method needs a special designed sample holder. Thus a more convenient way is given by using the objective lens. As we already mentioned, for structure observation of magnetic domains in TEM, the main objective lens is normally switched off. If we again slightly excite the objective lens and tilt the sample, then an in-plane external field will be applied at the sample as shown in Fig. 4.25. The magnitude and directions can be controlled by the tilting angle θ, where

$$H_{//} = H_{obj} \times \sin(\theta) \tag{4.36}$$

The disadvantage of this method is the difficulty of determining the objective lens field quantitatively. One method measures directly the field by a Hall probe device. However this needs to modify the sample holder to mount the Hall probe device or to open the column of the microscope. An

alternative method is to calibrate the field by using a permanent magnet material with known magnetic response [63]. First, the sample which has been demagnetized will be inserted into the TEM and an objective lens field will be applied on it. Then the field will be reduced to zero. After that the sample will be taken out from the TEM and the remnant magnetization will be measured by superconducting quantum interference device (SQUID). Since the remanence state is associated with the magnitude of the applied field in TEM, the objective lens field will be quantitatively determined. To measure each data point (including the field magnitude and the corresponding objective lens potential (or current)), the sample should be inserted to and taken out from the microscope. Then only very limited data can be achieved and the other data needs a curve fit. In this work, the objective lens field is only roughly estimated in such a way. If we assume that the maximum objective lens field is 20 kOe ($\mu_0 H = 2T$ in SI units) which is generated by the saturation lens current I_0, then the lens field H_{obj} corresponding to the lens current I is given by

$$H_{obj} = 20 \times \frac{I}{I_0}(kOe) \tag{4.37}$$

The excited objective lens current I is fixed at 0.78% of the saturation current I_0. The objective lens field is then estimated to 156 Oe. It should be noted that the additional magnetic field excited either by the magnetic sample holder or by the main objective lens can destroy the normal electron optical conditions preset in Lorentz mode. Fortunately here we investigated soft magnetic materials which can be easily magnetized and demagnetized, thus a very weakly excited objective lens field is sufficient. As we have seen the lens field which was actually used is only about 156 Oe. Then no additional electron optical compensation is necessary.

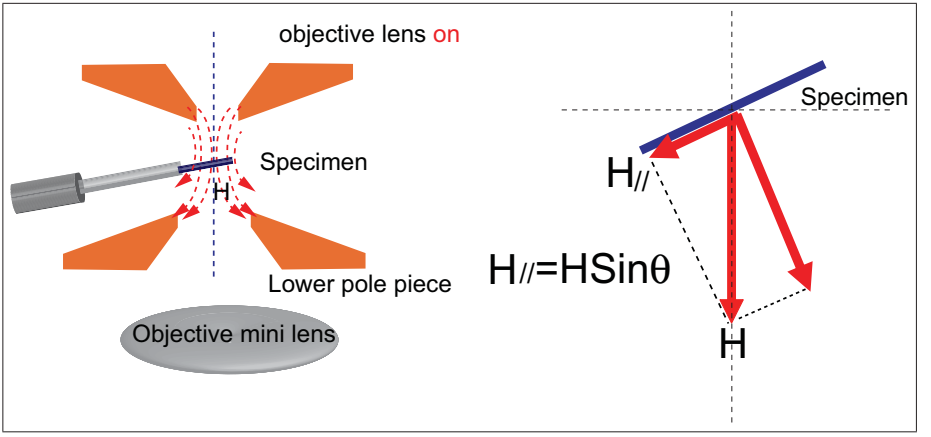

Figure 4.25. Illustration of the in-situ applied field experiment in TEM by tilting the sample in a weakly excited objective lens field.

4.5.1 Observation of the dynamical magnetization of the sample annealed at 550°C by Lorentz microscopy

First, the dynamical magnetization process of the sample heated one hour at 550°C was observed by Lorentz microscopy and is illustrated in Fig. 4.26. The tilting directions are indicated by arrows in the first image. The tilting angles marked in each of the image were directly read out from the TEM goniometer. It should be noted that for an ion milling sample, the wedge-shaped edge will provide several degrees of additional angles to the direction where the thickness is increasing, as given in this figure. Then the zero in-plane field is not coincided with the zero-degree tilting angle which was read out from the goniometer.

From Fig. 4.26 we can see when the tilting angle was initially set to 15.0°, only very few and weak domain walls can be seen. This indicates that most of the magnetizations were aligned along the $H_{//}$. While the strength of the $H_{//}$ has been further decreased by decreasing the tilting angle, more and more magnetic domain walls were visible forming the domain structure. When the sample was tilted to 5.3°, most of the magnetic domains walls can

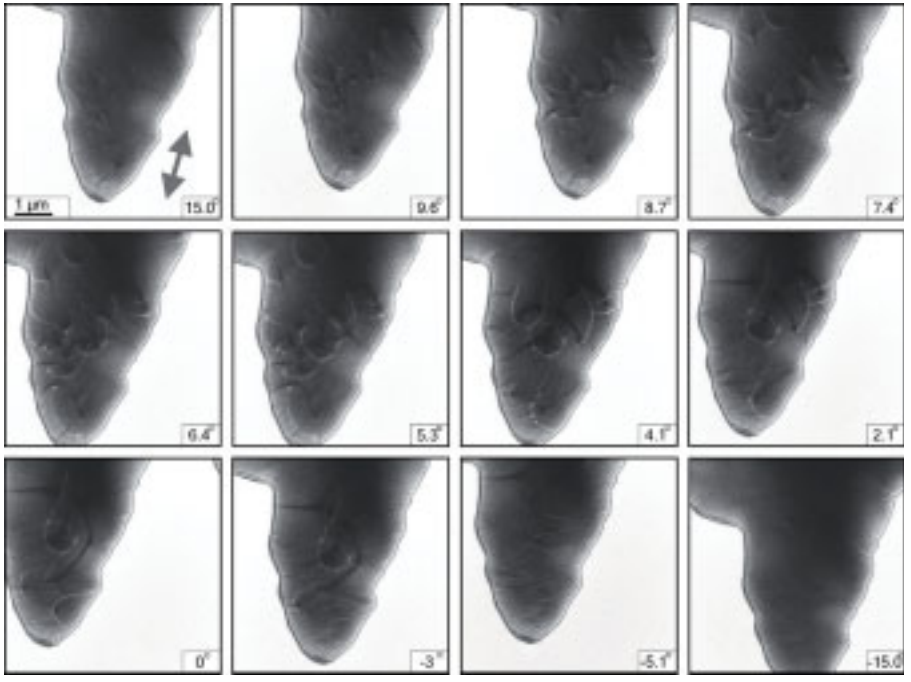

Figure 4.26. Tilting series of Lorentz microscopy images of $(Fe_{0.5}Co_{0.5})_{80}Nb_4B_{13}Ge_2Cu_1$ alloys heated one hour at 550°C. The objective lens was weakly excited to 0.78% of the saturation current.

be seen. This indicates the in-plane field direction has been reversed and the field magnitude is close to the coercivity field H_c.

With further tilting, the small magnetic domains began to emerge into large domains due to the increased $H_{//}$ in opposite direction. The domain wall motion was also observed in this process. It should be noted that during the continuous tilting, which means the strength of $H_{//}$ is also continually increased, the domain wall motion was not showing a smooth change. For example, changing the tilting angle from 5.3° to 4.1°, the domain configuration was keeping constant. Then, when the tilting angle was close to 4.1°, the domain walls suddenly jumped from one to another position and a new domain configuration was formed, as shown in the image marked by 4.1°. The domain wall motion between the 4.1°, 2.1°, 0°, and -3° were also finished in such kind of abrupt jumps. This interesting phenomenon is called Barkhausen effect and is often observed in the magnetization curve of ferromagnets. As shown in Fig. 4.27, the enlarged magnetization curve shows that the magnetization as a function of the field is not smooth but increases in steps. The reason for these steps can be explained as abruptly change of the domain configuration due to the domain walls pinning. Imaging the magnetic structure by Lorentz microscopy, we have clearly observed this effect in $(Fe_{0.5}Co_{0.5})_{80}Nb_4B_{13}Ge_2Cu_1$ soft magnetic alloys. It also proves that the reversal of the magnetization in this kind of soft magnetic alloy is at least partly finished through the domain wall motion.

When the tilting angle was further increased to -5.1°, the domain walls disappeared and this indicates that the sample arrives the saturation state. Then, there is no change with further tilting.

From the tilting series images it can be found that the two saturation states are not symmetrical around the zero tilting degree read out from the goniometer. As we have mentioned this is due to the wedged-shape sample, especially when the tilting direction is parallel to the direction with increasing thickness. If we assume that the additional angle induced by the wedged edge is 7.5° (The ion milling angle for the sample preparation is 10° after 30-40 minutes with 4.5kV accelerating voltage, then it will be decreased to 5° after 10-20 minutes at a lower voltage of 2.8-3 kV.). The zero in-plane field could

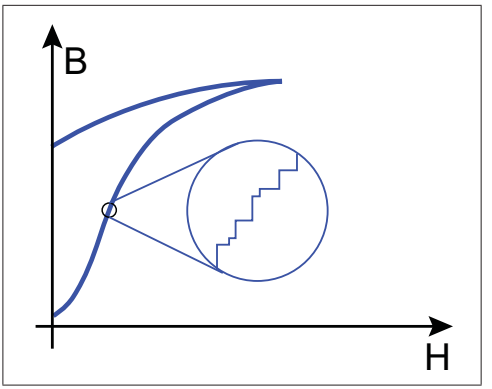

Figure 4.27. Illustration of the Barkhausen effect. The enlarged magnetization curve indicates that the magnetization as a function of the field is not smooth but increases in steps.

be estimated at -7.5° which is read out from the goniometer. From the zero in-plane field at -7.5° to the saturation state at 5.1°, a total tilting angle of 12.6° is necessary. According to Eq. 4.36, the saturation field can be estimated as:

$$H_{sat} = 156Oe \times \sin(12.6°) = 34Oe. \tag{4.38}$$

The sample is then very easily magnetized and demagnetized.

4.5.2 Dynamical magnetization observation of the sample annealed at 550°C by electron holography

The dynamical magnetization of the sample heated at 550°C for one hour was also observed by electron holography. Compared to Lorentz microscopy using the Fresnel mode were only the changes of the magnetic domain configuration during the magnetization can be imaged, the phase images reconstructed from the electron holograms provide a more detailed information of the magnetic flux changing under the applied field. The disadvantage of electron holography is the difficulty to get a live-time observation of the magnetization process. Due to the lack of the sufficient high coherent current, each of the hologram needs a long exposure time (from 4s to 10s). Additionally, in

order to remove the distortion caused by the stray field, a reference hologram should be imaged after the acquisition of the hologram. Then the live-time observation is very difficult.

A series of phase images is shown in Fig. 4.28. These images were reconstructed from holograms which were imaged in Lorentz mode with an objective lens slightly excited at 0.78% of the saturation lens current. The geometric location of the sample in the sample holder, as well as the tilting directions are the same as in the Lorentz microscopy tilting experiment.

At the initial tilting angle of 19.8°, it can be seen that most of the magnetic flux was forced along one direction (parallel to the in-plane applied field $H_{//}$) and only a small vortex structure is left at the bottom right. Then with decreasing tilting angle (decreasing $H_{//}$), the vortex has been grown and this indicates more and more magnetic flux around the vortex center turned away from the $H_{//}$. At the upper part of the images, one can see several other vortexes also began to form. When the sample was tilted to 4.8°, the vortexes grew to the maximum. If we follow the magnetic flux around the vortex center, we will find that the magnetic flux density which is indicated by the phase contour line spacing is nearly the same (neglecting the thickness effect). Since the magnetic flux with opposite directions will cancel out each other, the net value of the magnetic flux is very small. Then this state is close to the zero net flux in the hysteresis loop and the strength of $H_{//}$ is close to the coercivity force H_c.

Since the in-plane field direction has been inverted with increasing the tilting, the vortex began to shrink and indicates that the magnetic flux partly turned to the in-plane applied field direction. At a tilting angle of -5.0° , the complete magnetic flux is aligned along the direction of the $H_{//}$, the domain structures disappeared and correspond to the saturation state in the hysteresis loop. With additional tilting, no changes can be observed.

In order to observe the change of the magnetic domain configurations during the magnetization, the direction of the magnetic flux was further calculated from the phase images in Fig. 4.28 and indexed by different colors (the direction of magnetic flux is perpendicular to the direction of phase gradient). The result is shown in Fig. 4.29. Now the different magnetic

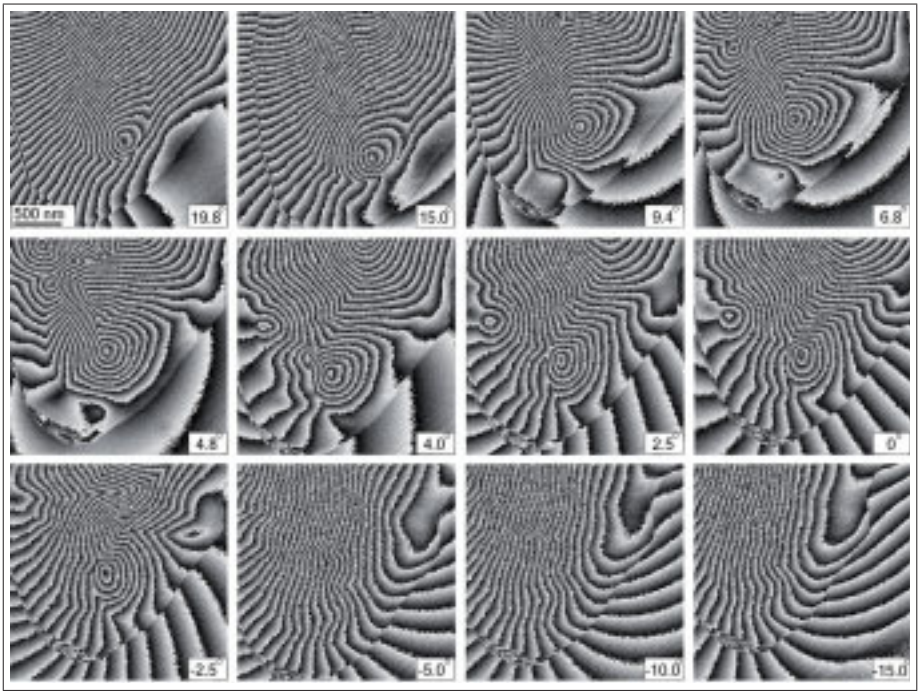

Figure 4.28. Tilting series of reconstructed phase images of $(Fe_{0.5}Co_{0.5})_{80}Nb_4B_{13}Ge_2Cu_1$ alloys heated one hour at 550°C. The objective lens was weakly excited to 0.78% of the saturation current.

domains and the magnetic flux directions inside of the domains can be clearly seen.

From the first image at a tilting angle of 19.8°, it can be seen that inside of the large red zone with an uniform magnetization, several small adjacent domains which are indicated by the yellow, blue and green colors were formed. Then these small domains began to grow with decreasing applied field. It is very interesting to note that during the growth, the relative boundary between them (the domain walls) did not change, so each of the domains was only expanded to the matrix and formed the larger domains. At the tilting angle of 6.8°, the domains grew to the maximum. As we have mentioned, here the applied field is close to the coercivity field. Between the two images of 4.8° and 4.0° , the domain configurations shows a significant change. As we have observed in Lorentz microscopy, this kind of change is due to the sudden jump of the domain walls under the increased in-plane applied field. Finally the domain structure is disappeared. Now the whole sample was magnetized along the blue direction which is opposite to the initial red direction. From both the tilting series of Lorentz microscopy images and the phase images of electron holography, we can conclude that the alloy samples at this heating temperature can easily be magnetized and demagnetized with very few pinning.

4.5.3 Observation of dynamical magnetization of the sample annealed at 610°C

The tilting series of Lorentz microscopy images and electron holography phase images of the sample heated one hour at 610°C is shown in Fig. 4.30, where the top and the bottom lines are the Lorentz microscopy images and the phase images, respectively. The objective lens is still excited to 0.78% of the saturation lens current.

Different from the sample heated at a lower temperature, with the changing applied field, the configuration of the magnetic domains were not significant changed. The domain walls were strongly pinned by grains boundaries. This indicates that the sample has a much higher coercivity. Similarly we can

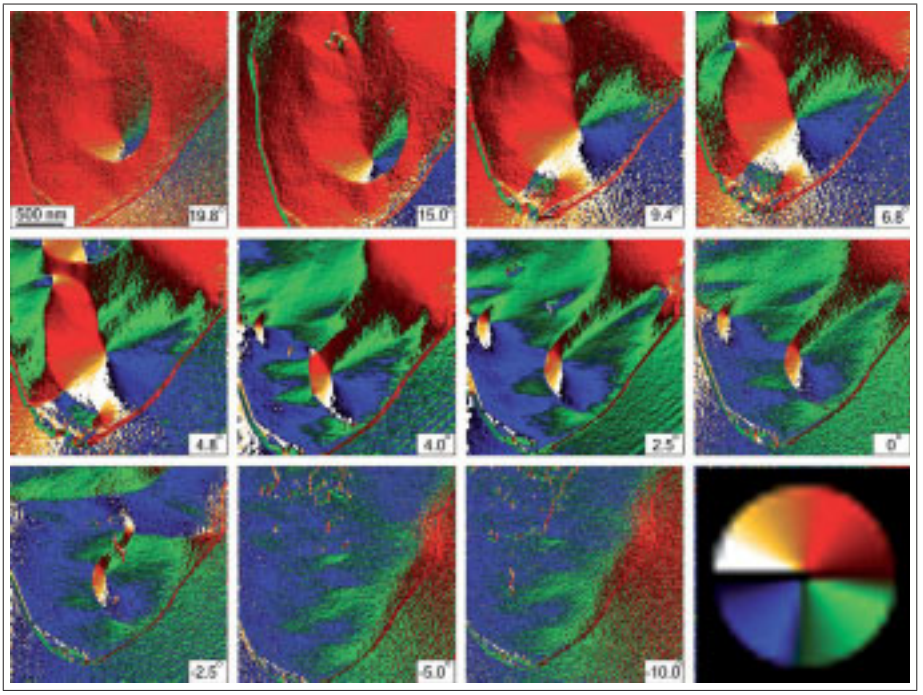

Figure 4.29. Tilting series mapping of magnetic flux direction in $(Fe_{0.5}Co_{0.5})_{80}Nb_4B_{13}Ge_2Cu_1$ alloys heated one hour at 550°C . The magnetic flux direction was calculated from the raw phase images in Fig. 4.28.

see in the phase images, though the sample was tilted to ±15°, the magnetic flux is still disordered. No large homogenous domain can be seen. So the tilting series experiments indicate in this sample heated at higher temperature the coercivity is extremely high due to the strong pinning by the grains boundary.

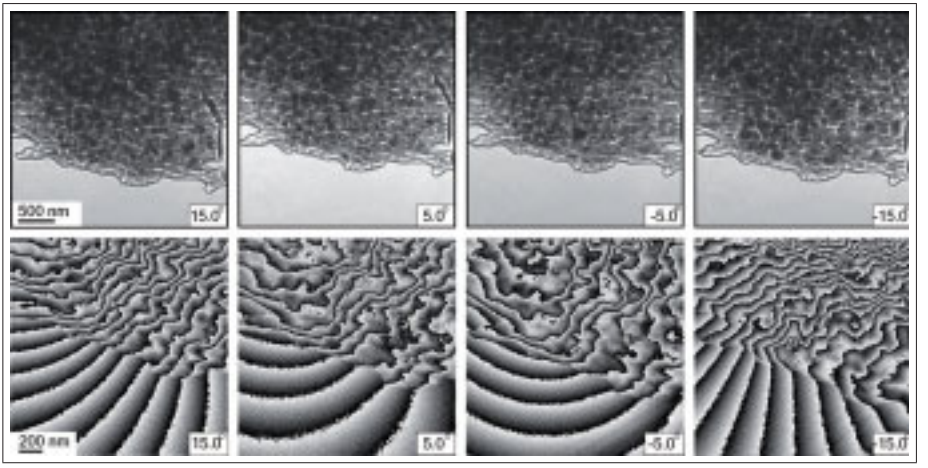

Figure 4.30. Tilting series of magnetic images of $(Fe_{0.5}Co_{0.5})_{80}Nb_4B_{13}Ge_2Cu_1$ alloys heated one hour at 610°C. Upper row: Lorentz microscopy images. Lower row: reconstructed phase images. The objective lens was weakly excited to 0.78% of the saturation current.

4.6 Correlation between microstructure and magnetic domain structure

From previous investigations we found there is a strong correlation between the microstructure and the magnetic domain structure in FeCo-based nanocrystalline alloys systems. The results indicate that the alloys are formed with nano-sized FeCo particles (bcc structure) embedded in an amorphous matrix. The sizes of the crystalline grains are increased with increasing heating temperature. On the other hand, the magnetic domain structures are varied with the grain sizes. At lower heating temperature (500°C and 550°C), the average

grain sizes are about 12 nm and 18 nm, respectively. Correspondingly, both the Lorentz microscopy and the electron holography investigations indicate that the alloys contain large magnetic domains with few pinning sites. The size of the magnetic domains is ranging from several hundred nanometers to several micrometers. Contrary to that, when the heating temperature was increased to 610°C, most of the residual amorphous phase has been transformed to a crystalline phase. The average grain sizes also increase to about 90 nm. In the mean time, the sizes of the magnetic domains dramatically decreased. Each of the domains contains only two or three particles. The magnetic domain wall is also strongly pinned by the grain boundary. The dynamical magnetization experiments further proved that, the alloys heated at lower heating temperature can be easily magnetized and demagnetized, hinting to low coercivity. Contrary, the alloys heated at higher temperatures are strongly pinned by grain boundaries.

Fine grained magnetic materials are conventionally discussed as hard magnetic materials regarding to their magnetic properties [64]. This is due to the fact that the material will be subdivided into single domain particles with the reduction of the grain size. Thus, the coercivity in a fine grained system is normally very large due to the magnetic anisotropy [65]. Magneto-crystalline anisotropy is an intrinsic property of a ferromagnetic crystal, which is related to the crystal symmetry. For example, as shown in Fig. 4.31 [66], in a single iron crystal with bcc structure, $\langle 100 \rangle$ is the "easy direction of magnetization", $\langle 111 \rangle$ is the "hard direction of magnetization", and $\langle 110 \rangle$ is the intermediate direction of magnetization. However, the large magnetocrystalline anisotropy can not explain the soft magnetic behavior of the FeCo nanocrystalline system which we have observed. The phenomenon should be explained by means of the Herzer random anisotropy model [65] [45].

In the random anisotropy model, there is a critical scale which is given by the ferromagnetic exchange length

$$L_0 = \sqrt{A/K_1}, \tag{4.39}$$

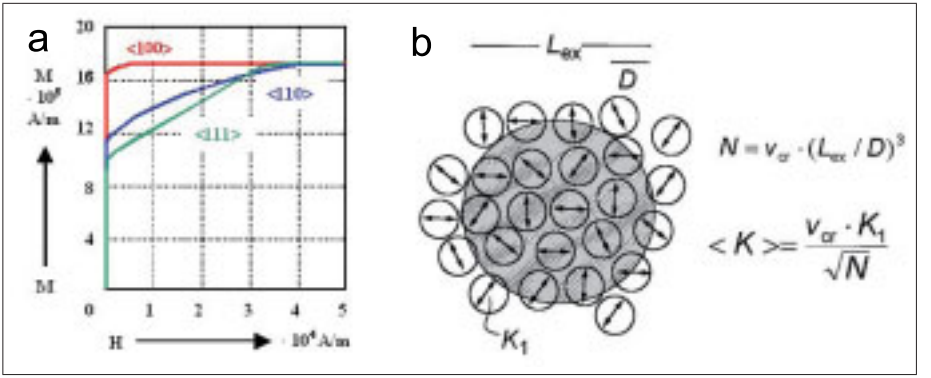

Figure 4.31. (a) Magneto-crystalline anisotropy in iron with bcc structure [66]. (b) Herzer random anisotropy model [45].

where A is the exchange stiffness constant and K_1 is the magneto-crystalline anisotropy. L_0 is in the order of the domain wall width. As we have measured, the domain wall width in FeCo-based nanocrystalline alloys is in the range of 30 nm to 40 nm. When the grain size D is below L_0, the randomly oriented FeCo grains will be ferromagnetically coupled by exchange interaction through the interfacial amorphous matrix. Thus, the effective magneto-crystalline anisotropy is significantly reduced due to the average effect. The magnetization will not follow the randomly oriented easy axis of the individual grains, but is forced to align parallel by exchange interaction. This is the reason that we have observed the large magnetic domains in the alloy systems with average grain size of 12 nm and of 18 nm, respectively. Corresponding to that, the domain wall motion in an external field will not be pinned by the grain boundaries.

The random anisotropy model is schematically illustrated in Fig. 4.31b [45]. The effective magneto-anisotropy is given by

$$\langle K \rangle = v_{cr}^2 D^6 K_1^4 / A^3, \tag{4.40}$$

where v_{cr} is the volume fraction of the grains. This D^6 relationship clearly explained the different magnetization behavior of the FeCo-based nanocrystalline with different grain sizes.

4.7 Fe-based B-free nanocrystalline alloys

4.7.1 Introduction

From the previous investigations, we have found there is a strong structure-property correlation in $(Fe_{0.5}Co_{0.5})_{80}Nb_4B_{13}Ge_2Cu_1$ alloys, that small nanocrystalline grains correspond to better soft magnetic properties. The element B also takes an important role during the nanocrystalline formation, since it increases the glass forming ability and prevents the crystallization of the alloys into undesired large grains [49]. Additionally, the B element also improves the thermal stability of the alloys [49]. The disadvantage is that B is a relative expensive element. Thus, in order to reduce the industrial costs, there is a great interest to develop new B-free nanocrystalline alloys with equivalent soft magnetic properties. In this section, we describe the investigations of the microstructure and the magnetic domain structure of a new Fe-based B-free nanocrystalline soft magnetic alloy $Fe_{79}Zr_6Si_{14}Cu_1$. The design of the $Fe_{79}Zr_6Si_{14}Cu_1$ alloy is based on the combination of the features of commercial Fe-TM (TM= early transition metal) and Fe-Si soft magnetic alloys [49]. The Fe-TM binary system such as Fe-Zr, Fe-Hf, etc. also has a strong glass forming ability. On the other hand, the replacement of B by Si can increase the activation energy barriers in Metglas alloys [67]. The alloy was prepared in a similar way as the FeCo-based nanocrystalline alloys we have previously investigated. First, the alloy melt with nominal composition $Fe_{79}Zr_6Si_{14}Cu_1$ was quenched by spraying it on the surface of a high-speed rotating copper wheel under a pressure of Ar gas through nozzles to obtain an alloy ribbon with thickness 25 μm. Subsequently the amorphous ribbon was heated at 450°C for 2 hours to transform it into a nanocrystalline alloy. TEM samples were prepared by mechanical dimpling followed by Ar-ion milling.

4.7.2 Microstructure characterization

Figure 4.32a shows a conventional BF-TEM image of the $Fe_{79}Zr_6Si_{14}Cu_1$ alloy annealed at 450°C for 2 hour. The morphology of the alloy exhibits a two-phase structure with small particles embedded in the matrix. The average

grain size is only about 14 nm. Two typical particles are indicated by the white arrows. The corresponding SAED pattern is inserted at the upper right of Fig. 1a. The Debye-Scherrer rings show a polycrystalline structure. Indexing of the rings confirms the α Fe with bcc structure. Particularly, a wide halo ring is superimposed on the ring of (110) plane, which indicates that the alloy still contains a large part of residual amorphous phase after annealing at 450°C for 2 hour. Figure 4.32b shows the HRTEM image of the

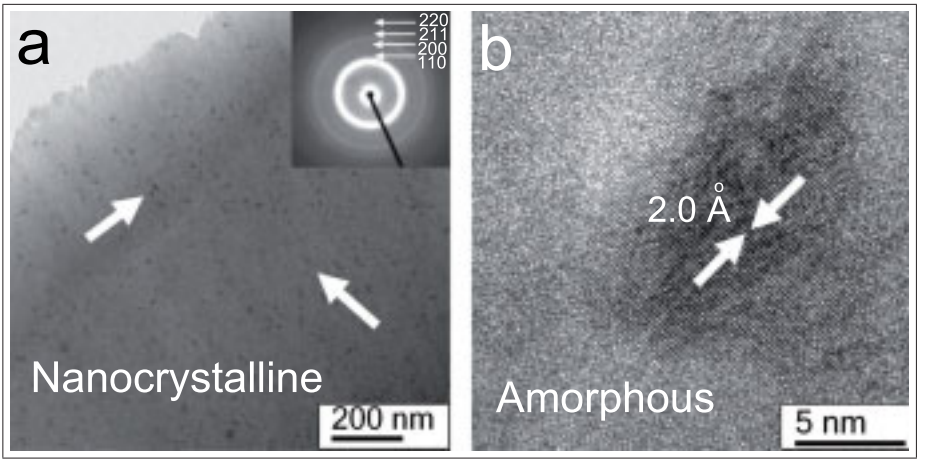

Figure 4.32. Microstructure of $Fe_{79}Zr_6Si_{14}Cu_1$ nanocrystalline alloy heated at 450°C for 2 hour: (a) TEM-BF image, inserted is the corresponding SAED pattern; (b) HRTEM image.

alloy. A nano-sized particle with fringe contrast can be clearly seen embedded in the amorphous matrix. The lattice distance of the grain is measured as 2.0 Å, which is corresponding with the (110) d-value of α-Fe crystalline phase. The structure characterization prove that with the absence of B element, the alloy still forms excellent nanocrystalline structures.

4.7.3 Magnetic domain structure

The magnetic domain structure of the alloy $Fe_{79}Zr_6Si_{14}Cu_1$ was further examined by Lorentz microscopy and electron holography. Both investigations were performed in Lorentz mode with the main objective lens switched off.

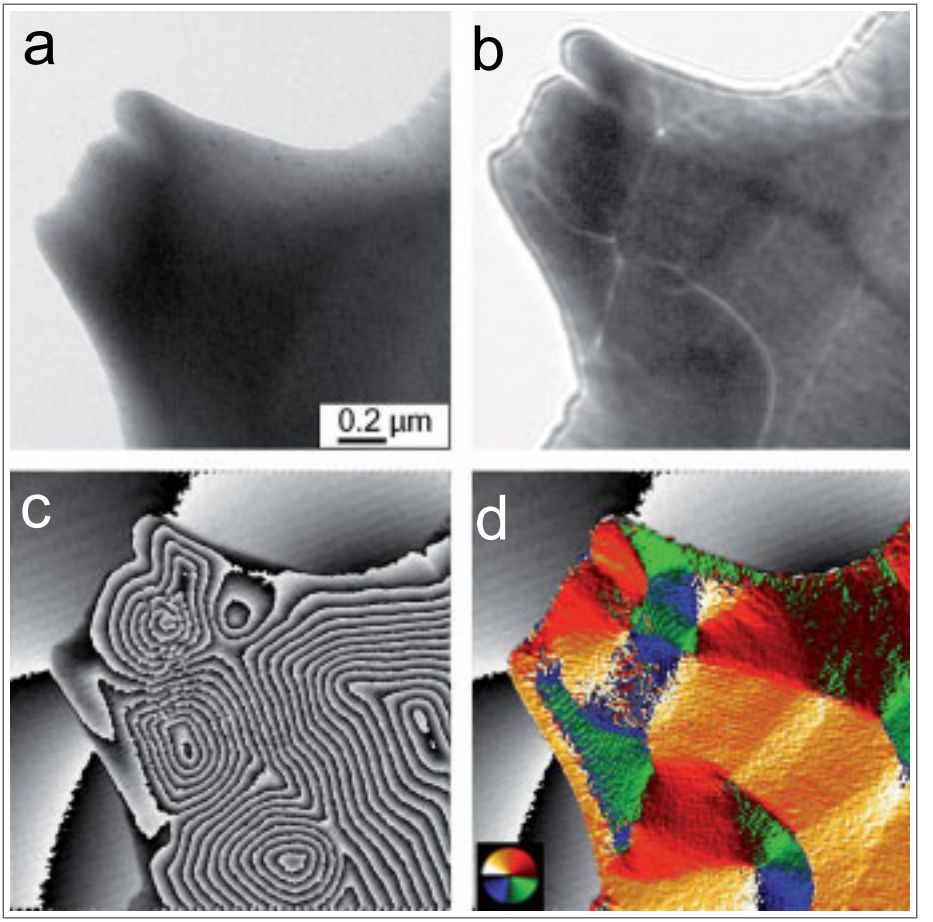

Figure 4.33. Magnetic domain structure of $Fe_{79}Zr_6Si_{14}Cu_1$ nanocrystalline alloys heated at 450°C for 2 hour: (a) in-focus, (b) de-focused Lorentz microscopy image; (c) reconstructed phase image of electron hologram; (d) color mapped magnetic flux directions.

Figure 4.33a shows the Lorentz microscopy image under in-focus imaging condition. It looks like a conventional BF-TEM image without any special magnetic contrast. When the focus condition was changed from in-focus to a large defocus, several bright and dark lines are visible, as shown in Fig. 4.33b. These contrast lines are formed with the convergence or divergence of the deflected electrons due to the magnetic field in the adjacent magnetic domains. Thus, these contrast lines directly indicate the positions of the magnetic domain walls. The size of the magnetic domains is ranging from several hundred nanometers to more than one micrometer. Thus, each of the magnetic domains contains several tens to hundreds grains.

In order to better visualize the magnetic flux inside the sample, electron holography investigations were further performed. Figure 4.33c shows a phase image reconstructed from the recorded electron hologram in Lorentz mode. The black and dark phase contour lines clearly show the distributions of the in-plane component of the magnetic flux. The contour line spacing corresponds to a phase shift of 2π. The varied magnetic flux in different magnetic domains forms large vortex structures. Particularly, the magnetic flux is also changed along the sample edge, hints to low magnetic anisotropy. The leakage field also can be found in the vacuum around the sample.

By calculating the phase gradient directions, the magnetic flux directions were further separated from the raw phase image and represented by different colors, as shown in Fig. 4.33d. Compared with the raw phase image (4.33, different magnetic domains are clearly distinguished.

The dynamical magnetization behavior was further observed by tilting the sample in a weakly excited objective lens field. The in-plane component of the applied filed was changed with the tilting angle. The tilting series phase images reconstructed from the electron holograms were shown in Fig. 4.34. The tilting angles have been marked on each of the images. In order to compare the results with the results of $(Fe_{0.5}Co_{0.5})_{80}Nb_4B_{13}Ge_2Cu_1$ alloys previously investigated, the objective lens current was set to 0.78% of maximum lens current, corresponding to an estimated lens field 156 Oe. The tilting series of phase images show that even in such a low applied field, the magnetic domain structures are significantly changed. The first and the

last image correspond to the two saturation states, since the magnetic flux is nearly forced along the external field directions and the magnetic domains structure disappeared. The total tilting angle between the two saturation states is only 10°, which is much smaller than the corresponding volume for $(Fe_{0.5}Co_{0.5})_{80}Nb_4B_{13}Ge_2Cu_1$ alloys heated at 550°C for 1 hour.

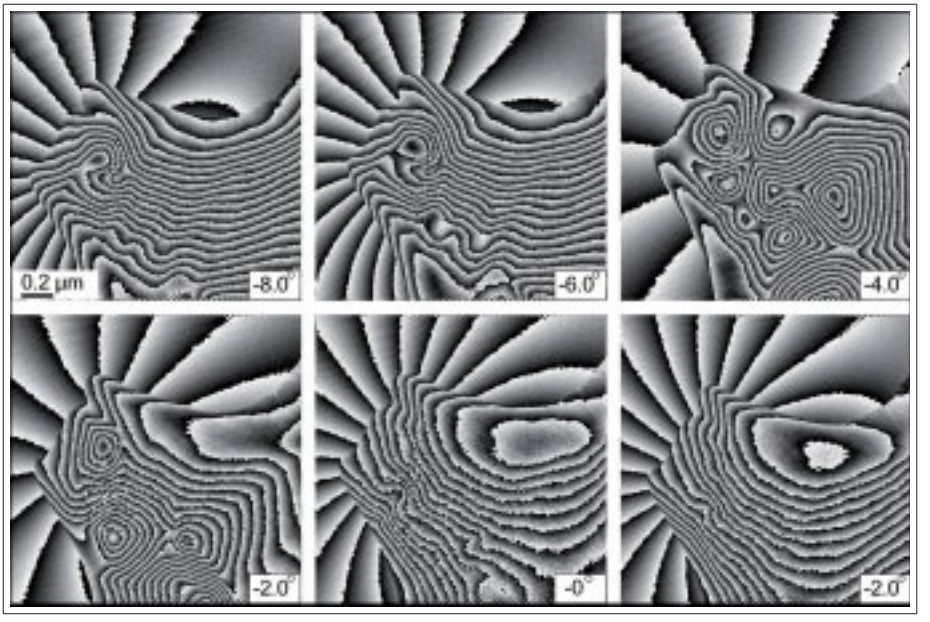

Figure 4.34. Tilting series of reconstructed phase images of $Fe_{79}Zr_6Si_{14}Cu_1$ nanocrystalline alloy heated at 450°C for 2 hour.

4.8 Summary

In this chapter we described the magnetic domain structures of FeCo-based nanocrystalline alloys by Lorentz microscopy and electron holography.

- Both Lorentz microscopy and electron holography indicate that the alloy heated at 500°C for one hour contains large magnetic domains (with size up to more than one micrometer) with few pinning sites. The magnetic flux distributions hint to low magneto-crystalline anisotropy.

The wall width of a typical 180° domain wall was measured to about 30 nm, which is in good agreement with a numerical evaluation.

- The Lorentz microscopy and electron holography investigations indicate the alloy heated at 550°C for one hour has a similar magnetic domain configuration as the sample heated at 500°C. The magnetic domain wall width was measured to about 40 nm. Additionally, the magnetic flux density of the sample was quantitatively determined to 1.0 T from electron holography phase image, in combination with the EELS-log ratio method for thickness determination. The dynamical magnetization observation indicates that the domain wall can easily move under week applied field.

- When the heating temperature was increased to 610°C for one hour, the size of the magnetic domains is significantly decreased. Each of the magnetic domains only contains two or three grains and the magnetic flux is disordered. The magnetic domain wall is strongly pinned by the grain boundary during the dynamical magnetization.

The microstructure characterization (chapter 3) and the magnetic domain structure investigation, the structure-property correlation in FeCo-based nanocrystalline alloys was obtained and well explained by the Herzer random anisotropy model. Additionally, the microstructure and magnetic domain structure of a new type Fe-based B-free soft magnetic alloy were investigated in this chapter.

Chapter 5

Reconstruction of 3D (Si,Ge) islands by 2D phase mapping

This chapter describes a 3D imaging of semiconductor (Si,Ge) islands grown on Si substrate by LPE growth. The surface morphology of (Si,Ge) islands was reconstructed from a 2D electron holography phase mapping. The reconstruction mechanism is based on the quantitative analysis of electron phase shift caused by the mean inner potential of the material. Two different models, the isolated atoms approximation and the bonding atoms model are used for the calculation of the mean inner potential during the reconstruction.

5.1 Introduction

5.1.1 Semiconductor nanostructures

During the last two decades, semiconductor nanostructures have attracted an increasing interest due to their high potential impact for both the fundamental research and the technical applications. In semiconductor nanostructures, artificial potentials for carriers, electrons, and holes are created at length scales comparable to the de Broglie wavelength or even smaller, lead to a significant quantum confinement effect [68]. The different densities of states (DOS) in 3D (bulk), 2D (film), 1D (wire) and 0D (dot) nanostructures are illustrated in Fig. 5.1 [69]. By using such kind of quantum

confinement effect, the restrictions due to bulk properties will be shifted or lifted. Then new devices could be developed with additional degrees of freedom in design. For example, in semiconductor quantum islands or quantum dots, three-dimensional quantum confinement gives rise to complete localization of electrons and holes and a discrete spectrum with δ-function-like density of states. This leads to novel device applications in microelectronic and opto-electronic devices [70].

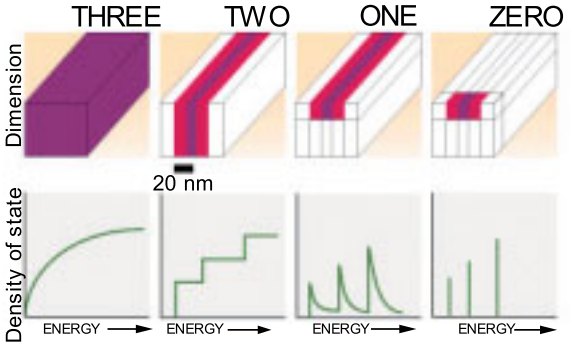

Figure 5.1. Densities of states (DOS) in quantum structures of different dimension [69].

5.1.2 (Si,Ge) semiconductor nanostructures

In this work we will investigate a particular semiconductor nanostructure consisting of 3D (Si,Ge) islands grown on (001) Si substrate. Both the silicon and germanium crystal have diamond structure, which consists of two sets of face-centered-cubic (fcc) lattices shifted at a quarter (1/4, 1/4, 1/4) along the space diagonal [1, 1, 1]. The lattice parameter of Si and Ge are 5.431 Å and 5.526 Å, respectively. They can completely miscible form a solid solution of $Si_{1-x}Ge_x$ alloys with a fixed crystal structure over the entire compositional range of $0 \leq x \leq 1$ [71]. Due to the wide range of variable crystal lattices and energy band-gaps, the (Si,Ge) alloy system provides a large opportunity for the application of electronic and photonics devices. Moreover, the induced strain in (Si,Ge) heterostructures due to the lattice mismatch can further modify the band structure, and provide new possibilities for energy band

engineering [72]. The (Si,Ge) nanostructures are particular attractive for monolithic integration of Si-based photonic and high-speed electronic devices with state-of-the-art CMOS chips [71].

5.1.3 Growth of 3D (Si,Ge) islands on Si substrate

The nanosized (Si,Ge) islands were grown on (001) oriented Si substrates by liquid phase epitaxy (LPE). Due to the large misfit between the substrate and the epitaxial layer, the growth occurs via a coherent Stranski-Krastanow (dislocation free) mode [73]. In this growth mode, at first a two dimensional wetting layer is formed on the surface of the substrate. With continuous growing of the wetting layer, the strain energy will also be increased. After reaching a critical thickness, the strain will be relaxed by forming a structure consisting of three-dimensional coherent islands.

Compared with other epitaxy techniques such as molecular beam epitaxy (MBE) and chemical vapor deposition (CVD), LPE growth occurs at nearly thermodynamic-equilibrium conditions [74]. During the growth of (Si,Ge) islands on (001) oriented Si substrate, Bismuth was selected as solvent. This advantageous is because at temperatures of 500°C-600°C, the solubility of Si and Ge in bismuth is very low. Then it is possible to get a precise control of supersaturation at low cooling rates and this leading to low growth rates. Another advantage is that the low surface energy can promote three-dimensional island growth rather than two-dimensional layer growth [74].

The whole growth process was performed under a pure hydrogen atmosphere to ensure a high purity of the epitaxial layer. The solute was saturated at two steps. In the first step the appropriate amount of Ge was dissolved and in the second step the solute was saturated with Si. Then the solution is homogenized at the growth temperature of 600°C for several hours. After that the sample A was cooled down to 590°C with 0.25 K/min, and the sample B was cooled with a cooling rate of 0.5 K/min.

5.2 Principle of 3D imaging by 2D phase mapping

5.2.1 CTEM limitations for 3D imaging

In order to get a better understanding of the structure-property correlations as well as the growth mechanism of the generated nanostructures, it is very important to obtain a 3D imaging of semiconductor nanostructures with high spatial resolution. TEM is a unique tool to study structure, composition and strain distribution in such kind of systems with high lateral resolution even at the atomic level of magnitude. Different from scanning probe techniques (SPM) such as atomic force microscopy (AFM) or scanning tunneling microscopy (STM), conventional TEM images normally provide only a 2D projection information of 3D nanostructures along the electron beam direction, as illustrated in Fig. 5.2. This is due to the fact that the high energy electrons transmit through the whole specimen but as a consequence of the projection theorem only a 2D electron intensity (amplitude) distribution in the exit plane of the specimen is recorded in the image plane. Due to the complex interaction between the incident electrons and the specimen such as described by the dynamical n-beam diffraction, it is difficult to extract quantitatively the thickness (height) information from the 2D electron intensity distribution. There exist, of course, various methods for the determination of the specimen thickness in TEM.

One of the commonly applied methods is using the convergent beam electron diffraction (CBED) technique. After recording the two beam case CBED pattern which satisfies the Bragg diffraction conditions, the thickness of the sample can be extracted from the positions of a series of fringes inside of the CBED disc [75]. These intensity oscillations are called Kossel-Möllenstedt fringes which are normally located symmetrically about the center of the hkl disk. A detailed introduction to this CBED method is given by J. C. H. Spence and J.M. Zuo [75] as well as by David B. Williams and C. Barry Carter [40]. The advantage of the CBED method is the high accuracy for the thickness determination. A determined accuracy of about 2% has been

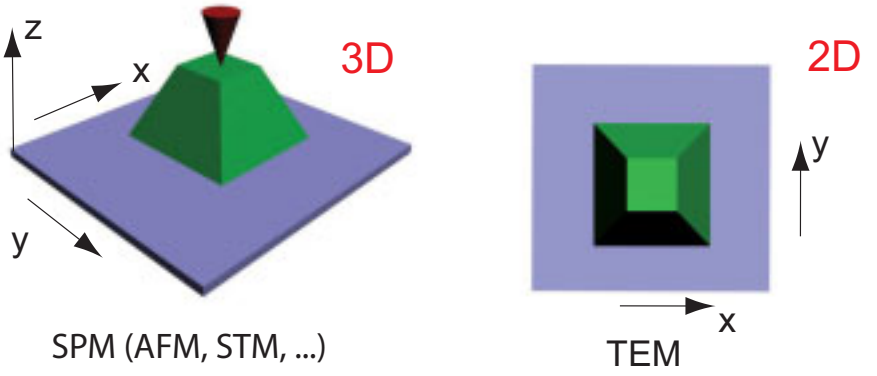

Figure 5.2. Sketch illustrating the imaging of nanostructures by SPM and TEM.

reported for a small unit cell crystal [75]. The disadvantage of the CBED method is that the method is only suitable for crystalline specimens. Additionally, the CBED method is not applicable to obtain a thickness mapping of a large area. This is due to the fact that during each measurement, the diffraction pattern associated with the thickness information is only coming from a small area illuminated by the convergent beam.

An alternative method using the electron energy loss spectrum (EELS) is the so-called EELS-log ratio method. This method has been used for the thickness determination of FeCo based nanocrystalline alloy specimens described in chapter 4. As we have already seen, the EELS-log ratio method can be applied to both crystalline and non-crystalline specimens. The method can be combined with an EELS line scan or spectrum imaging in the STEM mode to obtain a one-dimensional thickness profile or a two-dimensional thickness mapping. The disadvantage of this method is that the accuracy is not very high. This is mainly due to the lack of simple and efficient methods for the calculation of the mean free path length (MFP) of inelastically scattered electrons.

In this work, instead of using the electron intensity (amplitude) information, we successfully reconstructed the 3D (Si,Ge) islands nanostructures from a 2D phase mapping of electron holography.

5.2.2 Electron phase shift and mean inner potential

The basic principle of 3D imaging of semiconductor nanostructures by electron holography is based on the quantitative analysis of the electron phase shift caused by the mean inner potential of the investigated material. When high energy electrons transmit through the specimen, they will be scattered by the crystal potential which is generated by the positive nucleus and the negative electron charges in the crystal. Then the Schrödinger equation for incident electrons is written as

$$-\frac{\hbar^2}{2m}\Psi + V(r)\Psi = E\Psi, \tag{5.1}$$

where $\hbar$ is the reduced Planck constant, m is the electron mass, V(r) is the crystal potential and E is the electron energy depending on the accelerating voltage of the electrons. It has been reported if the electron energy is higher than 50 keV, the exchange between the electrons of the incident beam and the crystal electrons can be neglected [76]. Thus, the scattering potential is then only the electrostatic Coulomb potential. For crystalline specimens the Coulomb potential $V(\mathbf{r})$ is a three-dimensional periodic potential and can be expanded into Fourier series,

$$V(\mathbf{r}) = \sum_i V(\mathbf{g_i}) \exp\left(-2\pi \mathbf{g_i} \cdot \mathbf{r}\right) = V_0 + \sum_i {}' V(\mathbf{g_i}) \exp\left(-2\pi \mathbf{g_i} \cdot \mathbf{r}\right), \tag{5.2}$$

where $\mathbf{g_i}$ are the reciprocal lattice vectors. According to the Fourier transform theory, the first term V_0 is given by

$$V_0 = \frac{1}{\Omega_c} \int_{\Omega_c} V(\mathbf{r}) d\mathbf{r}, \tag{5.3}$$

where Ω_c is the crystal volume. We can recognize that V_0 is the average value of the whole crystal potential, which is normally called mean inner potential. Since the higher order terms reflect the periodical change of the Coulomb potential at atomic scale, then they can be neglected for electron holography applications at medium resolution.

If we neglect surface effects, the mean inner potential equals

$$V_0 = \frac{1}{\Omega}\int_{\Omega} V_{uc}(\mathbf{r})d\mathbf{r}, \tag{5.4}$$

where Ω is the volume of the unit cell, and $V_{uc}(r)$ is the electrostatic potential distribution within the unit cell.

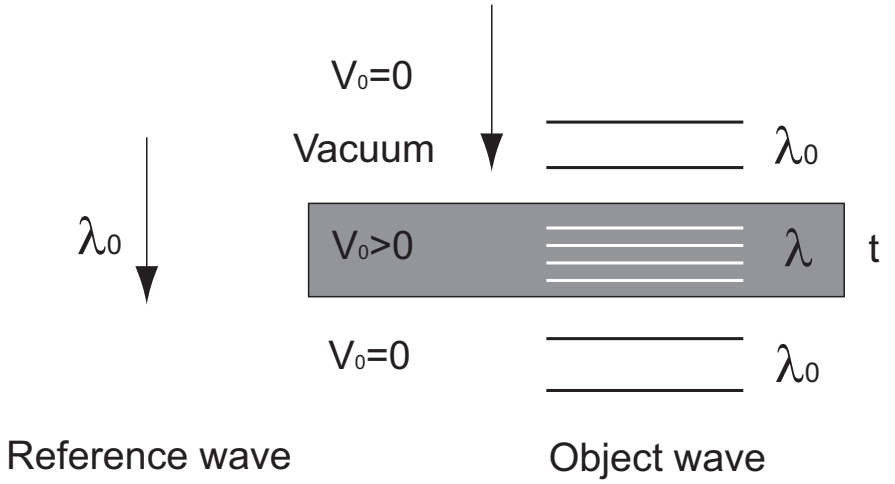

Figure 5.3. Illustration of electron phase shift due to the mean inner potential (adapted from [77]).

On the other hand, we consider electrons traveling in a homogeneous potential V_0. The incident beam is a plane wave and can be written as

$$\Psi(\mathbf{r}) = \exp(2\pi i\mathbf{k}\cdot\mathbf{r}) = \exp(2\pi k_z z), \tag{5.5}$$

where k_z is the electron wave vector in the vacuum (along the optical axis) depending on the accelerating voltage of the microscope. Considering the relativistic effect, the wave vector k_z in the vacuum is given by

$$k_z = \frac{1}{\lambda_0} = \frac{\sqrt{eV(2m_0c^2 + eV)}}{hc}, \tag{5.6}$$

where λ_0 is the electron wavelength in the vacuum, e is the electron charge,

V is the electron accelerating voltage, m_0 is the rest mass of the electron, c is the light velocity in the vacuum and h is the Planck constant.

When the electrons enter the specimen, the electron velocity will be slightly increased due to the attraction of the positive mean inner potential V_0. Then the wave vector in the specimen will be changed into [77]:

$$\begin{aligned} k = \frac{1}{\lambda} &= \frac{[(eV + eV_0)(2m_0c^2 + eV + eV_0)]^{1/2}}{hc} \\ &= \frac{[eV(2m_0c^2 + eV) + eV_0(2m_0c^2 + 2eV + eV_0)]^{1/2}}{hc} \\ &= k_z\{1 + \frac{eV_0(2m_0c^2 + 2eV + eV_0)}{eV(2m_0c^2 + eV)}\}^{1/2} \end{aligned} \tag{5.7}$$

The incident electron energy is about several hundreds kV, while the mean inner potential V_0 of most materials range from 5 to 30 V. Then after expanding Eq. 5.7, the higher order terms can be neglected, and only the first order term was to be taken into account [77],

$$k \approx k_z\{1 + \frac{eV_0(2m_0c^2 + 2eV}{eV(2m_0c^2 + eV)}\} + ... \tag{5.8}$$

Then the wave function Ψ in the specimen can be written as

$$\Psi \approx \exp(2\pi i k_z z) \exp(iC_E V_0 z), \tag{5.9}$$

where C_E is called electron interaction parameter. For this parameter yields:

$$C_E = \frac{2\pi}{\lambda V}(\frac{m_0c^2 + eV}{2m_0c^2 + eV}) \tag{5.10}$$

For 200 keV electrons, the parameter is given by $C_E = 0.00729\ V^{-1}nm^{-1}$. As illustrated in Fig. 5.3, when the electrons traveling through the specimen of thickness t_0, the phase shift ψ refered to the electrons propagating through the vacuum is given by

$$\psi_s \approx C_E V_0 t \tag{5.11}$$

Therefore, we can quantitatively calculate the thickness t from the phase

shift. It should be noted that when using this method, the object should be tilted away from the zone axis to avoid strong dynamical diffraction.

5.3 CTEM investigation of (Si,Ge) islands

Before describing the 3D imaging of (Si,Ge) islands by electron holography, we will discuss the conventional TEM experiments for the characterization of the morphology and structure of the islands.

Standard TEM plan-view samples were prepared by ion milling for both the CTEM and the electron holography investigations. In order to protect the (Si,Ge) islands from the ion beam, the ion milling was only performed from the side of the Si substrate.

5.3.1 Sample A

Figure 5.4 shows a typical BF-TEM plan-view image of sample A. Several (Si,Ge) islands deposited on the Si substrate are visible with dark contrast. The projection of the islands have a quadratic shape with a narrow size distribution. The average basal plane width ω was determined to 130 nm.

The inserted SAED image at the upper right of Fig. 5.4a was taken from a large area covered by several islands. The SAED pattern corresponds to the Si structure for [001] zone axis orientation. Though the electrons passed through both the islands and the Si substrate, only one set of electron diffraction pattern is visible. This indicates that the islands have a good epitaxial orientation and a very small lattice mismatch with the Si substrate. Furthermore, the different (Si,Ge) islands also have the same crystallographic orientations. The vertical growth direction of the islands is along the [001] direction, while the four basal edges are parallel to the [110] directions.

A more interesting phenomenon is that there is a high degree of coherence between the different islands. Not only the island orientations are identical, but also the positions of the islands are well aligned, as shown in Fig. 5.4. By comparing the BF image with the SAED pattern, it can be recognized that the islands are aligned along the Si substrate [100] direction. This ordered

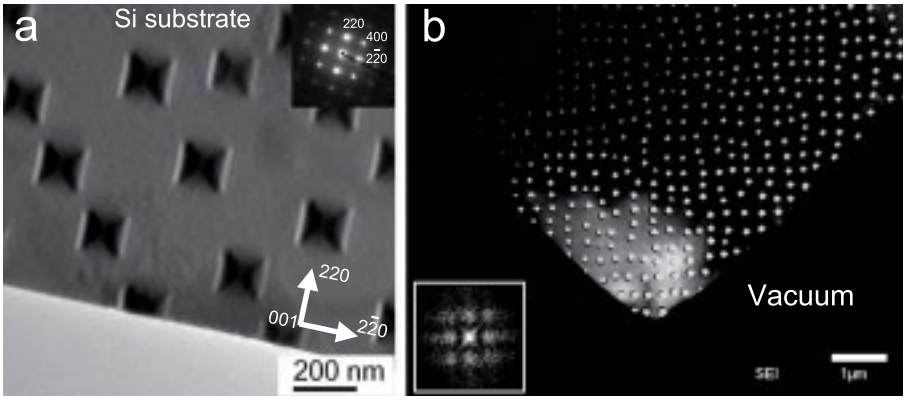

Figure 5.4. Plan-view TEM and STEM images of (Si,Ge) islands grown on (001) Si substrate with average basal plane width of 130 nm. (a) BF-TEM image. Inserted: SAED pattern. (b) STEM-HAADF image. Fourier transform power spectrum from a quadratic part of the HAADF image inserted at lower left. It indicates that the islands are two-dimensionally ordered.

structure can be more easily observed from the STEM-HAADF image in Fig. 5.4b which has a larger field of view. In the HAADF image the (Si,Ge) islands show bright contrast. A Fourier transform power spectrum (from a quadratic region of the HAADF image) is inserted at the lower left of Fig. 5.4b. The discrete spots with four-fold symmetry in the power spectrum reveals that the islands are organized like a two-dimensional lattice consisting of islands.

This interesting self-organized ordered structure indicates that the islands growth occurs via the well-known coherent SK mode. It has been well explained by Dorsch et al. that in such kind of (Si,Ge)/Si heterostructure system, surface ripples are developed due to the elastic stress relaxation during the early growth stages [78]. The ripples has a defined wavelength and form a two-dimensional pattern aligned along the [100] directions. Subsequently the ripples transform into pseudomorphic islands during the further growth process. The islands proceed to grow in vertical direction with fixed island width to form an ordered island structure, as we have seen in the BF and HAADF images.

A higher magnification STEM-HAADF image of the (Si,Ge) islands is shown in Fig. 5.5. In the STEM-HAADF imaging mode, only incoherent

scattered electrons at larger angles are collected by the annular dark-field detector and the complex dynamical diffraction effect is avoided during the contrast formation. Then the signal intensity from the thick area is higher than that from the thin area. The intensity profile across an individual island is plotted in Fig. 5.5b. It qualitatively reveals the height variation from the edge to the center region. However, no quantitative thickness data can be retrieved from the intensity profile. It also should be noted that the flat top of the profile is actually due to the intensity saturation during the image recording.

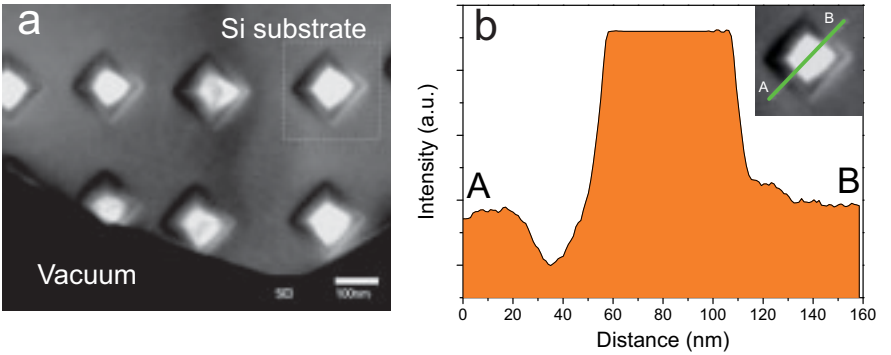

Figure 5.5. (a) High magnification STEM-HAADF image of (Si,Ge) islands grown on Si substrate (sample A). (b) Intensity line profile across an individual island.

5.3.2 Sample B

Figure 5.6 shows plan-view CTEM images and the corresponding electron diffraction pattern of an individual island in sample B. The BF and DF images in Fig. 5.6a and c were imaged with (000) and (220) beam, respectively. Both the BF and DF images indicate the island in sample B also has a quadratic shape. The basal plane width is now increased to about 350 nm, which is much larger compared with sample A. Obviously no dislocations were observed in the islands, which is consistent on the coherent SK growth mode. The SAED pattern in Fig. 5.6b again exhibits that the vertical growth

direction of the island is along the [001] direction of the substrate, and the basal edges are along the [110] directions.

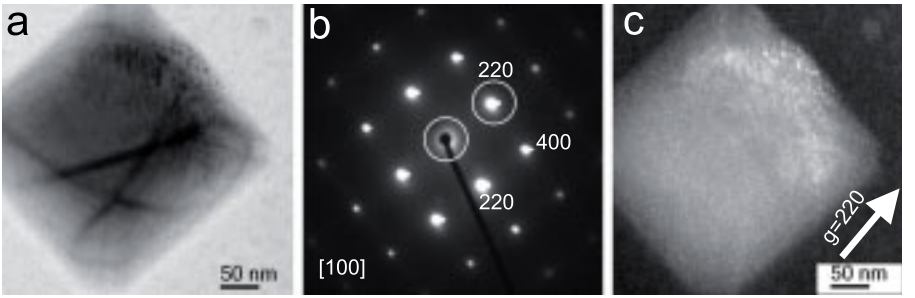

Figure 5.6. Plan view TEM images and SAED pattern of (Si,Ge) islands grown on (001) oriented Si substrate: (a) BF image; (b) SAED pattern and (c) DF image with (220) diffraction beam.

Evaluation of the chemical composition of the (Si,Ge) island

For the 3D imaging of (Si,Ge) islands from electron holography phase mapping, it is also necesseary to know the chemical composition of the islands since the materials mean inner potential also depends on the chemical composition. It has been reported that in the (Si,Ge)/Si LPE growth system, the islands basal plane width only scales with the Ge concentration and does not depend on the growth velocity and the growth temperature [79]. The dependence of the island basal plane width ω with the Ge concentration x can be approximately expressed as

$$\omega \approx 18.62\, x^{-2.01} \tag{5.12}$$

This equation was derived from the fitting of experimental AFM data [79]. The ω as a function of germanium content x was plotted in Fig. 5.7. For an island of a basal plane width $\omega = 130$ nm, the Ge concentration $x \approx 0.38$ and for basal plane width $\omega = 350$ nm, the Ge concentration $x \approx 0.23$.

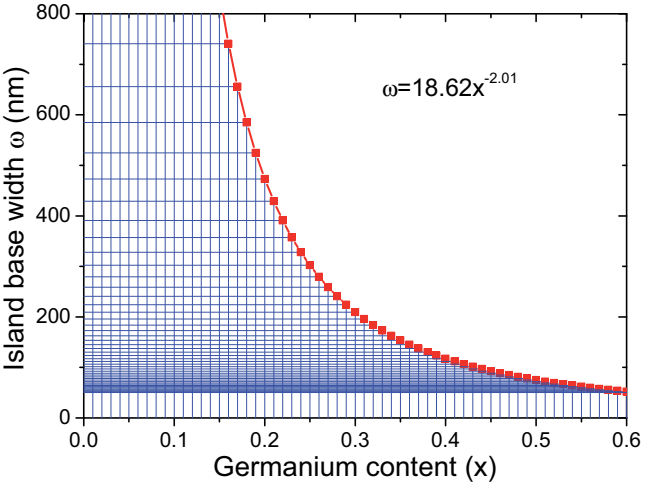

Figure 5.7. $Si_{1-x}Ge_x$ island base width as a function of Germanium composition.

5.4 Experimental phase mapping

For 3D imaging of (Si,Ge) islands, the experimental phase mapping by electron holography was applied. In order to get a large field of view, the electron holography was carried out in Lorentz mode. Both of the two specimens were tilted about 3-5 degree from the [001] zone axis to avoid any strong diffraction excitation.

5.4.1 Sample A

Figure 5.8a, b and c show the electron hologram, the reconstructed amplitude and phase images of the sample A, respectively. From the electron hologram it can be seen that several tens of the islands are covered by the biprism shadow, which contains a set of fine fringes. The vacuum area at the bottom of the image was used for the transmission of the reference wave. A selected part of the hologram from an individual island region (marked by the white frame) was magnified and inserted at the upper left of Fig. 5.8. The brightness of the inserted image has been slightly adjusted for a better visualization of the fringes. From the enlarged hologram it can be clearly seen that the

fringe spacings are strongly changed across the island, which indicates the large phase shift of the electrons due to the thickness variation. The reconstructed amplitude image is shown in Fig. 5.8b. It looks like a conventional BF-TEM image, no special interesting features are visible. Fig. 5.8c shows the corresponding unwrapped phase image. The bright contrast between the islands and the substrate depicts the large phase difference between them.

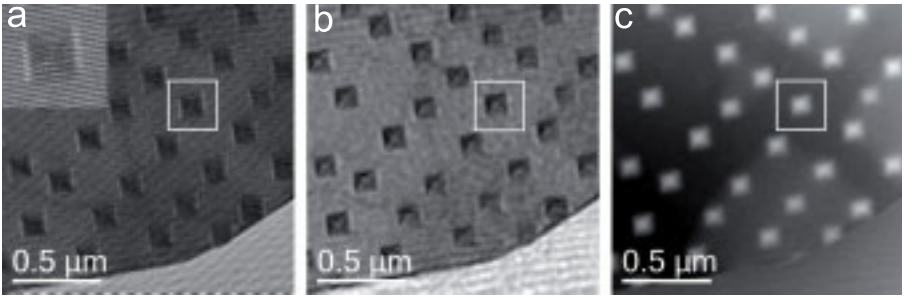

Figure 5.8. (a) Electron hologram, (b) reconstructed amplitude image and (c) reconstructed unwrapped phase image of (Si,Ge) islands (average basal plane width $\omega = 130\ nm$) grown on (001) orientated Si substrate.

5.4.2 Sample B

Figure 5.9 a, b, c and d show the electron hologram, the reconstructed amplitude, the raw phase as well as the unwrapped phase images of sample B, respectively. In the raw phase image in Fig. 5.9b large contour lines with a phase spacing of 2π are visible. This indicates the large phase shift across the island.

The line profiles extracted from the corresponding amplitude and phase image of an individual island are compared in Fig. 5.10a and b. An indication for the cross-section of the island parallel to the growth direction could be recognized from the phase profile. Contrary to that, the amplitude oscillates along the line scan.

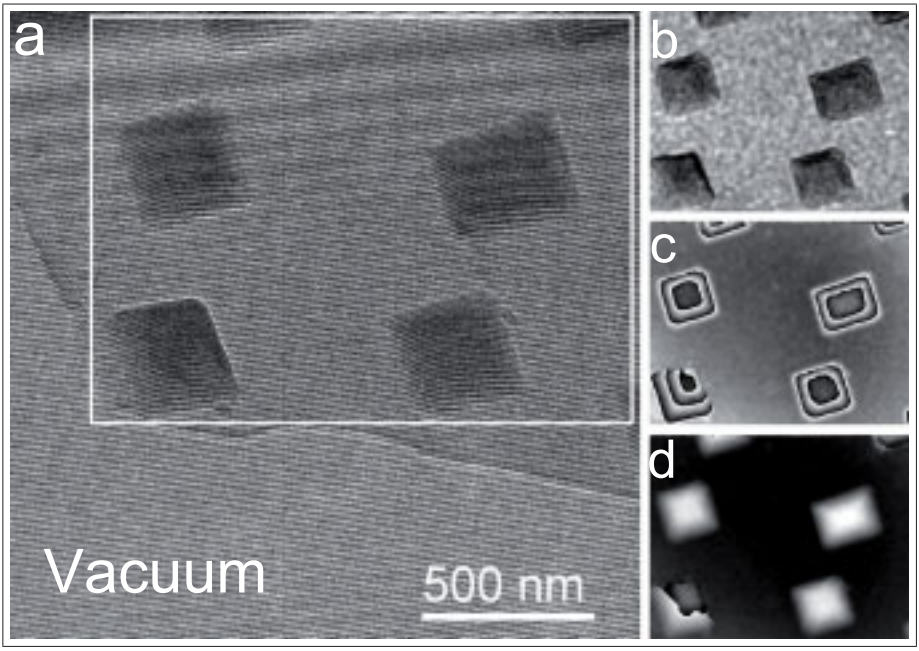

Figure 5.9. (Si,Ge) islands (a) hologram and (b) reconstructed amplitude, (c) raw phase and (d) unwrapped phase of the islands (basal plane width ω=350 nm) grown on (001) Si substrate.

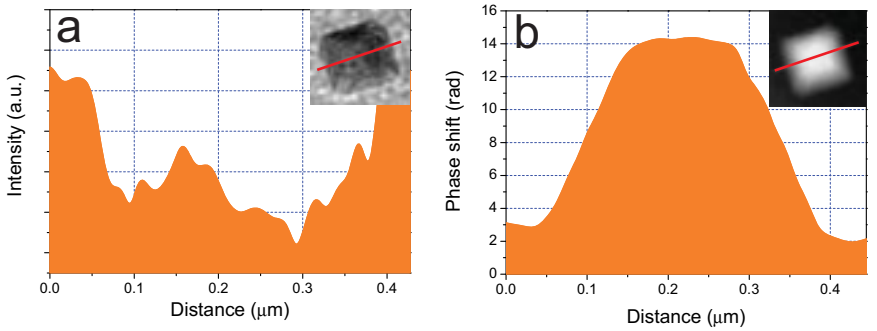

Figure 5.10. (a) Amplitude line profile and (b) the corresponding phase line profile of (Si,Ge) islands (basal plane width ω=350 nm) grown on (001) Si substrate.

5.4.3 Phase image processing

Before carrying out the reconstruction procedure, the phase images were further processed by means of digital image processing to subtract the mean inner potential contributions from the Si substrate. As illustrated in Fig. 5.11, the recorded electron phase shift in the island region (with respect to the vacuum) contains contributions of both the island and the substrate mean inner potential contributions. Particularly, the substrate has a wedged-shape due to the TEM sample preparation with ion milling. Therefore the phase shift contributions from the substrate are not uniform.

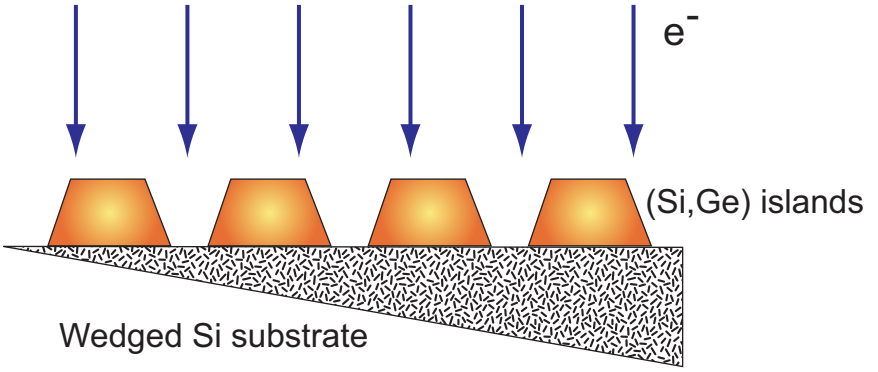

Figure 5.11. Schematic illustration of (Si,Ge) islands on a wedged-shape Si substrate.

The phase processing was performed with a standard SPM data analysis and processing software Gwyddion [80]. In order to keep the high precision, the original phase images reconstructed by Gatan Digital micrograph software were directly output as a text data file instead of any image formats. Then the phase data were imported into Gwyddion for further data manipulation. Since the substrate contributions are varied with the changing thickness, a polynomial fitting was used for subtracting the substrate contributions to the total phase shift. The fitted polynomial is given by

$$\sum_{j=0}^{m}\sum_{k=0}^{n} a_{j,k} x^j k^j, \tag{5.13}$$

where m and n are the selected horizontal and vertical polynomial degrees, respectively. The resulting data which only contain the phase shift contribution from the islands were output for surface morphology reconstruction. The phase images (sample A) before and after the digital image processing are compared in Fig. 5.12. The line profiles clearly show the non-uniform substrate contributions have been removed while the phase shift from the island is kept.

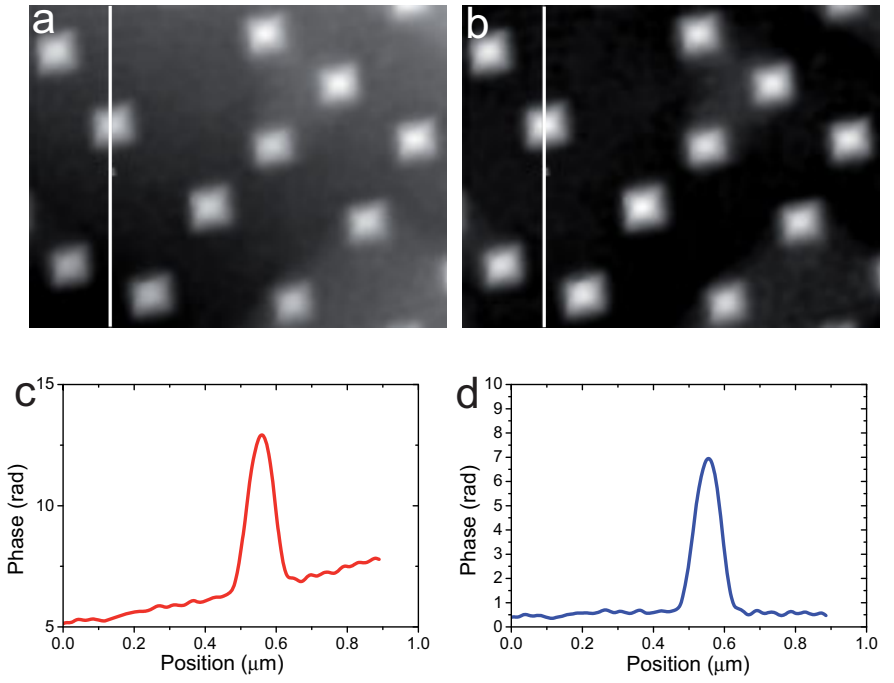

Figure 5.12. Phase images of (Si,Ge) islands before (a) and after (b) substrate subtraction. (c) and (d): The corresponding phase line profiles.

5.5 Mean inner potential calculation

In order to transform the experimental phase data to thickness mapping, according to Eq. 5.11, it is necessary to calculate the mean inner potential of

(Si,Ge) alloys. In this section two different models, the isolated atom model and the bonding model will be used for the calculation of the mean inner potential.

5.5.1 Isolated atoms model

First we will calculate the mean inner potential of the (Si,Ge) alloys within the isolated atom model. This means the bonds between the atoms in a real crystal are neglected, and then the crystal potential can be considered as a superposition of the individual atomic potentials. Though the electron density and the distributions of the electrostatic potential in a real crystal are slightly different from isolated atom model, it is still widely used for the interpretation and the simulation of TEM images. The atom potential is normally expressed by atomic scattering factors. The relationship between the atom potential and the atom scattering factor for high energy electrons have been introduced in detail by B. Fultz and J. M. Howe as following [81].

Atomic scattering factor and atomic potential

The Schrödinger equation for electron scattering by an individual atom is written as

$$-\frac{\hbar^2}{2m}\bigtriangledown^2\Psi(\mathbf{r}')+V(\mathbf{r}')\Psi(\mathbf{r}')=E\Psi(\mathbf{r}'), \tag{5.14}$$

where Ψ is the electron wave function, $\hbar$ is the reduced Planck constant, m is the electron mass, V(r′) is the atomic potential and E is the electron energy. In TEM the incident electrons are plane waves

$$\Psi_{inc}=e^{i\mathbf{k_0}\cdot\mathbf{r}} \tag{5.15}$$

The scattered wave takes on then the form

$$\Psi_{scatt}=f(\mathbf{k_0},\mathbf{k})\frac{e^{i|\mathrm{r}-\mathrm{r}'|}}{|\mathrm{r}-\mathrm{r}'|}, \tag{5.16}$$

where $f(\mathbf{k_0},\mathbf{k})$ is defined as the atomic scattering factor [81]. Both the incident wave and the scattered wave are illustrated in Fig. 5.13. By using

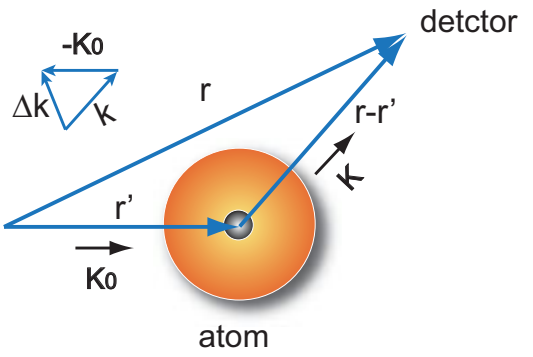

Figure 5.13. Electron scattering by atom potential. Adapted from Ref. [81].

the Green function G(r)

$$G(\mathbf{r},\mathbf{r}') = -\frac{1}{4\pi}\frac{e^{ik|\mathbf{r}-\mathbf{r}'|}}{|\mathbf{r}-\mathbf{r}'|} \tag{5.17}$$

which satisfies

$$(\bigtriangledown^2 + k_0^2)G(\mathbf{r},\mathbf{r}') = \delta(\mathbf{r}'), \tag{5.18}$$

The differential equation is transformed into an integral equation (see Ref. [81]). Then the total wave is given by

$$\Psi(r) = \Psi_{inc} + \Psi_{scatt} \tag{5.19}$$

$$\Psi(r) = e^{i\mathbf{k_0}\cdot\mathbf{r}} + \frac{2m}{\hbar^2}\int U(\mathbf{r}')\Psi(\mathbf{r}')G(\mathbf{r},\mathbf{r}')d^3\mathbf{r}' \tag{5.20}$$

where

$$U(\mathbf{r}') = \frac{2mV(\mathbf{r}')}{\hbar^2} \tag{5.21}$$

Equation 5.20 is the exact solution for the scattering problem of Eq. 5.14. However the unsolved problem is the unknown wave $\Psi(r)$ which is located on both sides of Eq. 5.20. An approximation is necessary for further proceeding [81]. Here the first Born approximation is applied, which means the wave function $\Psi(r')$ in the right side of Eq. 5.20 is replaced by the incident plane wave

$$\Psi(\mathbf{r}') \approx e^{i\mathbf{k_0}\cdot\mathbf{r}'} \tag{5.22}$$

The first Born approximation assumes that the scattering is week, so the electrons are only scattered once. For high energy electron scattering by an individual atom, this condition can be satisfied. If the detector is far from the scatterer, the equation could be further simplified. In this situation the Green function can be rewritten as

$$G(\mathbf{r},\mathbf{r}') \backsimeq -\frac{1}{4\pi}\frac{e^{i\mathbf{k}\cdot(\mathbf{r}-\mathbf{r}')}}{|\mathbf{r}|} \tag{5.23}$$

After inserting Eqs. 5.22 and 5.23 into Eq. 5.20, we will get

$$\Psi(r) = e^{i\mathbf{k_0}\cdot\mathbf{r}} - \frac{m}{2\pi\hbar^2}\frac{e^{i\mathbf{k}\cdot\mathbf{r}}}{|\mathbf{r}|}\int V(\mathbf{r}')e^{-i\mathbf{\Delta k}\cdot\mathbf{r}}d^3\mathbf{r}' \tag{5.24}$$

Where $\mathbf{\Delta k}$ is defined as

$$\mathbf{\Delta k} = \mathbf{k} - \mathbf{k_0}, \tag{5.25}$$

and the scattering wave is

$$\Psi_{scatt}(\mathbf{\Delta k},\mathbf{r}) = \frac{e^{i\mathbf{k}\cdot\mathbf{r}}}{|\mathbf{r}|}f(\mathbf{\Delta k}), \tag{5.26}$$

where

$$f(\mathbf{\Delta k}) \equiv -\frac{m}{2\pi\hbar^2}\int V(\mathbf{r}')e^{-i\mathbf{\Delta k}\cdot\mathbf{r}}d^3\mathbf{r}' \tag{5.27}$$

Thus within the first Born approximation, the scattering wave is proportional to the Fourier transform of the scattering potential [81].

Particularly, the atomic scattering factor in forward direction ($\Delta k = 0$) is given by

$$f(0) = -\frac{m}{2\pi\hbar^2}\int V(\mathbf{r}')d^3\mathbf{r}' \tag{5.28}$$

From here we can recognize that the right part contains the total atomic potential.

Structure factor and mean inner potential

Similarly, we can replace the atom potential $V(\mathbf{r}')$ in Eq. 5.27 by the electrostatic potential distribution $V_{uc}(\mathbf{r}')$ inside the unit cell of a crystal. Then we will get the electron scattering from the unit cell. The first Born approximation conditions are still satisfied here. (It should be noted that, we can not directly replace $V(\mathbf{r}')$ in Eq. 5.27 by the whole crystal potential of a thick crystal. Otherwise the first Born approximation conditions can not be satisfied, since multiple scattering will occur and dynamical diffraction effects have to be included.) Then the electron scattering structure factor is given by

$$F(\mathbf{\Delta k}) \equiv -\frac{m}{2\pi\hbar^2}\int V_{uc}(\mathbf{r}')e^{-i\mathbf{\Delta k}\cdot\mathbf{r}}d^3\mathbf{r}' \tag{5.29}$$

The structure factor in forward direction ($\mathbf{\Delta k} = 0$) is given by

$$F(0) = -\frac{m}{2\pi\hbar^2}\int V_{uc}(\mathbf{r}')d^3\mathbf{r}' \tag{5.30}$$

Comparing with Eq. 5.4, we will find that the crystal mean inner potential V_0 is given by

$$V_0 = \frac{\int V_{uc}(\mathbf{r}')d^3\mathbf{r}'}{\Omega} = -\frac{2\pi\hbar^2}{m\Omega}F(0), \tag{5.31}$$

where Ω is the volume of the unit cell.

From here we can conclude that the structure factor for high energy electron scattering in forward direction is proportional to the mean inner potential of the crystal.

For the isolated atoms model, the electrostatic potential inside the unit cell can be considered as the superposition of the isolated atomic potential. Then the structure factor is given by

$$F(\mathbf{\Delta k}) = \sum_j f_j(\mathbf{\Delta k})e^{-i\mathbf{\Delta k}\cdot\mathbf{r_j}} \tag{5.32}$$

where $f_j(0)$ is the atomic scattering factor of the j atom inside the unit cell.

In forward direction $\mathbf{\Delta k} = 0$

$$F(0) = \sum_j f_j(0), \tag{5.33}$$

$f_j(0)$ is the atomic scattering factor of the j atom inside the unit cell in forward direction. The mean inner potential is then given by

$$V_0 = -\frac{2\pi\hbar^2}{m\Omega}\sum_j f_j(0) \tag{5.34}$$

Conventionally, the mean inner potential is given in unit volt instead of electron volt, then Eq. 5.34 is written as

$$V_0 = -\frac{2\pi\hbar^2}{me\Omega}F(0) = -\frac{2\pi\hbar^2}{me\Omega}\sum_j f_j(0) \tag{5.35}$$

Si and Ge atomic scattering factors

The atomic scattering factor $f(\Delta\mathbf{k})$ for high energy electrons can be either deduced from the X-ray scattering factor f_x using the Mott formula, or can be directly calculated from the electronic structure.

When deducing from the X-ray scattering factor, the Mott formula is given by

$$f(\Delta\mathbf{k}) = \frac{2me^2}{\hbar^2\Delta k^2}\{Z - \frac{mc^2}{e^2}f_x(\Delta\mathbf{k})\} \tag{5.36}$$

where Z is the atomic number for a particular atom and c is the velocity of light in vacuum [81]. The Mott formula is based on the fact that the X-ray scattering factor f_x is proportional to the Fourier transform of the electron density distribution $\rho(\mathbf{r}')$ in the atom, where

$$f_x(\mathbf{\Delta k}) = -\frac{e^2}{mc^2}\int \rho(\mathbf{r}')e^{-i\mathbf{\Delta k}\cdot\mathbf{r}}d^3\mathbf{r}' \tag{5.37}$$

The atom potential distribution V(r') is connected with atom charge dis-

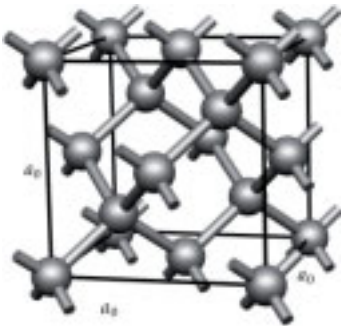

Figure 5.14. Diamond structure of (Si,Ge) alloys [82].

tribution via the Poisson equation

$$\nabla^2 V(r') = -(Z - \rho(\mathbf{r}')), \tag{5.38}$$

where Z is the nuclear charge.

The atomic scattering factor also have been directly calculated by Doyle and Turner using the relativistic Hartree-Fock atomic wave functions [83]. For Si with atomic number 14, the calculated value $f_{\mathrm{Si}}(0) = 5.828$ Å, and for Ge with atomic number 32, $f_{\mathrm{Ge}}(0) = 7.378$ Å.

Structure factor of (Si,Ge) alloys in forward direction

(Si,Ge) alloys crystallises in the diamond structure with space group $Fd\bar{3}m$. The diamond structure consists of two sets of face-centered-cubic (fcc) lattices displaced at (1/4, 1/4, 1/4) along the space diagonal. The diamond structure is illustrated in Fig. 5.14. It can be seen that eight atoms located at the corner contribute ($8 \times (1/8) = 1$ atom) to the unit cell, 6 face-centered atoms contribute ($6 \times (1/2) = 3$) atoms, and 4 inner atoms contribute as a whole, so totally in one unit cell there are eight atoms. Then for $(\mathrm{Si}_{1-\mathrm{x}}, \mathrm{Ge}_{\mathrm{x}})$ alloys,

$$\sum_j \mathrm{f_j}(0) = 8 \times \{\mathrm{f_{si}}(0)(1-x) + \mathrm{f_{Ge}}(0)x\} \tag{5.39}$$

After substituting $f_{\mathrm{Si}}(0) = 5.828$ Å and $f_{\mathrm{Ge}}(0) = 7.378$ Å into Eq. 5.39, we will get

$$\sum_j \mathrm{f_j}(0) = 8 \times \{5.828(1-x) + 7.378x\} \text{ Å} \tag{5.40}$$

Unit cell volume

As shown in Eq. 5.35 the mean inner potential also depends on the unit cell volume Ω. For diamond structure, the unit cell volume Ω is given by

$$\Omega = a^3, \tag{5.41}$$

where a is the lattice constant. For $\mathrm{Si_{1-x}Ge_x}$ alloys, the lattice constant a is changed with the Ge concentration. Then a is given by (Ref. [84])

$$a(x) = 5.431 + 0.20x + 0.027x^2 \text{ (Å)} \tag{5.42}$$

The lattice constant of $\mathrm{Si_{1-x}Ge_x}$ alloys as a function of the Ge concentration is plotted in Fig. 5.15.

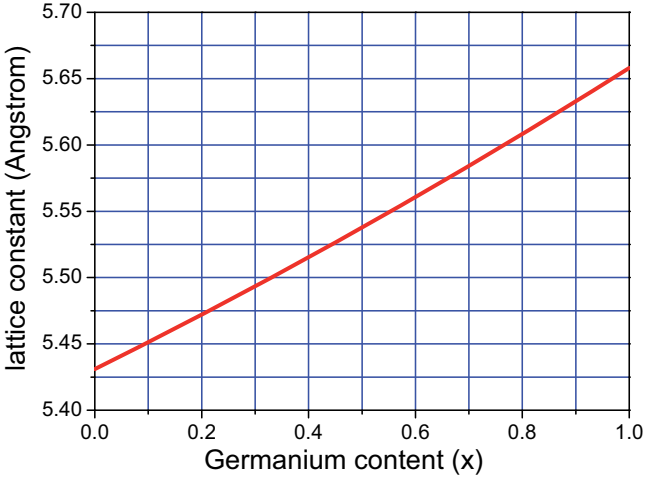

Figure 5.15. Lattice constant a of $\mathrm{Si_{1-x}Ge_x}$ alloys as a function of the germanium composition.

Mean inner potential of $Si_{1-x}Ge_x$ alloys using the isolated atom model

By substituting the structure factor in forward direction and the unit cell volume into Eq. 5.35, we get the mean inner potential of the $Si_{1-x}Ge_x$ alloys as a function of Ge concentration, as shown in Fig. 5.16. It should be noted that in general for TEM applications, the atomic scattering factors calculated by Doyle and Turner [83] need to be multiplied by $m/m_0 = [1 - (v/c)^2]^{-1/2}$, where v is the velocity of electrons in TEM [15]. However, for mean inner potential calculation, if the electron mass m in Eq. 5.35 still takes the rest mass m_0, the scattering factor correction will be omitted.

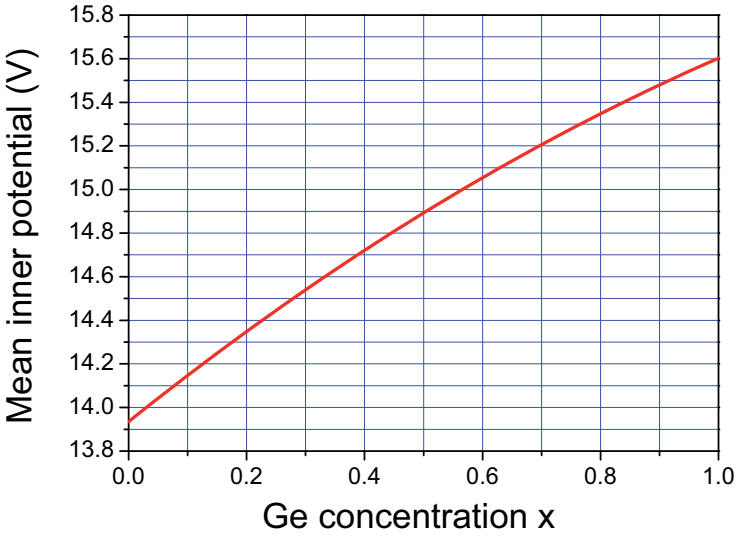

Figure 5.16. Mean inner potential of $Si_{1-x}Ge_x$ alloys as a function of the germanium composition using the isolated atom model calculation.

5.5.2 Mean inner potential using the bonding model

The isolated atoms approximation (considering the electron scattering by means of atomic scattering factors) is very simple and has been widely used in most of the TEM analysis. But it is not precise for the interpretation of

the phase shift of electrons due to the mean inner potential of the material to be investigated. This is due to the fact that when isolated atoms form a crystal, the electron density as well as the electrostatic potential distributions around the atoms will be slightly modified due to the bonding between the atoms. The redistributions of electron density and electrostatic potential mostly happen in the shell part of the atoms, but less in the core part.

In TEM, such bonding effects mainly affect the electron scattering in forward direction or near forward direction, but much less at large angle scattering like the Bragg angle scattering. This is because the large angle scattering is mostly due to the scattering at the core of the atoms. Then the bonding effects can be neglected when interpretating diffraction contrast images or STEM-HAADF images.

In medium resolution electron holography, the detected electron phase shift is connected with the mean inner potential of the material. As we have already explained, the structure factor in forward direction is proportional to such a mean inner potential. This means that the phase shift which we detected corresponds to forward scattered electrons and then it is very sensitive to bonding effects. As already mentioned the isolated atom approximation is not precise enough. We have to recalculate the electrostatic potential distribution inside the unit cell. This is equal to a recalculation of the structure factor instead of simply superimposing the atomic scattering factors (with proper phase factor), as shown in Eq. 5.33.

The precise calculation of the electrostatic potential distribution in the unit cell of the crystal is a difficult many-body problem. This problem looks similar to high energy electron scattering by crystal potential. However, the difficulty here is we must consider the exchange and correlations between the electrons, while in high energy electron scattering, the exchange and correlations between beam electrons and crystal electrons can be neglected. Today a powerful solution for this problem is given by Density Functional Theory (DFT) calculations. After the ground state electron density is calculated, via Poisson equation, the electrostatic potential distribution in the crystal, as well as the mean inner potential will be calculated.

In general the DFT calculation can be performed in either pseudo-potential

method calculation or full electron calculation. But for high energy electron scattering, the scattering potential not only comes from the shell part of the atoms. But most contributions come from the scattering at the core part. Then the full electron calculation programme like the Wien 2K package have to be applied. It is difficult to calculate the electronic structure of the alloys with full electron DFT calculation. Thus, we estimate the mean inner potential of (Si,Ge) alloys by fitting the values of Si and Ge crystal which have been calculated by DFT. This kind of fitting includes the bonding effects between the Si atoms or the Ge atoms, but does not include the boding between Si and Ge atoms.

The Si and Ge crystal mean inner potential have been calculated as 12.57 V and 14.67 V by P. Kruse et. al (with Wien 2k DFT calculation) [85]. The fitted mean inner potential of (Si,Ge) alloys is plotted in Fig. 5.17. For $Si_{0.62}Ge_{0.38}$ alloys, the mean inner potential is 13.37 V. For $Si_{0.77}Ge_{0.23}$ alloys, the mean inner potential is decreased to 13.05 V.

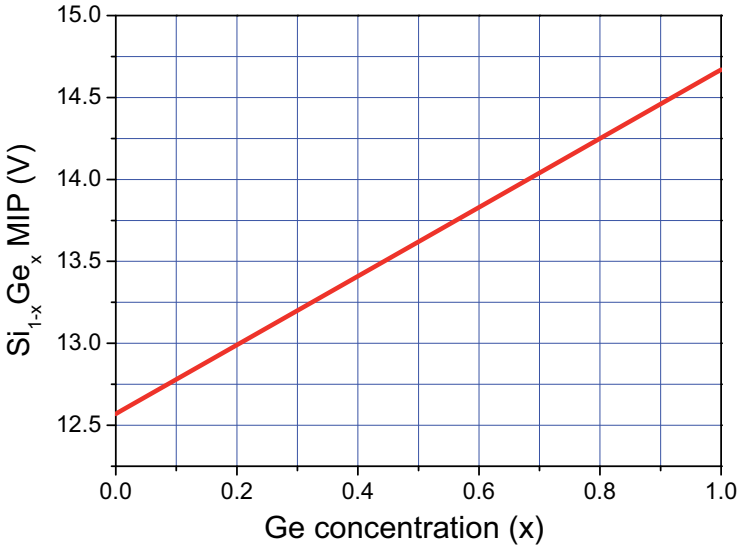

Figure 5.17. Mean inner potential of $Si_{1-x}Ge_x$ alloys as a function of the germanium conposition. (Fitted with the value of Si and Ge crystal calculated by means of DFT.)

Reconstruction of the (Si,Ge) islands

With the calculated mean inner potential, we transform the 2D phase mapping into the 3D images. The 3D imaging of $Si_{0.62}Ge_{0.38}$ islands grown on Si substrate is shown in Fig. 5.18. We can see that the islands have truncated pyramidal shape and the average height $h \approx 66\ nm$, and $h : \omega \approx 1 : 2$. The four side facets are calculated as (1,1,1) plane.

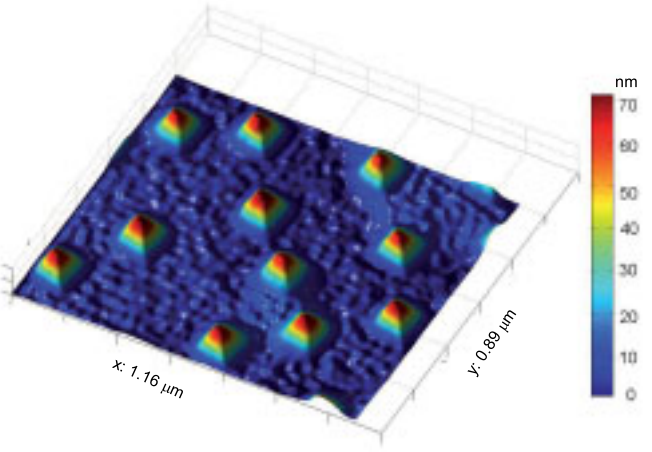

Figure 5.18. Reconstructed 3D $Si_{0.62}Ge_{0.38}$ islands grown on Si substrate from 2D phase mapping.

The 3D imaging of a $Si_{0.77}Ge_{0.23}$ island grown on Si substrate is shown in Fig. 5.19. The island clearly shows a truncated pyramidal shape. It can be seen that with the increasing lateral size of the islands to $\omega \approx 350\ nm$, the island height is also increased to $h \approx 130\ nm$. The island clearly shows a shape of a truncated pyramid with 111 side and a single (001) top facet.

5.6 Summary

In this chapter, we successfully reconstructed the 3D surface morphology of (Si,Ge) islands by a 2D electron holography phase mapping. The (Si,Ge)

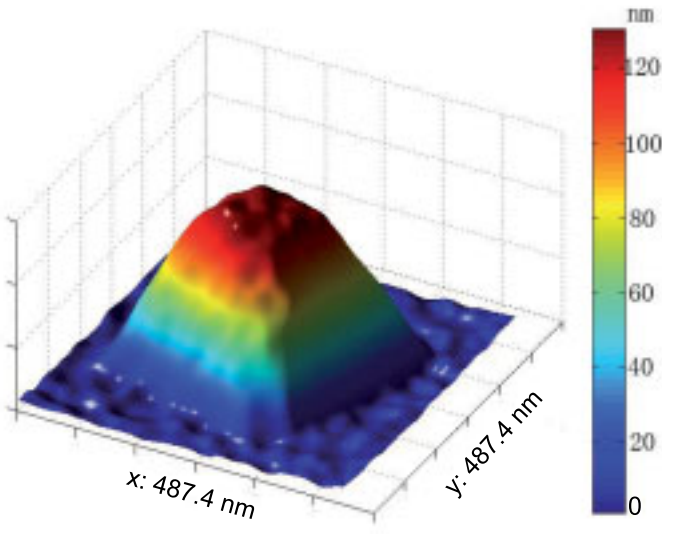

Figure 5.19. Reconstructed 3D $Si_{0.77}Ge_{0.23}$ island grown on Si substrate from 2D phase mapping.

islands were grown on (001) oriented Si substrate by LPE growth and prepared in TEM plan-view. Two specimens with different islands basal plane width were investigated.

Conventional TEM investigations(BF, DF) and STEM-HAADF indicate that the projection of the islands along the incident electron beam direction have a common quadratic shape. The basal plane width ω was measured to about 130 nm and 350 nm, respectively. SAED experiments proved that the islands have a good epitaxial orientation and a very small lattice mismatch with the Si substrate. Additionally, the islands show a self-assembled ordering structure, which proves that the growth of the islands takes in a dislocation free coherent SK mode. The alloys composition of the $Si_{1-x}Ge_x$ islands were estimated from the determined basal plane width to x=0.38 (ω=130 nm) and x=0.23 (ω=350 nm), respectively.

The experimental phase mapping were performed in Lorentz mode with a large field of view. Both of the phase images were unwrapped before recon-

struction to removing the phase jump. Further imaging processing incudes the Si substrate contribution with a polynomial fitting.

The mean inner potential was calculated using two different models. Using the isolated atom model, the mean inner potential is 14.69 V ($Si_{0.68}Ge_{0.32}$) and 14.41 V ($Si_{0.77}Ge_{0.23}$) respect, while for the bonding atoms model, the calculated mean inner potential is 13.37 V ($Si_{0.68}Ge_{0.32}$) and 13.05 V ($Si_{0.77}Ge_{0.23}$), respectively.

Finally, by using the calculated mean inner potential, the electron phase shift was transformed to height data and the (Si,Ge) islands were successfully reconstructed with a 3D visualization.

Chapter 6

Summary and outlook

6.1 Summary

This thesis is mainly focused on the investigation of magnetic materials and semiconductor nanostructures by means of off-axis electron holography. The basic principle is based upon the detection and analysis of the phase shift of electrons caused by the distribution of the electric and magnetic field in 3D space. Two different topics, the structure-property correlations in FeCo-based and Fe-based nanocrystalline soft magnetic alloys, and a 3D imaging of (Si,Ge) islands grown on (001) oriented Si substrate are involved in this work:

6.1.1 Nanocrystalline soft magnetic alloys

In the first topic, the correlation between structure and soft magnetic properties of FeCo-based and Fe-based nanocrystalline soft magnetic alloys were investigated. The alloys were fabricated by annealing amorphous ribbons at different temperatures.

First, the structure and chemical composition of FeCo-based nanocrystalline alloys were characterized by conventional TEM techniques, including BF- and DF- imaging, electron diffraction, HRTEM, STEM-HAADF and EDX analysis. The TEM results indicate that the alloys consist of an amorphous matrix with embedded nano-sized FeCo crystallites of random orien-

tation. The FeCo particles were proved to have bcc structure with a lattice parameter of 2.0 Å. Further analyses reveal that the size of the crystallites strongly depends on the annealing temperature during the crystallization. For lower heating temperature (1h at 500°C and 550°C), the average grain size of the crystallites is only about 12 nm and 18 nm, respectively. Contrary to that, most of the residual amorphous phase has been crystallized during annealing at 610°C for 1h. This leads to a dramatic increase of the grain size to about 90 nm. Additionally, a few crystallites of ($Fe_{23}B_6$) have been identified.

Second, the magnetic domain configurations of the FeCo-based nanocrystalline alloys were investigated and analyzed by electron holography and Lorentz microscopy. The results indicate that there is a strong correlation between the microstructure of the alloys and the structure of the magnetic domains:

1. For the alloys heated one hour at 500°C, both, electron holography and Lorentz microscopy images reveal that the alloy consists of magnetic domains with a size varying from several hundred nanometers to several micrometers. Very few pinning sites were formed. The configuration of the magnetic domains hints to good soft magnetic properties. Further, from the line profile of electron phase shift perpendicular to the domain wall, the width of the wall was measured to about 30 nm, which is much larger than the average size of the nanocrystallites (∼12 nm) mentioned above. The measured width of the domain wall is also in good agreement with a numerical simulation.

2. When the heating temperature was increased to 550°C, the alloy keeps the similar configuration of the magnetic domains (large magnetic domain size and few pinning sites). The width of the magnetic domain wall are about 40 nm as estimated from a focus series of Lorentz microscopy images. The result again indicates that for this heating temperature, the width of the domain wall is still much larger than the average FeCo grain size of about 18 nm. Additionally, the magnetic flux density of the alloy was quantitatively calculated to about 1.0 T from the phase gradient in correlation with the thickness determined by electron energy-loss spectroscopy.

3. For an annealing temperature of 610°C, the size of the magnetic domains is significantly decreased with the size of the crystalline grains ($\sim$ 90 nm). Each of the magnetic domains only comprises two or three nanocrystallites, while the magnetic domain walls are strongly pinned by the boundaries between the crystallites. The magnetic flux in the alloy is very complex and disordered, which hints to poor soft magnetic properties.

Third, the dynamical magnetization behavior of the alloys was observed in both the Lorentz microscopy and electron holography by tilting the specimen in a weakly excited objective lens field. The results indicate that the alloys heated at lower annealing temperature (550°C) can be easily magnetized and demagnetized in week applied field. A Barkhausen effect also was observed during the dynamical magnetization. Compared to that, the magnetic domain walls are strongly pinned by the grain boundaries in the alloys annealed at 610°C. This results in poor soft magnetic properties.

Finally, the observed correlation of the structure and magnetic properties correlation of the alloys was interpreted by the Schertz random anisotropy model. The results indicate that better soft magnetic properties can be obtained from alloys with smaller FeCo grains.

6.1.2 Semiconductor nanostructures

In the second topic, a 3D imaging of nanoscale (Si,Ge) islands was successfully derived from a 2D phase mapping of electron holograms. The (Si,Ge) islands were grown on (001) oriented Si substrate by LPE growth and prepared for plan-view TEM. Two specimens strongly differencing in the size of the islands were investigated.

First, the correlation between the electron phase shift, the mean inner potential and the specimen thickness was discussed in detail.

Second, the (Si,Ge) island structure was characterized by conventional plan-view TEM. The results clearly show that in both specimens, the projection of the islands is quadratic. The basal plane width ω was measured to be about 130 nm and 350 nm, respectively. Electron diffraction experiments further proved that the islands have identical azimuthal orientation and a

very small lattice mismatch with the Si substrate. Particularly, the islands show a high degree of lateral ordering , which reveals that the growth of the islands takes in coherent SK mode. The composition of the $Si_{1-x}Ge_x$ islands was also calculated from the determined basal plane width to x=0.38 (ω=130 nm) and x=0.23 (ω=350 nm), respectively.

Third, the electron holography experiments were carried out in Lorentz mode with a large field of view. After the reconstruction of the phase images from the electron holograms, the contribution of the Si substrate to the electron phase shift was subtracted with a polynomial fitting.

Fourth, the mean inner potential of $Si_{1-x}Ge_x$ alloys was calculated by two different methods. The model assuming isolated atoms revealed a mean inner potential of 14.69 V ($Si_{0.68}Ge_{0.32}$) and 14.41 V ($Si_{0.77}Ge_{0.23}$) respectively. On the contray, the model including atomic bonds delivered the mean inner potentials of 13.37 V ($Si_{0.68}Ge_{0.32}$) and 13.05 V ($Si_{0.77}Ge_{0.23}$), respectively.

Finally, by using the calculated mean inner potential, the electron phase shift was transformed to height data and the (Si,Ge) islands were successfully reconstructed with a 3D visualization.

6.2 Outlook and further suggestions

Based on the work in this thesis, some suggestions for forthcoming studies are summarized.

1. High-resolution imaging of magnetic structures by electron holography

High-resolution magnetic imaging is very attractive for magnetic materials research in order to interpret the correlations between magnetism and structure at atomic scale. One example is to study the structure-property correlations in spin electronic devices. In order to keep the specimen in natural magnetization, magnetic imaging by electron holography should be carried out in Lorentz mode (the main objective lens should be switched off and the electrons are focused by an objective mini lens). Due to the poor resolu-

tion of the objective mini lens and the insufficient coherence of the electron sources, the lateral resolution of electron holography for magnetic imaging is limited to about 4 nm, which is far from the atomic scale. The resolution improvement can be achieved by a new design of a high-resolution objective mini lens or using an electrostatic lens. New electron sources with higher degree of spatial coherence such as single-atom emitters are also necessary.

2. Imaging 3D distribution of electric and magnetic field

The recorded electron phase shift in a conventional electron hologram is actually an integration along the electron path. Thus, in most of the electron holography applications, an assumption of homogeneous electric and magnetic field distribution along the electron path is involved. However, this is not always true. An imaging of the real 3D distribution of both electric and magnetic field in the sample is necessary. This can be done by a combination of the electron tomography techniques and electron holography. Such 3D distributions of electric and magnetic field can provide additional field information of semiconductor, ferroelectric and magnetic materials.

3. Direct visualization of the electronic structure in real space

Benefiting from the recent development of electron optics such as the Cs corrector, the resolution of modern TEM is continuously improved. A point resolution below 0.5 Å has been reported. It can be expected that such progress will still move on. For a long time, the ultimate goal of TEM was to answer the question "which atoms are where", while it is not so difficult to find the atoms positions with the sub-Å resolution instrument. Then the next question is what will we see at higher resolution? Can we see the electronic structure particularly the valence-electron distributions in real space? If so, it can be expected that the phase images will provide more useful information about the valence-electron distributions than the STEM-HAADF images and the conventional TEM images. This is because in STEM-HAADF, the collected electrons are mostly scattered at the core part of the atoms. Additionally, electron scattering from the valence-electron

is always week. In comparison to conventional HRTEM images, the phase images will provide more useful information on the bonding.

4. New method for fast calculation of the mean inner potential

The mean inner potential (MIP) is defined as the average Coulomb potential of the crystal. As we have already seen, MIP is widely used in electron microscopy as well as in electron holography. So, it is necessary to set up an efficient method for the calculation of the MIP for any materials. MIP sensitively depends on the electron density distribution of the material. Therefore, density functional theory (DFT) is necessary for the determination of the MIP. However, as the zero-point of MIP is defined outside of the crystal in infinite distance most of the DFT calculations will not provide this absolute value directly. A conventional method consists of the calculation of the Coulomb potential of a supercell with a vacuum layer [86]. The potential in the vacuum will be regarded as zero point. In order to decrease the surface effect, a multiple number of unit cells should be included. Then, the calculation for this large supercell will be very complex. Here, we proposed a new and very fast method for the MIP calculation. Instead of using a large supercell at the beginning, the electron density of one unit cell under periodic boundary conditions (PBC) will be calculated. After this, the electron density of this small unit cell will be repeated many times to set up a supercell. A vacuum layer will be added at the top. The Poisson equation has to be solved only once to get the potential from the electron density. As most of the computation time is consumed for the electron density calculation by means of DFT, this new method will drastically shorten the computation time and can be widely used for different materials from alloy structures to amorphous materials.

5. The influence of chemical bonding on the formation of high resolution TEM images

During the last two decades, most simulations of HRTEM images are based on the isolated atom scattering model. However, in a real crystal, the electron

density of the atoms is different due to the chemical bonds between the atoms. In particular, this affects the low angle electron scattering. It is necessary to investigate the influence of the bonding effects to the formation of HRTEM images. For this planned work a study is proposed consisting of the following steps: First, the electron density of the crystal will be calculated by DFT calculation. Second, the structure factor of the unit cell will be calculated from the electron density by means of the Poisson equation. Third, the structure factor as a function of the scattering angle is used as input into the conventional HRTEM simulation packages. Finally, the simulated results will be compared with both HRTEM simulations for isolated atoms and experimental HRTEM images.

Bibliography

[1] D. Gabor. A new microscopic principle. *Nature*, 161(4098):777–778, 1948.

[2] M.E. Haine and T. Mulvey. The formation of the diffraction image with electrons in the Gabor diffraction microscope. *J. Opt. Soc. Am*, 42: 763–773, 1952.

[3] E.N. Leith and J. Upatnieks. Reconstructed wavefronts and communication theory. *J. Opt. Soc. Am*, 52(10):1123–1130, 1962.

[4] G. Möllenstedt and H. Dueker. Beobachtungen und Messungen an Biprisma-Interferenzen mit Elektronenwellen. *Zeitschrift fuer Physik A Hadrons and Nuclei*, 145(3):377–397, 1956.

[5] G. Möllenstedt and H. Wahl. Elektronenholographie und Rekonstruktion mit Laserlicht. *Die Naturwissenschaften*, 55(7):340–341, 1968.

[6] H. Lichte, M. Reibold, K. Brand, and M. Lehmann. Ferroelectric electron holography. *Ultramicroscopy*, 93(3-4):192–212, 2002.

[7] S. Frabboni, G. Matteucci, G. Pozzi, and M. Vanzi. Electron holographic observations of the electrostatic-field associated with thin reverse-biased p-n-junctions. *Phys. Rev. Lett.*, 55(20):2196–2199, 1985.

[8] W. D. Rau, P. Schwander, F. H. Baumann, W. Hoppner, and A. Ourmazd. Two-dimensional mapping of the electrostatic potential in transistors by electron holography. *Phys. Rev. Lett.*, 82(12):2614–2617, 1999.

[9] J. Li, M.R. McCartney, and D.J. Smith. Semiconductor dopant profiling by off-axis electron holography. *Ultramicroscopy*, 94(2):149–161, 2003.

[10] A. C. Twitchett-Harrison, T. J. V. Yates, S. B. Newcomb, R. E. Dunin-Borkowski, and P. A. Midgley. High-resolution three-dimensional mapping of semiconductor dopant potentials. *Nano Lett.*, 7(7):2020–2023, 2007.

[11] A. Tonomura, T. Matsuda, J. Endo, T. Arii, and k. Mihama. Direct observation of fine-structure of magnetic domain-walls by electron holography. *Phys. Rev. Lett.*, 44(21):1430–1433, 1980.

[12] R. E. Dunin-Borkowski, M. R. McCartney, R. B. Frankel, D. A. Bazylinski, M. Posfai, and P. R. Buseck. Magnetic microstructure of magnetotactic bacteria by electron holography. *Science*, 282(5395):1868–1870, 1998.

[13] L. Reimer. *Transmission Electron Microscopy: Physics of Image Formation and Microanalysis*. Springer-Verlag, second edition, 1989.

[14] A. Tonomura. *Electron Holography*. Springer, second, enlarged edition, 1999.

[15] E. Völkl and M. Lehmann. The reconstruction of off-axis electron holograms. In E. Völkl, L.F. Allard, and D.C. Joy, editors, *Introduction to Electron Holography*. Kluwer Academics/Plenum Publishers, 1999.

[16] L. Marton. Electron interferometer. *Phys. Rev.*, 85(6):1057–1058, Mar 1952.

[17] A. Tonomura. Applications of electron holography. *Rev. Mod. Phys.*, 59 (3):639–669, Jul 1987.

[18] H. Lichte. Parameters for high-resolution electron holography. *Ultramicroscopy*, 51(1-4):15–20, June 1993.

[19] Q. Ru, J. Endo, T. Tanji, and A. Tonomura. Phase-shifting electron holography by beam tilting. *Appl. Phys. Lett.*, 59(19):2372–2374, 1991.

[20] Q. Ru, G. Lai, K. Aoyama, J. Endo, and A. Tonomura. Principle and application of phase-shifting electron holography. *Ultramicroscopy*, 55 (2):209–220, 1994.

[21] M. Lehmann and H. Lichte. Tutorial on off-axis electron holography. *Microsc. Microanal.*, 8(6):447–466, 2002.

[22] J.C. Russ. *The Image Processing Handbook*. CRC Press, 2006.

[23] D.J. Smith, W.J. de Ruijter, J.K. Weiss, and M.R. McCartney. Quantitative electron holography. In E. Völkl, L.F. Allard, and D.C. Joy, editors, *Introduction to Electron Holography*. Kluwer Academics/Plenum Publishers, 1999.

[24] G.C. Capitani, P. Oleynikov, S. Hovmöller, and M. Mellini. A practical method to detect and correct for lens distortion in the TEM. *Ultramicroscopy*, 106(2):66–74, 2006.

[25] J. M. Zuo. Electron detection characteristics of a slow-scan CCD camera, imaging plates and film, and electron image restoration. *Microsc. Res. Tech.*, 49(3):245–268, May 2000.

[26] D.C. Ghiglia and M.D. Pritt. *Two-dimensional phase unwrapping: theory, algorithms, and software*. Wiley New York, 1998.

[27] V. V. Volkov and Y. M. Zhu. Deterministic phase unwrapping in the presence of noise. *Opt. Lett.*, 28(22):2156–2158, 2003.

[28] H. Lichte and M. Lehmann. Electron holography - basics and applications. *Rep. Prog. Phys.*, 71(1), 2008.

[29] H. Lichte. Performance limits of electron holography. *Ultramicroscopy*, 108(3):256–262, 2008.

[30] A. Harscher and H. Lichte. Experimental study of amplitude and phase detection limits in electron holography. *Ultramicroscopy*, 64(1-4):57–66, 1996.

[31] D. Shindo and T. Oikawa. *Analytical Electron Microscopy for Materials Science*. Springer-Verlag, 2002.

[32] A.T. Fromhold and E.L. Cook. Schottky emission as a rate-limiting factor in thermal oxidation of metals. *Phys. Rev. Lett.*, 17(24):1212–1216, 1966.

[33] M. Born and E. Wolf. *Principles of Optics: Electromagnetic Theory of Propagation, Interference and Diffraction of Light*. Cambridge University Press, 7th edition, 1999.

[34] C. C. Chang, H. S. Kuo, I. S. Hwang, and T. T. Tsong. A fully coherent electron beam from a noble-metal covered W(111) single-atom emitter. *Nanotechnology*, 20(11), 2009.

[35] M. Lehmann. Influence of the elliptical illumination on acquisition and correction of coherent aberrations in high-resolution electron holography. *Ultramicroscopy*, 100(1-2):9–23, 2004.

[36] W.S. Boyels and G.E. Smith. Charge-coupled semiconductor devices. *Bell systems Tech.*, 49:587–599, 1970.

[37] G.Y. Fan and M.H. Ellisman. Digital imaging in transmission electron microscopy. *J. Microsc*, 200(1):1–13, 2000.

[38] P. Roberts, J.N. Chapman, and A.M. MacLeod. A CCD-based image recording system for the CTEM. *Ultramicroscopy*, 8:385–396, 1982.

[39] J.C.H. Spence and J.M. Zuo. Large dynamic range, parallel detection system for electron diffraction and imaging. *Rev. Sci. Instrum.*, 59:2102, 1988.

[40] D. B. Williams and C. Barry Carter. *Transmission Electron Microscopy: A Textbook for Materials Science*. Plenum Press, Newyork, 1996.

[41] F. Krumeich, 2007. http://www.microscopy.ethz.ch/lens.htm.

[42] F. Fiorillo. *Measurement and Characterization of Magnetic Materials*. Elsevier Academic Press, 2004.

[43] J. Crangle. *Solid State Magnetism*. Edward Arnold London, 1991.

[44] M.E. McHenry, M.A. Willard, and D.E. Laughlin. Amorphous and nanocrystalline materials for applications as soft magnets. *Prog. Mater. Sci.*, 44(4):291–433, 1999.

[45] G. Herzer. Nanocrystalline soft magnetic alloys. In K.H.L. Buschow, editor, *Handbook of Magnetic Materials*, volume 10, pages 415–462. Elsevier, Amsterdam, 1997.

[46] A. Makino, A. Inoue, and T. Masumoto. Nanocrystalline soft-magnetic Fe-M-B (M=Zr, Hf, Nb) alloys produced by crystallization of amorphous phase (overview). *Mater. Trans.*, 36(7):924–938, 1995.

[47] R. M. Bozorth. Atomic moments of ferromagnetic alloys. *Phys. Rev.*, 79(5):887, Sep 1950.

[48] K.R. Podolak, 2006. http://www.personal.psu.edu/ krp150/.

[49] J. Long, D.E. Laughlin, and M.E. McHenry. Structural and soft magnetic properties of a new nanocrystalline Fe-based and B-free alloy. *J. Appl. Phys.*, 103:07E708, 2008.

[50] G. Bertotti. *Hysteresis in Magnetism*. Academic Press San Diego, 1998.

[51] R. Carey and E.D. Isaac. *Magnetic Domains and Techniques for Their Observation*. The English University Press Ltd, London, 1966.

[52] E.D. Dahlberg and J.G. Zhu. Micromagnetic microscopy and modeling. *Phys. Today*, 48(4):34–40, 1995.

[53] M. Peshkin and A. Tonomura. *The Aharonov-Bohm Effect*. Springer-Verlag, 1989.

[54] Y. Aharonov and D. Bohm. Significance of electromagnetic potentials in the quantum theory. *Phys. Rev.*, 115(3):485–491, 1959.

[55] A. Tonomura, T. Matsuda, J. Endo, T. Arii, and K. Mihama. Holographic interference electron-microscopy for determining specimen magnetic-structure and thickness distribution. *Phys. Rev. B*, 34(5): 3397–3402, 1986.

[56] R. E. Dunin-Borkowski, M. R. McCartney, D. J. Smith, and S. S. P. Parkin. Towards quantitative electron holography of magnetic thin films using in situ magnetization reversal. *Ultramicroscopy*, 74(1-2):61–73, 1998.

[57] M. Getzlaff. *Fundamentals of Magnetism*. Springer, 2007.

[58] A. Hubert and R. Schäfer. *Magnetic Domains: the Analysis of Magnetic Microstructures*. Springer, 1998.

[59] C. Kittel and P. McEuen. *Introduction to Solid State Physics*. Wiley New York, 1986.

[60] S. Middelhoek. Domain walls in thin Ni-Fe films. *J. Appl. Phys.*, 34: 1054, 1963.

[61] R.F. Egerton. *Electron Energy-Loss Spectroscopy in the Electron Microscope*. Plenum press, New York, second edition, 1996.

[62] T. Malis, S. C. Cheng, and R. F. Egerton. EELS log-ratio technique for specimen-thickness measurement in the TEM. *J. Electron Microsc. Tech.*, 8(2):193–200, February 1988.

[63] V. V. Volkov, D. C. Crew, Y. Zhu, and L. H. Lewis. Magnetic field calibration of a transmission electron microscope using a permanent magnet material. *Rev. Sci. Instrum.*, 73(6):2298–2304, June 2002.

[64] FE Luborsky. High coercive materials. *J. Appl. Phys*, 32:171S–183S, 1961.

[65] G. Herzer. Nanocrystalline soft-magnetic materials. *Phys. Scr.*, T49A: 307–314, 1993.

[66] H. Foll. Electronic materials, 2006. http://www.tf.uni-kiel.de/matwis/amat.

[67] V.R.V. Ramanan and G.E. Fish. Crystallization kinetics in Fe- B- Si metallic glasses. *J. Appl. Phys.*, 53:2273, 1982.

[68] J. Stangl, V. Holý, and G. Bauer. Structural properties of self-organized semiconductor nanostructures. *Rev. Mod. Phys.*, 76(3):725–783, Sep 2004. doi: 10.1103/RevModPhys.76.725.

[69] G Blaylock, 1999. http://www-unix.oit.umass.edu/ blaylock/p284/.

[70] P. Bhattacharya, S. Ghosh, and A. D. Stiff-Roberts. Quantum dot opto-electronic devices. *Annu. Rev. Mater. Res.*, 34:1–40, 2004.

[71] E. Kasper and K. Lyutovich. *Properties of Silicon, Germanium and SiGe: Carbon.* Iet, 2000.

[72] Y. Shiraki and A. Sakai. Fabrication technology of SiGe hetero-structures and their properties. *Surf. Sci. Rep.*, 59(7-8):153–207, November 2005.

[73] M. Schmidbauer, T. Wiebach, H. Raidt, M. Hanke, R. Kohler, and H. Wawra. Self-organized ordering of $Si_{1-x}Ge_x$ nanoscale islands studied by grazing incidence small-angle x-ray scattering. *J. Phys. D: Appl. Phys.*, 32(10A):A230–A233, 1999.

[74] T. Teubner, U. Jendritzki, K. Böttcher, G. Schadow, R. Heimburger, A.K. Gerlitzke, S. Deiter, C. Eisenschmidt, T. Boeck, R. Fornari, et al. Liquid phase epitaxy set-up designed for in situ X-ray study of SiGe island growth on (001) Si substrates. *Cryst. Res. Technol.*, 43(12):1278–1285, 2008.

[75] J.C.H. Spence and J.M. Zuo. *Electron Microdiffraction.* Plenum Press, 1992.

[76] P. Rez. Virtual inelastic-scattering in high-energy electron-diffraction. *Acta. Crystallogra. A*, 34(JAN):48–51, 1978.

[77] E.J. Kirkland. *Advanced Computing in Electron Microscopy.* Plenum Pub Corp, 1998.

[78] W. Dorsch, M. Albrecht, H.P. Strunk, B. Steiner, H. Wawra, and G. Wagner. The transition from ripples to islands in strained heteroepitaxial growth under low driving forces. *J. Cryst. Growth*, 183(3):305–310, 1998.

[79] W. Dorsch, H.P. Strunk, H. Wawra, G. Wagner, J. Groenen, and R. Carles. Strain-induced island scaling during SiGe heteroepitaxy. *Appl. Phys. Lett.*, 72:179, 1998.

[80] P. Klapetek, D. Necas, and C. Anderson. Gwyddion, 2009. http://gwyddion.net.

[81] B. Fultz and J.M. Howe. *Transmission Electron Microscopy and Diffractometry of Materials*. Springer Verlag, 2001.

[82] S. Sque. Structure of diamond, 2006. http://newton.ex.ac.uk/.

[83] P.A. Doyle and P.S. Turner. Relativistic Hartree-Fock X-ray and electron scattering factors. *Acta Cryst.*, A24(3):390–397, 1968.

[84] J. P. Dismukes, E. Ekstrom, D. S. Beers, E. F. Steigmeier, and I. Kudman. Thermal + Electrical Properties Of Heavily Doped Ge-Si Alloys Up To 1300 Degrees K. *J. Appl. Phys.*, 35(10):2899–&, 1964.

[85] P. Kruse, M. Schowalter, D. Lamoen, A. Rosenauer, and D. Gerthsen. Determination of the mean inner potential in III-V semiconductors, Si and Ge by density functional theory and electron holography. *Ultramicroscopy*, 106(2):105–113, 2006.

[86] M. Y. Kim, J. M. Zuo, and J. C. H. Spence. Ab-initio LDA calculations of the mean Coulomb potential V-0 in slabs of crystalline Si, Ge and MgO. *Phys. Status Solidi A*, 166(1):445–451, 1998.

Acknowledgement

First of all, I would like to express my deepest gratitude to my supervisor, Professor Wolfgang Neumann for providing me constant support and inspiring guidance during my Ph.D studying. His immense knowledge, advice and encouragement are of great value for me. I would also like to thank him for his detailed and constructive comments to my work and the thesis.

I am very grateful to Dr. H. Kirmse for his valuable advice and friendly help, including experimental instructions and fruitful discussions of my work. Also many thanks for his careful reading of the manuscript.

I am grateful to our collaborators: Prof. David E. Laughlin, Prof. Michael E. McHenry and Dr. Jianguo Long (Carnegie Mellon University, USA) for providing us the magnetic samples. Particularly Dr. Jianguo Long gave us crucial help in magnetic domain structure analysis.

This thesis would not have been possible without the expert guidance. I am sincere gratitude to Dr. Kurt Scheerschmidt (Max Planck Institute of Microstructure Physics, Halle) and Prof. Michael Lehmann (Technical University of Berlin) for their kind help in theoretical and experimental methods.

I also would like to thank the colleagues in our group Dr. Ines Häusler, Dr. Anna Mogilatenko, Mr. Reinhard Otto and Ms. Panagoula Manolaki for their kind help. Many thanks for Mr. Stephan Wicke and Mrs Eva Oehlschlegel for technical support and Mrs. Silke Putzke for prompt settlement of administrative problem.

Finally I would like to thank my parents and my wife for their continuous support and encouragement over the years.

This work was supported by the German Research Society (DFG) with the GRK-1025 funds.